UiT
THE ARCTIC UNIVERSITY OF NORWAY

Faculty of Science and Technology
Department of Geosciences

Metamorphic evolution of the Passo Feio Complex (central part of the Dom Feliciano Belt, southern Brazil)

Tonje Tennholm

Master's thesis in Geology, GEO-3900
May 2019

Abstract

The Passo Feio Complex is considered as a part of the São Gabriel Terrane, located to the west of the Dom Feliciano Belt in the state of Rio Grande do Sul (Brazil), but shows numerous similarities with the easterly exposed Porongos Metamorphic Complex which is a part of the Schist Belt in that area.

P-T phase equilibrium modelling of metamorphosed sedimentary rocks from the Passo Feio Complex was performed with an aim to compare thermal conditions during their metamorphic evolution with those of the Porongos Metamorphic Complex and other related parts of the Dom Feliciano Belt foreland during orogenesis.

Petrographic and field observations of metapelitic samples suggest that the southern part of the complex can be subdivided into three metamorphic zones: one zone corresponding to greenschist facies conditions and two zones corresponding to lower and middle amphibolite facies conditions, respectively. Phase equilibrium modelling of samples from the southeastern (staurolite- and garnet-bearing) zone suggests that garnet started to crystallize at ca. 515-555°C and 2.7-4.8 kbar. Estimated peak metamorphic conditions suggest temperatures of ca. 535-590°C and pressures of ca. 4.7-7.6 kbar. Assuming an average crust density of 2.8 g/ cm^3, these conditions suggest an apparent thermal gradient of ca. 35-55°C/km during the onset of garnet growth, and 19-35°C/km for the equilibration of garnet rims and the matrix mineral assemblage. Phase equilibrium modelling of one sample from the southern zone (garnet-bearing) zone suggests that garnet started to crystallize at ca. 485°C and 2.6 kbar, and that peak metamorphic conditions were reached at temperatures of ca. 500-550°C and pressures of ca. 5.3-7.0 kbar. These conditions suggest an apparent thermal gradient of ca. 50°C/km for the onset of garnet growth and a decrease to ca. 20-29°C/km during peak metamorphic conditions. The rocks were thrust down to depths of ca. 17-28 km with a decrease in the apparent thermal gradient towards the equilibration of the matrix mineral assemblage. Contact metamorphism is evident close to the ca. 560 Ma Caçapava Granite, indicating that a local thermal event (M_2) occurred after the complex reached its peak metamorphic conditions.

The modelling results are similar to those from the easterly exposed Porongos Metamorphic Complex, suggesting that the protolith rocks of the Passo Feio Complex could have originally represented the same rift basin that was inverted during the formation of the Dom Feliciano Belt in the state of Rio Grande do Sul in the time interval between ca. 650 and 560 Ma.

"Rocks and minerals: the oldest storytellers."

- A.D Posey

Acknowledgements

This work was supported by the Norwegian Centre for International Cooperation in Education (SIU) and the Coordenação de Aperfeicoamento de Pessoal de Nível Superior (CAPES) in Brazil through the grant project no. UTF-2016-CAPES-SIU10024.

First of all, I would like to thank my supervisor Jiří Konopásek for giving me this opportunity. Thank you for excellent guidance, feedback and geological expertise. Your enthusiasm and outstanding dissemination inspired me to learn more about petrology in the first place.

Secondly, a huge thanks to Fátima Bitencourt and the geology crew at UFRGS for a warm welcome and a great adventure during fieldwork. Guiseppe Betino De Toni, Matheus Ariel Battisti and Stephanie Carvalho da Silva, thank you for the fantastic company. A special thanks to Jack James Percival and Matheus Ariel Battisti for all the help throughout the year, I wish you both the very best of luck in the future.

This would not have been possible without all the help that I have received with laboratory work. To the laboratory staff at the University of Tromsø, thank you for both introducing me to the laboratory work as well as producing the thin sections for me. Especially Karina Monsen, you are great! Also, a special thanks to Muriel Erambert for the microprobe session at the University of Oslo, it was a pleasure to learn from your expertise.

To my family and friends, thank you for all the support and for believing in me and believing in my choices. Finally, to all the wonderful geology students that I have been lucky enough to get to know through these years, I am thankful for the great social environment we have been a part of during this journey. I will certainly miss the super diamond squad, we had a blast!

Tonje Tennholm

Tromsø, May 2019

Abbreviations

Minerals

Ab	Albite
Act	Actinolite
Afs	Alkalifeldspar
Alm	Almandine
And	Andalusite
An	Anorthite
Ap	Apatite
Bt	Biotite
Chl	Chlorite
Fsp	Feldspar
Grt	Garnet
Grs	Grossular
Hbl	Hornblende
Hcrd	Hydrouscordierite
Hem	Hematite
Ilm	Ilmenite
Kfs	K-feldspar
Ky	Kyanite
Ms	Muscovite
Op	Opaque mineral
Pg	Paragonite
Pl	Plagioclase
Po	Pyrrhotite
Prp	Pyrope
Qtz	Quartz
Rt	Rutile
Sil	Sillimanite
Sph	Sphene
Sps	Spessartine
St	Staurolite
Stp	Stilpnomelane
Tur	Tourmaline
Zo	Zoisite
Zrn	Zircon

Other

a.p.f.u	Atoms per formula unit
X_{Mg}	$Mg^{2+} / (Mg^{2+} + Fe^{2+})$
X_{Alm}	$Fe^{2+} / (Fe^{2+} + Mg^{2+} + Mn^{2+} + Ca^{2+})$
X_{Prp}	$Mg^{2+} / (Fe^{2+} + Mg^{2+} + Mn^{2+} + Ca^{2+})$
X_{Grs}	$Ca^{2+} / (Fe^{2+} + Mg^{2+} + Mn^{2+} + Ca^{2+})$
X_{Sps}	$Mn^{2+} / (Fe^{2+} + Mg^{2+} + Mn^{2+} + Ca^{2+})$
X_{An}	$Ca^{2+} / (Ca^{2+} + Na^{+} + K^{+})$
PPL	Plane polarized light
XPL	Crossed polarized light

Table of Contents

1 Introduction 1
1.1 Geological setting 2
1.2 The Dom Feliciano Belt 5
1.2.1 Granite Belt 6
1.2.2 Schist Belt 7
1.2.3 Foreland Basins 7
1.3 Rio Grande do Sul Sector 8
1.3.1 Tectonic evolution of southern Brazil 9
1.4 Study area and previous research 10
1.4.1 São Gabriel Terrane 10
1.3.2 The Passo Feio Complex 11
2 Methods 15
2.1 Fieldwork 15
2.2 Laboratory work 15
2.2.1 Thin section preparation 15
2.2.2 Optical microscopy 15
2.2.3 Bulk chemical analysis 16
2.2.4 Mineral separation 16
2.2.5 Electron microprobe analysis and scanning electron microprobe (SEM) imaging 18
2.3 Phase equilibrium modelling 18
3 Results 21
3.1 Structural data 21
3.2 Sample introduction 24
3.3 Whole rock chemistry 27
3.4 Optical petrography and mineral chemistry 29
3.4.1 Sample BD03 29
3.4.2 Sample BD09b 31
3.4.3 Sample BD14 33
3.4.4 Sample BD15 36
3.4.5 Sample BD16c 38
3.4.6 Sample BD21 39

3.4.7 Additional samples 41
3.5 Phase equilibrium modelling 42
3.5.1 BD03 42
3.5.2 BD09b 47
3.5.3 BD14 50
3.5.4 BD15 53
3.5.5 BD16c 56
3.5.6 BD21 59
3.6 Chlorite geothermometry 60
3.6.1 Results of chlorite geothermometry 60
4 Discussion 63
4.1 Metamorphism related to deformational events 63
4.2 Metamorphic zones in the Passo Feio Complex 65
4.3 Age of metamorphism 67
4.4 P-T estimates and geothermal gradient 68
4.4.1 Comparison with other metasedimentary complexes of the Dom Feliciano Belt 70
4.5 Tectonic evolution of the Dom Feliciano Belt in the state of Rio Grande do Sul 74
5 Conclusions 79
Work cited 80
Appendix A 83

1 Introduction

The margins of South America and Africa were first recognized to match together as two pieces of a puzzle by the geographer Abraham Ortelius in 1596, and the Austrian geologist Eduard Suess indicated the existence of a 'larger continent' (Suess, 1885) before opening of the Atlantic Ocean by the end of the nineteenth century. This large continent has been given the name "Gondwana" after the shared flora, and since then it has been a subject of research (Siegesmund et al., 2018).

A large part of geological research related to the formation of Southwest Gondwana, especially in southern Brazil and western Africa, is conducted in orogens on both margins of the present South Atlantic Ocean. Remnants of the southwestern Gondwana are well represented by Neoproterozoic NE-SW trending fold belts along the South Atlantic margin together with old cratons towards the interiors of the African and South American continents (Basei et al., 2018; Philipp et al., 2018). One of these fold belts is the Dom Feliciano Belt, which will be discussed more in detail in this chapter.

This thesis represents a metamorphic study of samples of metasedimentary rocks from the Passo Feio Complex at the eastern edge of the São Gabriel Terrane, which represents the westernmost geological unit of the central Dom Feliciano Belt. The aim of the thesis is to provide information about the P-T conditions during thrusting of the São Gabriel Terrane under the overlying Porongos Complex in the central part of the Dom Feliciano Belt.

The study is based on field and laboratory work, petrographic studies, analyses of mineral compositions and equilibrium modelling of observed mineral assemblages. Whole rock chemistry of individual samples were used for the construction of P-T pseudosections using the Perple_X software by Connolly (2005).

1.1 Geological setting

The South American continent can be divided into two large geological domains, which are the Amazonas or pre-Brasiliano domain in the northwest and the Brasiliano domain occurring mainly in its central-eastern part. The Amazonas domain is of Laurentian affinity, while the Brasiliano domain is of Gondwana affinity and originated during the Brasiliano-Pan African Orogeny, also referred to as the Brasiliano Cycle in South America. This cycle involved the break-up of a former supercontinent called Rodinia and subsequent amalgamation of West Gondwana approximately between ca. 900 Ma and 500 Ma (Chemale et al., 1995; Basei et al., 2018).

The supercontinent Rodinia is referred to as the starting point for the Neoproterozoic tectonic history of West Gondwana, as most cratonic blocks were at that time amalgamated into the supercontinent by the end of the Mesoproterozoic (1.0-0.9 Ga). Subduction/accretion activity began along the continental margins of Rodinia, where crustal stretching led to the formation of rift basins in a continental back-arc region during early Neoproterozoic. These rift basins were continuously filled with products of syn-rift volcanism and detrital material formed by erosion of the surrounding Archean and Paleoproterozic cratons (Konopásek et al., 2018).

The rift phase lasted from around 850 Ma to ca. 680-660 Ma, with different stages of crustal thinning occurring simultaneously at different places along the continental margins. Subduction and magmatic arc formation marked a change of tectonic forces from extensional to compressional during the Late Neoproterozoic, leading to continental collision in the Middle Ediacaran and marking the beginning of the assembly of Gondwana (Basei et al., 2018; Konopásek et al., 2018). This continental collision is described by Rapalini (2018) as a protracted process of collision of several independent crustal blocks.

The Western Gondwana (Fig. 1.1) in Ediacaran-Cambrian times consisted of several cratons called Amazonia, West Africa, Congo-São Francisco, Kalahari and Río de la Plata (all of Archean to Paleoproterozoic age) together with some smaller crustal blocks (Konopásek et al., 2018; Rapalini, 2018). The East Gondwana blocks will not be discussed here.

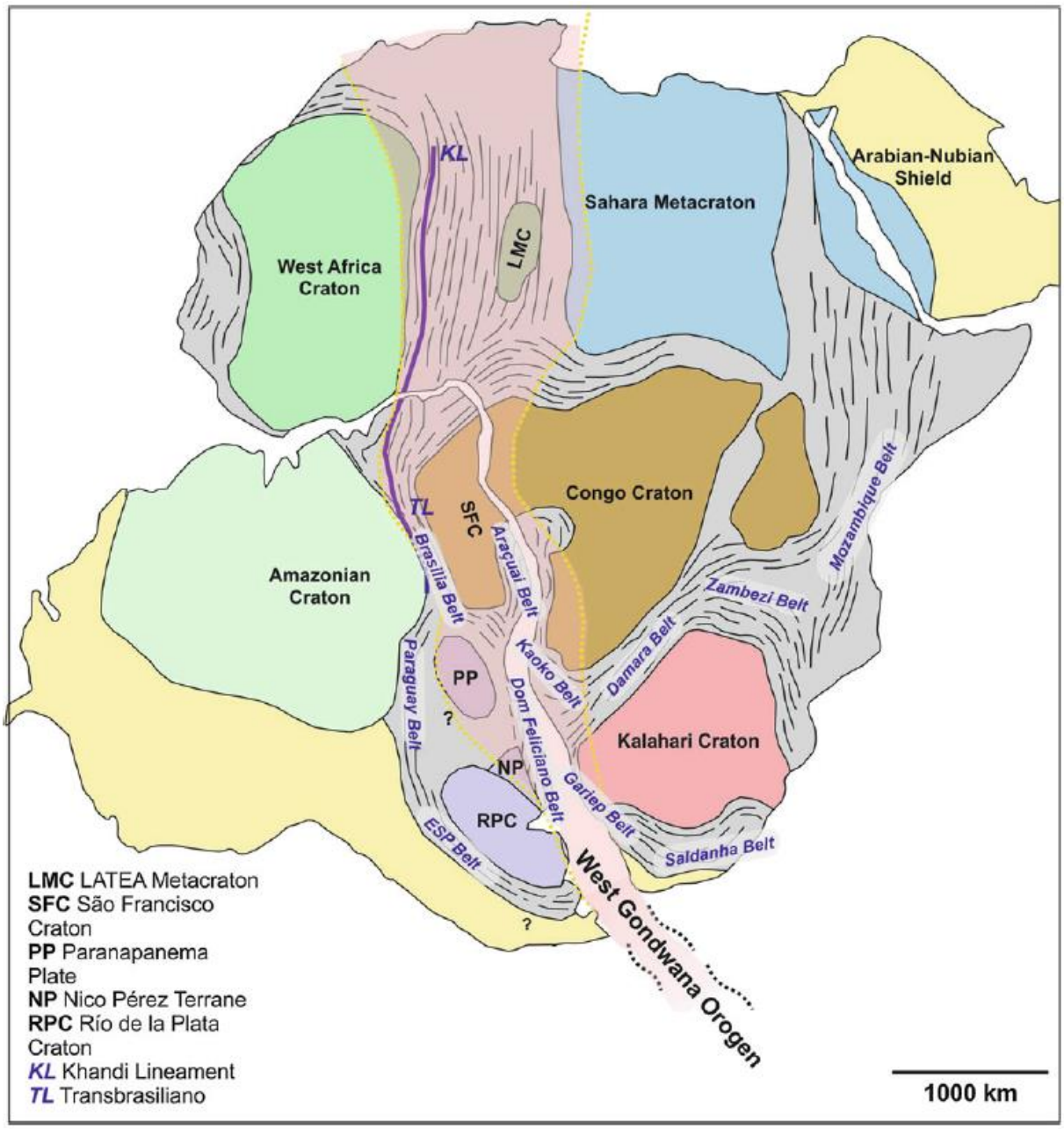

Fig. 1.1 *Illustration of the main crustal blocks of Western Gondwana and the position of orogenic belts (from Hueck et al., 2018). ESP Belt – Eastern Sierras Pampeanas Belt.*

The Nico Pérez Terrane was supposedly accreted to the Río de la Plata Craton around 630-625 Ma, where the latter represents an assortment of predominant Paleoproterozoic units (2.26-2.05 Ga) and does not show any significant Neoproterozoic reworking. The Nico Pérez Terrane, on the other hand, records Archean, Paleo- and Mesoproterozoic ages (Höfig et al., 2018).

Paleomagnetic data have indicated that the Amazonia and West Africa were probably still a part of Rodinia at its final break-up by the Early Ediacaran (ca. 615 Ma), and the Río de la Plata and Congo-São Francisco cratons were already attached and not a part of Rodinia by Mid-Ediacaran times (ca. 575 Ma). Rapalini (2018) has proposed a late accretion of the Kalahari Craton to the already assembled Río de la Plata-Congo-São Francisco blocks. The same author also proposed that the accretion of Eastern Gondwana blocks probably occurred in the latest Ediacaran-Cambrian times, as the Arabian-Nubian Shield was a part of proto-Gondwana by 550 Ma. Available paleomagnetic data suggests that Amazonia-West Africa was a part of Gondwana by ca. 525 Ma, but this is poorly constrained (Rapalini, 2018).

Neoproterozoic fold and thrust belts developed along the margins of some of these crustal blocks, as illustrates the Fig. 1.1. Among these are the Brasilia, Ribeira, Araçuai, Dom Feliciano, Kaoko, Damara and Gariep belts (Hueck et al., 2018). The Kaoko-Dom-Feliciano-Gariep orogenic system (Porada, 1989), with metaigneous rocks of Early Neoproterozoic age, is interpreted as a result of an interaction between the Río de la Plata, Congo and Kalahari cratons juxtaposed along major shear zones together with several microplates (Konopásek et al., 2018; Hueck et al., 2018).

In the next sections, the regional geology of the Dom Feliciano Belt (Fig. 1.1) will be presented with focus on the study area; the Passo Feio Complex within the São Gabriel Terrane located in the southernmost Brazil.

1.2 The Dom Feliciano Belt

The Neoproterozoic Dom Feliciano Belt (DFB) evolved from rifting, drifting and amalgamation between ca. 900 and 500 Ma, as a result of the collision between the Congo, Kalahari and Río de la Plata cratons (Fig. 1.1; de Oliveira et al., 2014). The basement of the DFB is represented by the Archaean to Paleoproterozoic Luís Alves and Nico Pérez terranes, which acted as a foreland to the belt in South America (Hartmann et al., 2000; Hueck et al., 2018).

The Dom Feliciano Belt (Fig. 1.2) is the southernmost portion of the so-called Mantiqueira Province, which is a collective term used in Brazil for the main Neoproterozoic orogenic domains along the Atlantic coast, and formed during the assembly of West Gondwana. Apart from the DFB, it also comprises the Ribeira (Paraná, Sáo Paulo, Minas Gerais and Rio de Janeiro states) and Araçuaí (Espírito Santo, eastern Minas Gerais and southern Bahia states) belts in its northern part. The African counterparts are the Saldania-Gariep, Damara, Kaoko and West Congo belts (Basei et al., 2018; Hueck et al., 2018; Philipp et al., 2016; Philipp et al., 2018).

The Dom Feliciano Belt is the geotectonic unit of greatest continuity in the Mantiqueira Province, with its approximate length of 1200 kilometers and maximum width of 200 kilometers. This NE-SW trending belt extends along the Atlantic coast through the southeastern part of Brazil and Uruguay, with a northern limit in the state of Santa Catarina and southern termination in Uruguay (Fig. 1.2). The DFB can be divided into three main lithotectonic domains: granitic batholiths, metasedimentary sequences and associations of foreland basins, also known as the Granite Belt, the Schist Belt and the Foreland Basins, respectively. These three domains are all exposed in different structural windows of the belt, in the state of Santa Catarina, Rio Grande do Sul and in Uruguay (Basei et al., 2000; Basei et al., 2018; Hueck et al., 2018).

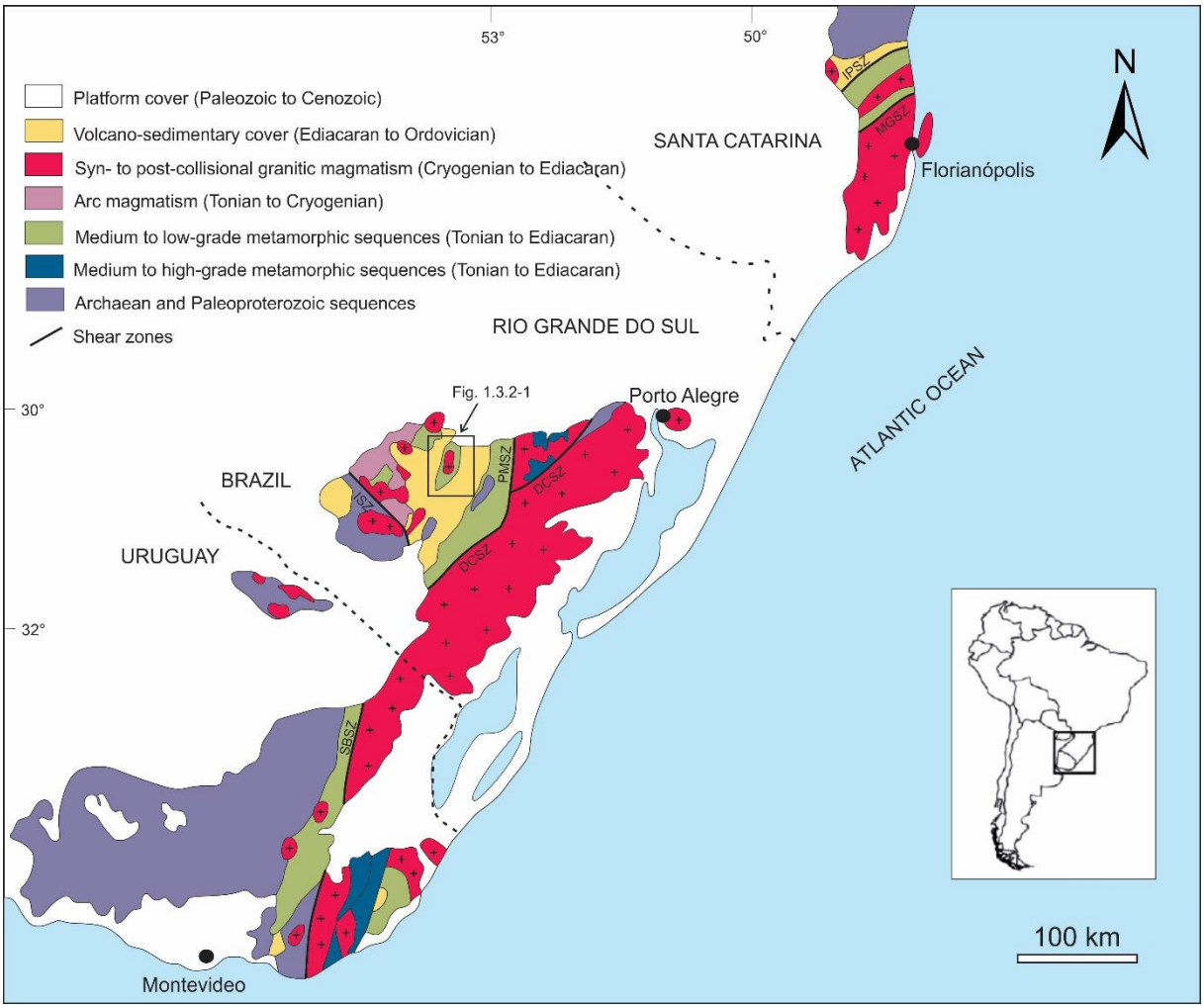

Fig. 1.2 *Tectonic map of the Dom Feliciano Belt (modified after Battisti et al. 2018). IPSZ – Itajaí-Perimbó Shear Zone; MGSZ – Major Gercino Shear Zone; DCSZ – Dorsal do Canguçu Shear Zone; PMSZ – Passo do Marinheiro Shear Zone; ISZ – Ibaré Shear Zone; SBSZ – Sierra Ballena Shear Zone.*

1.2.1 Granite Belt

The Granite Belt is the easternmost domain of the DFB, a part of the syn- to post-collisional granitic magmatism with Cryogenian to Ediacaran age (Fig. 1.2). The belt consists of deformed calc-alkaline to alkaline granitoid rocks and comprises three segments of batholiths separated from each other by the Paraná Basin sediments. These are the Florianópolis Batholith in the state of Santa Catarina (SC), the Pelotas Batholith in the state of Rio Grande do Sul (RS) and the Aiguá batholith in Uruguay (UY), with more or less continuous magmatic activity between ca. 650 Ma and 550 Ma, as determined by dating of various intrusions (Basei et al., 2000; Basei et al., 2018; Hueck et al., 2018).

1.2.2 Schist Belt

The NE-SW trending Schist Belt consists of medium- to low-grade metamorphic sequences of Tonian to Ediacaran age (Fig. 1.2). It represents supracrustal rocks situated between the Foreland Basins and the Granite Belt, and can be separated into three metamorphic complexes named Brusque (SC), Porongos (RS) and Lavelleja (UY). These metasedimentary and metavolcano-sedimentary sequences have been metamorphosed at greenschist facies and locally at lower amphibolite facies, and folded by several deformational phases (Basei et al., 2000; Basei et al., 2008).

1.2.3 Foreland Basins

The Foreland Basins are located along the western side of the Schist Belt, as a volcano-sedimentary cover of Ediacaran to Ordovician age (Fig. 1.2), and they are grouped into three main basins named Itajaí (SC), Camaquã (RS) and El Soldado-Piriánopolis (UY). These basins were formed in the late stages of the Brasiliano Cycle, when lateral escape tectonic events with extensional components generated space for basin development and sediment accumulation (Basei et al., 2000; de Oliveira et al., 2014).

The Camaquã Basin in Rio Grande do Sul is the largest and most complete foreland basin in the Dom Feliciano Belt. It was filled by sedimentary and volcano-sedimentary deposits and deformed between ca. 620 Ma and 540 Ma (Basei et al., 2000; de Oliveira et al., 2014; Hueck et al., 2018). The basin sediments are stratigraphically divided into different sediment groups, each with distinct structural and lithological characteristics (de Oliveira et al., 2014).

1.3 Rio Grande do Sul Sector

The central domain of the DFB in Rio Grande do Sul (Fig. 1.2) is a part of the Sul-Riograndense Shield, which is an association of Precambrian terranes composed of various geotectonic units with distinct characteristics, all juxtaposed during the Brasiliano Cycle. The Sul-Riograndense Shield can be divided into four different geotectonic units (Fig. 1.3) known as the Taquarembó Terrane, the São Gabriel Terrane, the Porongos Belt (also referred to as the Tijucas Terrane) and the Pelotas Batholith. Shear zones are separating these units and they are further overlain by the Camaquã Basin (Pertille et al., 2017; Hueck et al., 2018).

The Taquarembo Terrane is assumed to consist of exposures of the Río de la Plata Craton (Saalmann et al., 2011), while the Pelotas Batholith, Porongos Belt and the Camaquã Basin represent tectonic units of the DFB formed or reworked during the Neoproterozoic. The Pelotas Batholith is part of the large granitic association, the Porongos Belt is composed of metavolcano-sedimentary rocks and basement inliers and constitutes the central domain of the schist belt, and the Camaquã Basin is a foreland basin with a thick sedimentary package containing subordinate volcanic rocks predominantly deposited during the Ediacaran. The São Gabriel Terrane is a part of the western and oldest part of the Sul-Riograndense Shield (Hueck et al., 2018).

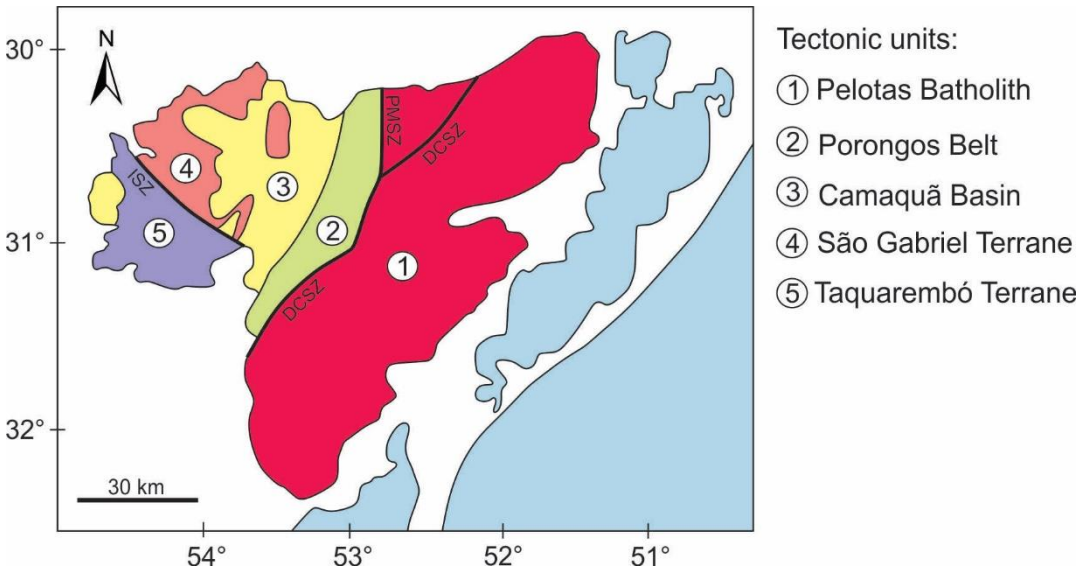

Fig. 1.3 *Simplified geological map of the Rio Grande do Sul sector of the Dom Feliciano Belt (modified after Hueck et al., 2018). ISZ – Ibaré Shear Zone; PMSZ – Passo do Marinheiro Shear Zone; DCSZ – Dorsal do Canguçu Shear Zone.*

1.3.1 Tectonic evolution of southern Brazil

There are three Brasiliano events that have been recognized in Rio Grande do Sul, and these are the Passinho event at ca. 0.9 Ga, the São Gabriel event at ca. 750-700 Ma and the Dom Feliciano event at ca. 620-600 Ma (Saalmann et al., 2011). Most of the geological units in the region were generated and/or intensely deformed during the Brasiliano Cycle, over a time period of more than 300 million years (Chemale Jr. et al., 1995; Saalmann et al., 2011).

Archaean and Paleoproterozoic (2.26-2.0 Ga) rocks are exposed in the Taquarembó Terrane in the western region of the Sul-Riograndense Shield. The NW-SE-trending Ibaré Shear Zone (ISZ) separates the Taquarembó Terrane from the São Gabriel Terrane, which is assumed to have been thrust onto the Río de la Plata Craton and consists of Neoproterozoic juvenile orthogneisses with ages between 880 and 700 Ma that have intruded into metavolcano-sedimentary rocks. The São Gabriel Terrane was later accreted to the Nico Pérez Terrane, the basement of the Porongos Belt. This belt consists of SW-NE-trending volcano-sedimentary schists with an approximate age of 790 Ma, formed in an intra-continental basin. The Dorsal de Canguçu Shear Zone (DCSZ) separates the Porongos Belt from the ca. 620-590 Ma Pelotas Batholith to the east. Late Neoproterozoic to Cambrian successions of the Camaquã foreland basin cover large areas of the Sul-Riograndense Shield, deposited during late-orogenic stages between ca. 630 and 580 Ma (Chemale Jr. et al., 1995; Saalmann et al., 2011).

The Passo Feio Complex, which is a target of this study, is considered as a part of the São Gabriel Terrane (SGT), which is located in the western part of the Sul-Riograndense Shield (Fig. 1.3). According to several researchers, the SGT represents one of the best exhibitions of the initial evolution period of the Brasiliano Cycle, as it contains all of the elements related to construction and closure of Neoproterozoic oceans (Philipp et al., 2018).

1.4 Study area and previous research

1.4.1 São Gabriel Terrane

The São Gabriel Terrane (SGT) consists of two Neoproterozoic juvenile arcs, respectively of Tonian and Cryogenian age, a late-collisional basin and remnants of ophiolithic complexes (Philipp et al., 2018). The juvenile signature of the Neoproterozoic metavolcano-sedimentary rocks and gneissic rocks within the SGT is a unique feature in contrast to most other Brasiliano belts that are characterized by remobilization of older continental crust (Babinski et al., 1996; Saalmann et al., 2011).

The São Gabriel Terrane (Fig. 1.3) has an elongated shape in the N20-30°E direction, and covers an area of approximately 110 x 60 km. Phanerozoic units of the Paraná Basin cover the SGT in the northern and western areas, while it is limited to the south by the Ibaré Shear Zone, and to the east by the Caçapava magnetic anomaly (Babinski et al., 1996; Saalmann et al., 2011; Philipp et al., 2018).

The tectonic evolution of the São Gabriel Terrane started with the opening of an oceanic domain between ca. 930 and 900 Ma. This ocean was located east of the Río de la Plata Craton (RPC) and west of the Nico Pérez Terrane (NPT). An intraoceanic island arc, the Passinho Arc, formed between ca. 890 and 860 Ma. The São Gabriel Arc formed between ca. 770 and 720 Ma, and it was subsequently accreted to the western margin of the Nico Pérez Terrane around 710-700 Ma. Emplacement of late orogenic granites at ca. 700-680 Ma marks the post-collisional stage (Philipp et al., 2018).

The tectonic evolution of the SGT has resulted in a geological unit consisting of intra-oceanic to magmatic arc rocks, ophiolites and post-tectonic granites. These rocks can be grouped into the Cambaí orthogneisses and the supracrustal sequences of the Passo Feio, Cambaizinho, Palma and Bossoroca complexes, as well as the Mantiqueiras sequence and Ibaré Complex that include ophiolites of Tonian age (Saalmann et al., 2011). Philipp et al. (2018) divided the SGT into four main associations, which are metasedimentary complexes, the Palma Accretionary Prism, arc-related rocks and volcano-sedimentary rocks of the Camaquã Basin and plutonic

rocks associated (Philipp et al., 2018). The association of different rock units within the SGT are named and categorized differently by various reasearchers.

Saalmann et al. (2011) described four main deformational phases that can be distinguished in the SGT, respectively known as D_1, D_2, D_3 and D_4. The first deformational event (D_1) included development of a first foliation parallel to the compositional layering associated with formation of quartz veins. These quartz veins have been subsequently deformed into tight to isoclinal folds (D_2) accompanied by amphibolite facies metamorphism. L_2 mineral and stretching lineation oriented parallel to F_2 fold axes are locally preserved in some places. D_1 and D_2 structures are overprinted by D_3 deformation, and their ages have been bracketed between the first signs of subduction activity in the area (ca. 880 Ma) and the beginning of the São Gabriel event and D_3 (ca. 750-730 Ma). Tight F_3 folds with subvertical to steeply NW-dipping fold axial planes refolded the isoclinal F_2 folds. The last deformational event (D_4) occurred during retrograde metamorphism and is characterized by semi-brittle to brittle SE-directed thrusting, which led to imbrication, kinking and thrust-related folding. This deformation either immediately followed the latest stages of D_3 or it may represent a later thrusting event. Intrusion of the Caçapava Granite thus sets a minimum age of 560 Ma for the last event (Saalmann et al., 2011).

1.3.2 The Passo Feio Complex

The Passo Feio Complex (PFC) is located in the Caçapava do Sul region (Fig. 1.4). In terms of geological position, it is exposed along the eastern edge of the São Gabriel Terrane, and consists of a Neoproterozoic supracrustal metavolcano-sedimentary sequence intruded by the Caçapava Granite at ca. 560 Ma (Remus et al., 2000). It is originally defined as a sequence of metapelite, marble, calc-silicate schist, quartzite, amphibolite, metavolcanic/metavolcano-clastic rocks and magnesium schist. The sequence has been considered as a part of a passive margin sequence, but the geotectonic significance regarding the original basin in relation to the tectonic evolution of the SGT is not well understood (Lopes et al., 2015; Philipp et al., 2018).

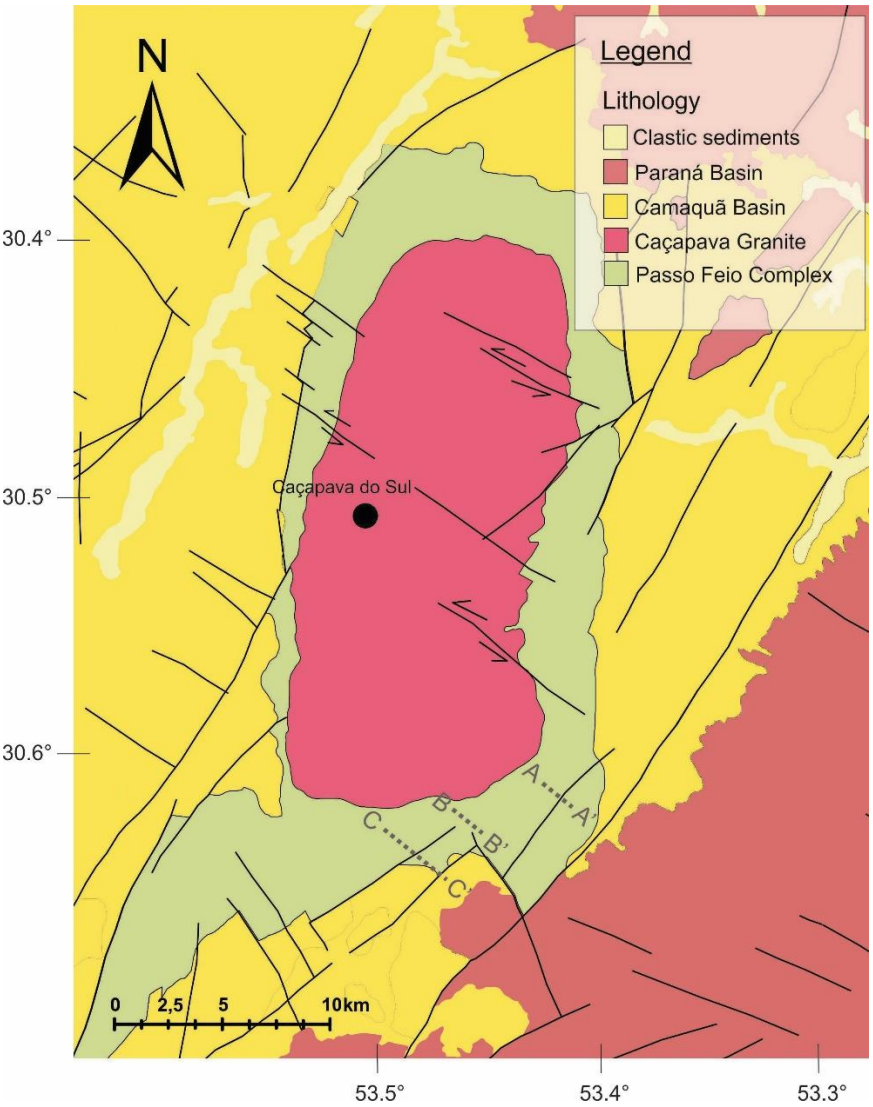

Fig. 1.4 *Illustrated map of the Passo Feio Complex. The city of Caçapava do Sul is indicated by a black circle. Profiles A-A', B-B', C-C' are shown in grey.*

Metasedimentary rocks in the PFC contain xenocryst zircons of Archaean, Paleoproterozoic and Neoproterozoic ages that were metamorphosed at ca. 700 Ma, according to Remus et al. (2000). Lopes et al. (2015) dated detrital zircons of metapelite samples both from the northern and southern part of the PFC showing an age range from 3637 to 803 Ma, which implies that sediments derived from several continental sources. The Archean to Paleoproterozoic age pattern implies that detrital material derived from adjacent cratons, as well as a contribution from younger Neoproterozoic sources not consistent with derivation solely from the craton (Lopes et al., 2015). The age of the metapelites in the PFC is poorly known, but Soliani (1986) obtained ages between 556-666 Ma from muscovites and microdiorites.

Bitencourt (1983) described two regional metamorphic events, M_1 and M_2, evident in the PFC. The first one (M_1) occurred around 700 Ma and the second one (M_2) at 562 ± 8 Ma, contemporaneous to the Caçapava Granite intrusion (Bitencourt, 1983; Remus et al., 2000). The grade of metamorphism varies from greenschist to amphibolite facies, as the metamorphic assemblages of the chlorite and staurolite zones are preserved, where M_1 reaches amphibolite facies as represented by the staurolite zone and M_2 is retrogressive, characterized by growth of chlorite and representing the greenschist facies (Bitencourt, 1983). At least two deformation events have been observed in the PFC, and these are synchronous with the metamorphic events M_1 and M_2 (Remus et al. 2000).

2 Methods

2.1 Fieldwork

Fieldwork was conducted in the state of Rio Grande do Sul in southern Brazil between the 16th and 26th of June 2018, in areas outside the city of Caçapava do Sul (Fig. 1.4). The main purpose of the fieldwork was to collect samples from the Passo Feio Complex for the estimation of metamorphic conditions. 24 samples in total were collected in the field and on each locality, the sampling was completed by macroscopic observations and structural measurements. Stereographic plots presented in chapter 3.1 were constructed with the Orient 3.8.0 software program.

2.2 Laboratory work

Laboratory work included thin section preparation, optical microscopy, bulk rock chemical analysis, mineral separation, electron microprobe analysis and scanning electron microscope (SEM) imaging.

2.2.1 Thin section preparation

Petrographic thin sections were made from all of the 24 samples. The samples were cut into two pieces with a diamond saw perpendicular to observed planar fabric and parallel with the lineation, if present. After drying, a selected area of each sample was cut into smaller blocks of approximately 1 cm x 2.2 cm x 3 cm when possible. Further preparation of the thin sections was completed by the laboratory staff at the Department of Geosciences at the University of Tromsø.

2.2.2 Optical microscopy

A Leitz Wetzlar polarization microscope was used for the petrographic study of mineral assemblages, mineral textures and crystallization relationships. Based on the stable mineral assemblages present in the thin sections and the degree of preservation, six of the 24 samples were selected for the estimation of metamorphic conditions. Photos of thin sections were taken using a Leica DFC450 camera.

2.2.3 Bulk chemical analysis

The six samples selected for determination of whole rock composition were cleaned and air-dried to avoid contamination, before crushing them into smaller pieces. Based on the sample sizes, some were crushed with a hammer, while others were crushed using a hammer mill. Further on, 50 ml of each of the crushed samples were milled using a planetary ball mill (Retsch PM 100), in an agate bowl with 15 agate balls to achieve the analytical grain size. Mill time of every sample varied between 4 minutes and 12 minutes, depending on their physical properties. All equipment was washed and blow-dried before the introduction of a new sample to avoid contamination.

Approximately 10 grams of each of the six samples were sent to the Bureau Veritas laboratories in Vancouver, Canada, for conduction of the bulk chemical analyses, and the same analyses were also conducted locally at the University of Tromsø. Before the actual analysis, the samples were ignited and then melted for the preparation of glass pellets. The ignition process involved igniting approximately two grams of each sample in a furnace at 1000°C ± 50°C for one hour, and then cooled in a desiccator for at least one hour. Ignition is done to determine the loss of ignition, which is used for correction of results of the analysis to represent the original (not ignited) material. Further on, 5.6000 ± 0.0001 grams of flux (LT66:LM34 with 66.0 % lithium tetraborate, 34.0 % lithium metaborate and 0.2 % lithium bromide) were measured up and filled in glass containers. 0.8000 ± 0.0001 grams of each sample were measured up and mixed in the glass containers together with the flux, which is used to give samples a similar matrix and to make the melting process easier. The samples were subsequently placed in a melting device for automated glass pellet production, before analysis of major elements with a Bruker S8 Tiger wavelength dispersive X-ray fluorescence spectrometer.

2.2.4 Mineral separation

Based on optical microscopy, two samples (BD03 and BD05) were selected as potentially suitable for dating of monazites. As one of them was needed for the whole rock analysis, 50 ml of the sample were kept separately, while the rest was run through the Wilfley shaking table to separate heavy, intermediate and light fractions. The other sample was chosen solely for dating of monazites, so the entire sample was separated into fractions through the shaking table. The

heavy fractions potentially containing monazite grains were saved for further mineral separation.

Gravity separation using a heavy liquid was conducted to further concentrate the heavy fractions required for analysis. This method is based on known variations in specific gravity among different minerals, where lithium heterotungstate (LST) liquid with a density of 2.86 g/cm^3 was used to separate minerals with lower densities, such as e.g. quartz and feldspars (depending on composition). The remaining concentrates were washed and air-dried over night.

For magnetic separation, magnets of iron and neodymium were used to remove strongly magnetic minerals from the samples. The remaining concentrates were run through a Frantz isodynamic magnetic separator (model L-1) with a tilt of 20° and a magnetic field of 0.5 mA. The magnetic separator split concentrates into magnetic and non-magnetic fractions, where the non-magnetic fractions were used for further work while the magnetic ones were kept separately.

For the mixture of minerals which are not easy to separate magnetically, it is possible to use a sieve. A sieve with holes of 100 μm was used during this work due to the small grain size of monazites expected in the sample. The coarse fraction was then stored, while the fine fraction in the bottom container was run through the magnetic separator with an aim to split monazite from other similar-sized minerals. The non-magnetic fraction could then be loaded in diiodomethane (DIM), which is another type of heavy liquid used to separate minerals according to their density. The difference between DIM and LST is that LST has a low viscosity and the density can be adjusted by adding or evaporating deionized water, while DIM has a higher density (3.32 g/cm^3) and can separate heavy minerals from the heavy fraction after the LST treatment.

2.2.5 Electron microprobe analysis and scanning electron microprobe (SEM) imaging

Quantitative measurements of mineral chemistry for minerals in the six selected samples were made by electron probe microanalysis at the University of Oslo, using a CAMECA SX100 electron microprobe with five spectrometers. An operating accelerating voltage of 15 kV and a beam current of 15 nA were used for point analysis for all mineral phases.

2.3 Phase equilibrium modelling

The Perple_X (version 6.8.5) software package (Connolly, 2005) was used to construct P-T pseudosections and compositional isopleths. P-T pseudosections are modelled equilibrium phase diagrams that show stable mineral phases when calculated with a specific bulk chemical composition and within chosen pressure and temperature intervals. Compositional isopleths are graphical contours that present how a composition of minerals evolve through the P-T space.

Perple_X is a software made for calculation and interpretation of a phase diagram section, and consists of the following steps; problem definition, phase diagram section computation and depiction, computational assessment, digital interpretation and graphical interpretation. Each of the steps involves different programs in which Fig. 2.1 illustrates. Calculation of pseudosections was conducted through the use of the following routines; BUILD (problem definition), VERTEX (calculation) and PSSECT (graphical representation). Compositional isopleths were calculated through WERAMI (digital interpretation) and PSTABLE (graphical representation) routines. Outputs from PSSECT and PSTABLE were redrawn in CorelDRAW for a better readability.

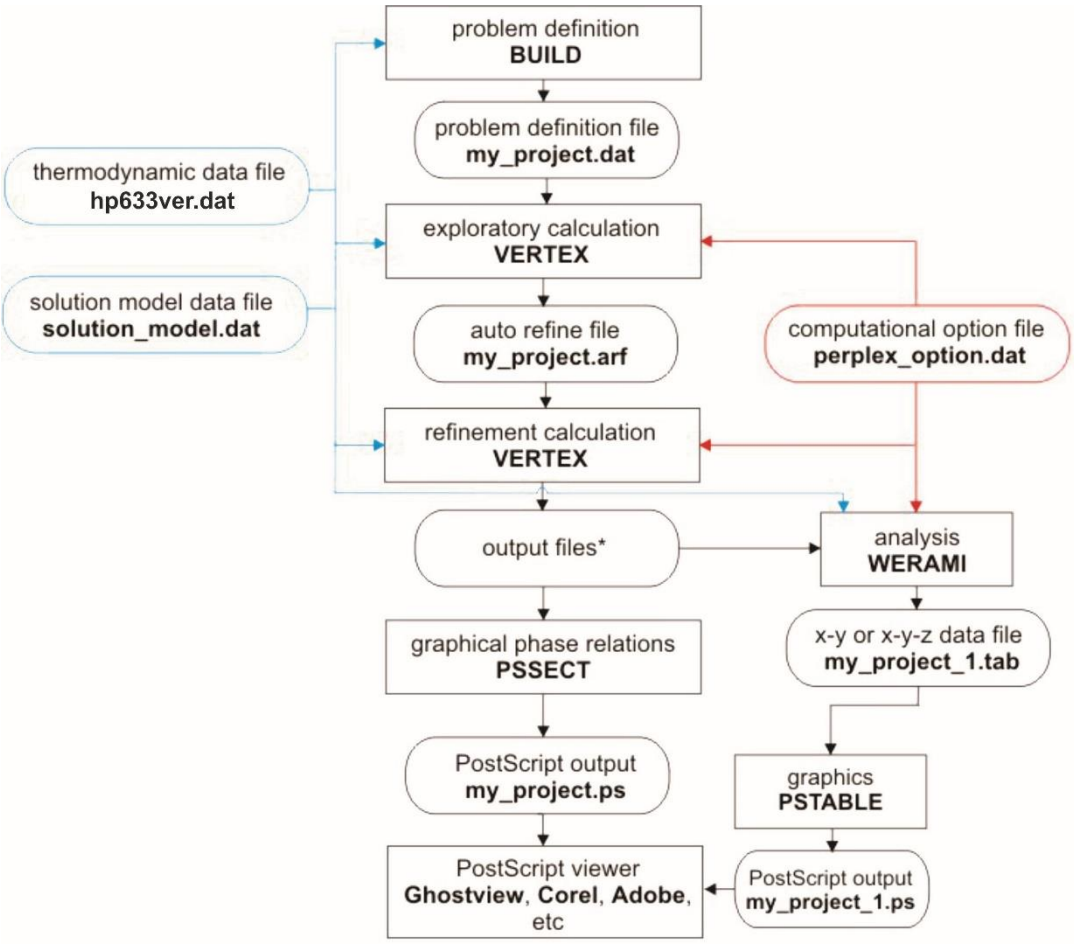

Fig. 2.1 *Schematic overview of the Perple_X program structure. Modified after Perple_X documentation; web-based tutorials (http://www.perplex.ethz.ch/perplex_66_seismic_velocity.html).*

3 Results

3.1 Structural data

This chapter presents a brief summary of structural observations and data collected during the fieldwork within the Passo Feio Complex. Structural relationships observed in the field are important to consider in order to relate observed metamorphic mineral assemblages to deformational events. Rare good outcrops due to dense vegetation and a high degree of weathering made the structural work rather challenging in some places.

At least two, but possibly three, deformational events were observed in the studied area. The deformational events are further referred to as D_1, D_2 and D_3, where the latter is a matter of interpretation and will be discussed in chapter 4.

The first deformational event (D_1) is here described as the event that started with reworking and metamorphism of the sedimentary layering (S_0), resulting in a foliation (S_1) usually represented by shape preferred orientation of micas or by compositional layerings. Furthermore, obligue to recumbent tight to isoclinal folds (F_1) were produced, as the S_1 fabric is observed to have been affected by a folding event. Fold axial planes are subparallel with the S_1 foliation in some outcrops, and more differentiated in others. Folded quartz veins are often present at various outcrops, and the S_1 foliation seems to be the dominant fabric in the Passo Feio Complex. Lineation (L_1) parallel with the fold axes were observed.

The second deformational event (D_2) can be described as a compressional event that led to folding (F_2) of the S_1 foliation by larger-scale open folds, as shown in Fig. 3.3. Measured fold axial planes in the respective areas are not parallel with the S_1 foliation, as the figure illustrates.

Measured orientations of fold axial planes and fold axes throughout the study area are presented in Fig. 3.1. The axial planes show a visible NE-SW-trend in dip direction, where the majority of the measured ones are dipping towards NW. The fold axes have a low to moderate plunge towards NE and SW.

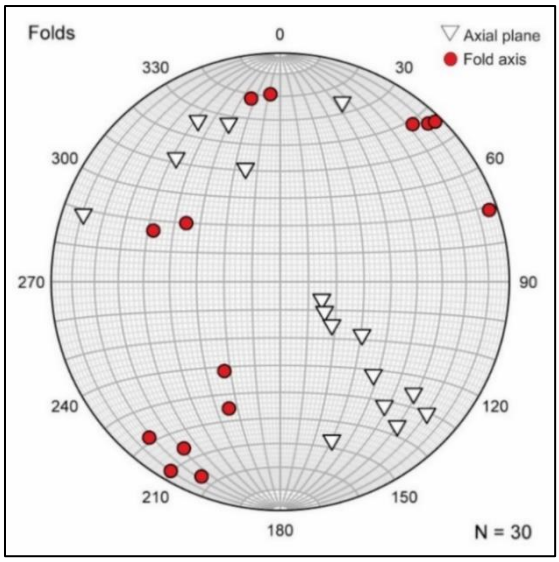

Fig. 3.1 *Stereographic projections of fold measurements. Fold axial planes and fold axes are plotted together as poles.*

All foliation measurements throughout the study area show a NE-SW-trend and are presented in a stereonet in Fig. 3.2a. The dip of the foliation varies from low- to high-angle due to folding and some competence differencies within the rocks, but the foliation still show the same overall pattern. The majority of foliation planes are dipping towards the SE, but some dip towards NW. Lineation observed in the field shows more or less the same trend as the foliation (Fig.3.2b). Stretching lineations and mineral lineations are included in the latter, and the overall orientation of all lineations is subparallel to the fold axes.

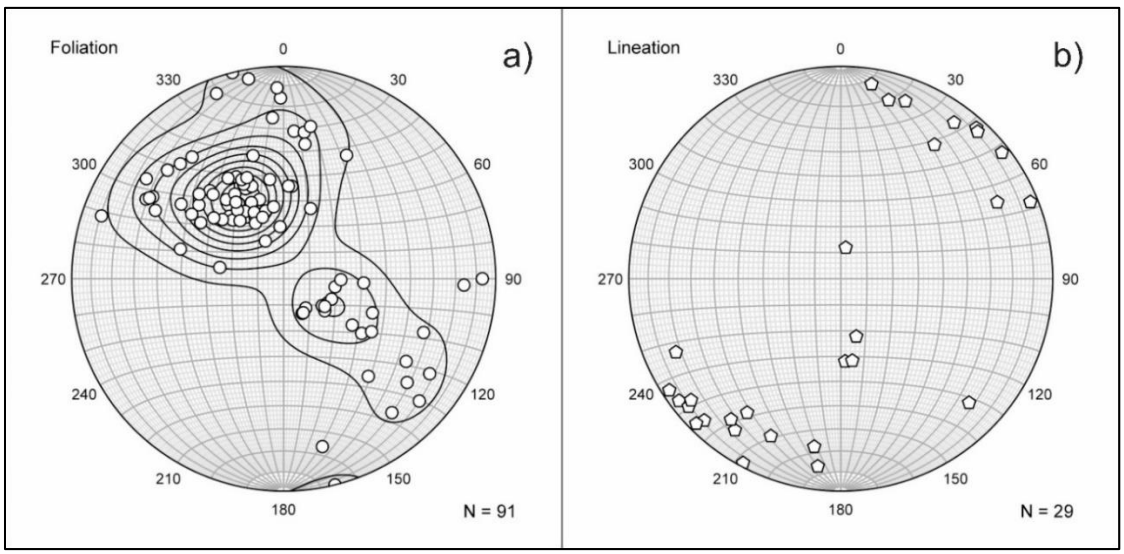

Fig. 3.2 *Stereographic porjections of* ***a)*** *foliation and* ***b)*** *lineation, plotted as poles.*

Foliation and fold axial planes from respective areas of the profile lines in Fig. 1.4 are presented below in Fig. 3.3. There is a visible trend regarding the fold axial planes and their orientation in these areas, together with the orientation of the foliation measured.

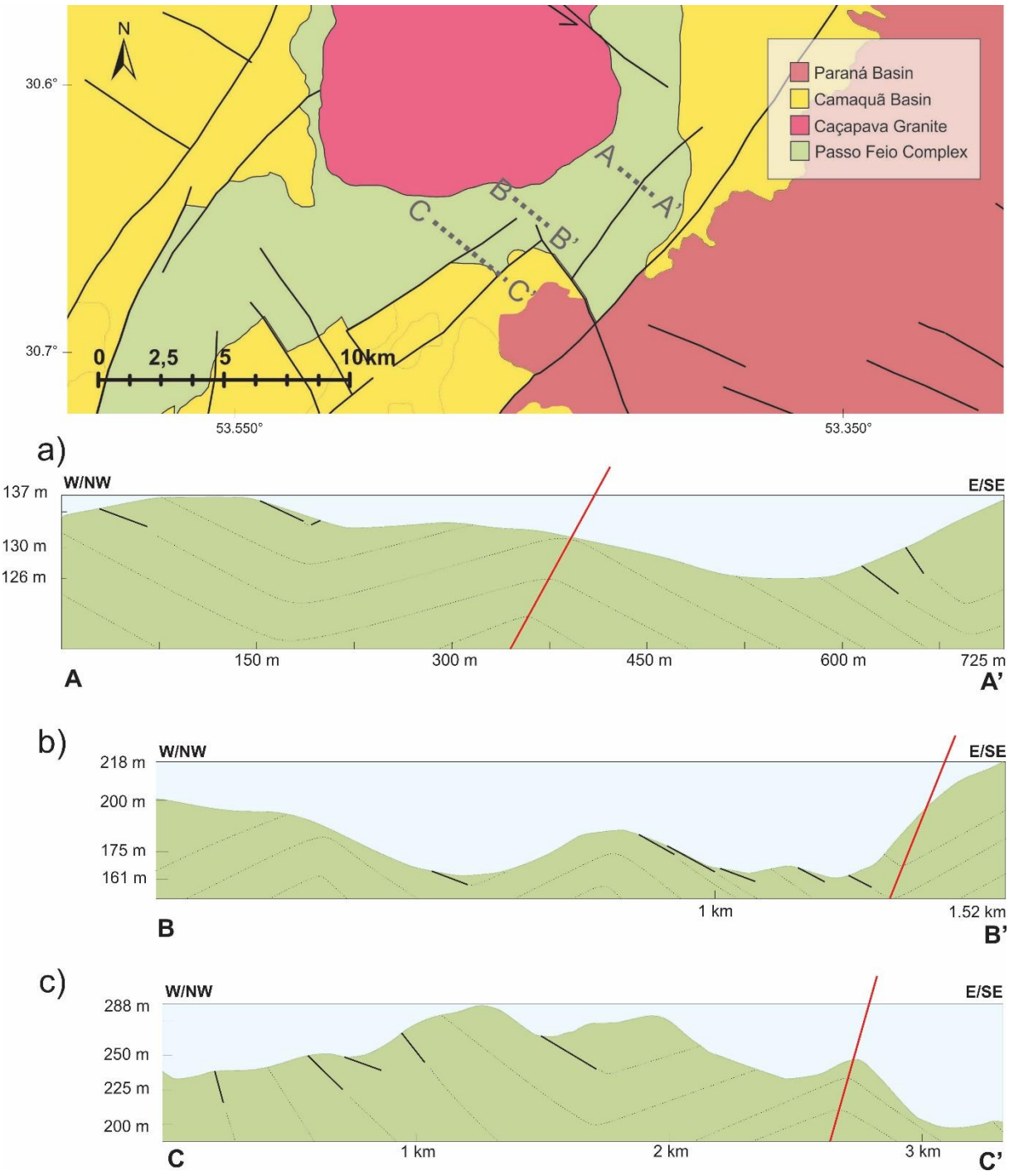

Fig. 3.3 *Profiles of the PFC.* ***a)*** *Profile A-A',* ***b)*** *Profile B-B',* ***c)*** *Profile C-C'. Black lines – observed foliation; dotted lines – projected S_1 fabric; red lines – fold axial planes.*

3.2 Sample introduction

Six samples from the Passo Feio Complex were chosen for geothermobarometry and studied in detail during this research, all of them collected from the southern/southeastern part of the complex (Fig. 3.4).

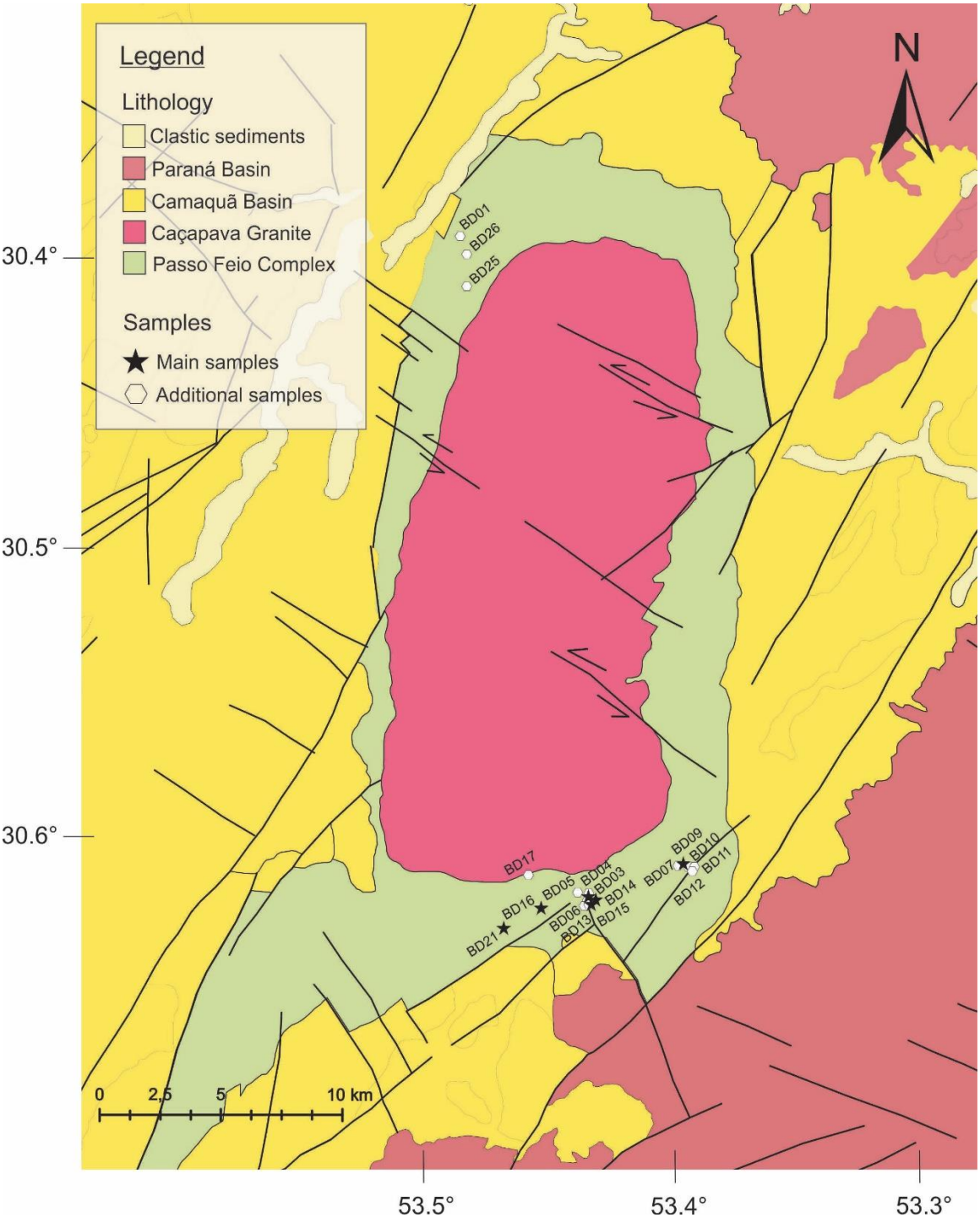

Fig. 3.4 *Map of study area and sample locations. Thick black lines – faults; Clastic sediments – Ceonozoic; Paraná Basin – Paleoozoic; Camaquã Basin – Neoproterozoic; Caçapava Granite – Neoproterozoic; Passo Feio Complex – Neoproterozoic.*

Sample BD03 (S30.643889°, W53.453333°) is a staurolite-garnet schist from the southern-southeastern part of the Passo Feio Complex. The hand specimen (Fig. 3.5a) is dark grey with staurolite (~2 mm) and garnet (~1 mm) porphyroblasts in a fine-grained matrix. Intercalated quartz-rich layers can be observed throughout the sample, all very thin (< 1-2 mm) and relatively parallel with the main foliation.

Sample BD09b (S30.631667°, W53.418056°) is a staurolite-garnet schist from the southeastern part of the Passo Feio Complex. The hand specimen (Fig. 3.5b) is brownish grey with approximately 2 mm large garnet porphyroblasts in a fine-grained matrix.

Sample BD14 (S30.646667°, W53.452222°) is a garnet schist from the southern-southeastern part of the Passo Feio Complex. The hand specimen (Fig. 3.5c) is greenish grey with porphyroblasts of garnet (~1 mm) in a fine-grained matrix. The slightly wavy foliation contains very thin (< 1 mm) quartz-rich layers.

Sample BD15 (S30.645000°, W53.450556°) is a mica schist from the southern-southeastern part of the Passo Feio Complex. The matrix is very fine-grained and greyish in color with ~1-2 mm large porphyroblasts of garnet (Fig. 3.5d). Pearly lustre is present in mica-rich layers of the sample.

Sample BD16c (S30.648100°, W53.470817°) is a garnet-mica schist from the southern part of the Passo Feio Complex. The hand specimen (Fig. 3.5e) is very fine-grained and greenish grey in color, with some small garnet porphyroblasts (< 1 mm). The phyllite consists of thin laminae of the matrix minerals quartz, muscovite and biotite, as a small-scale sequence of very fine layers.

Sample BD21 (S30.655556°, W53.484722°) is a phyllite from the southern part of the Passo Feio Complex. The hand specimen (Fig. 3.5f) is light brownish grey and very fine-grained with thin laminae of quartz, muscovite and biotite. There is a relatively high proportion of opaque minerals present, compared to the other samples.

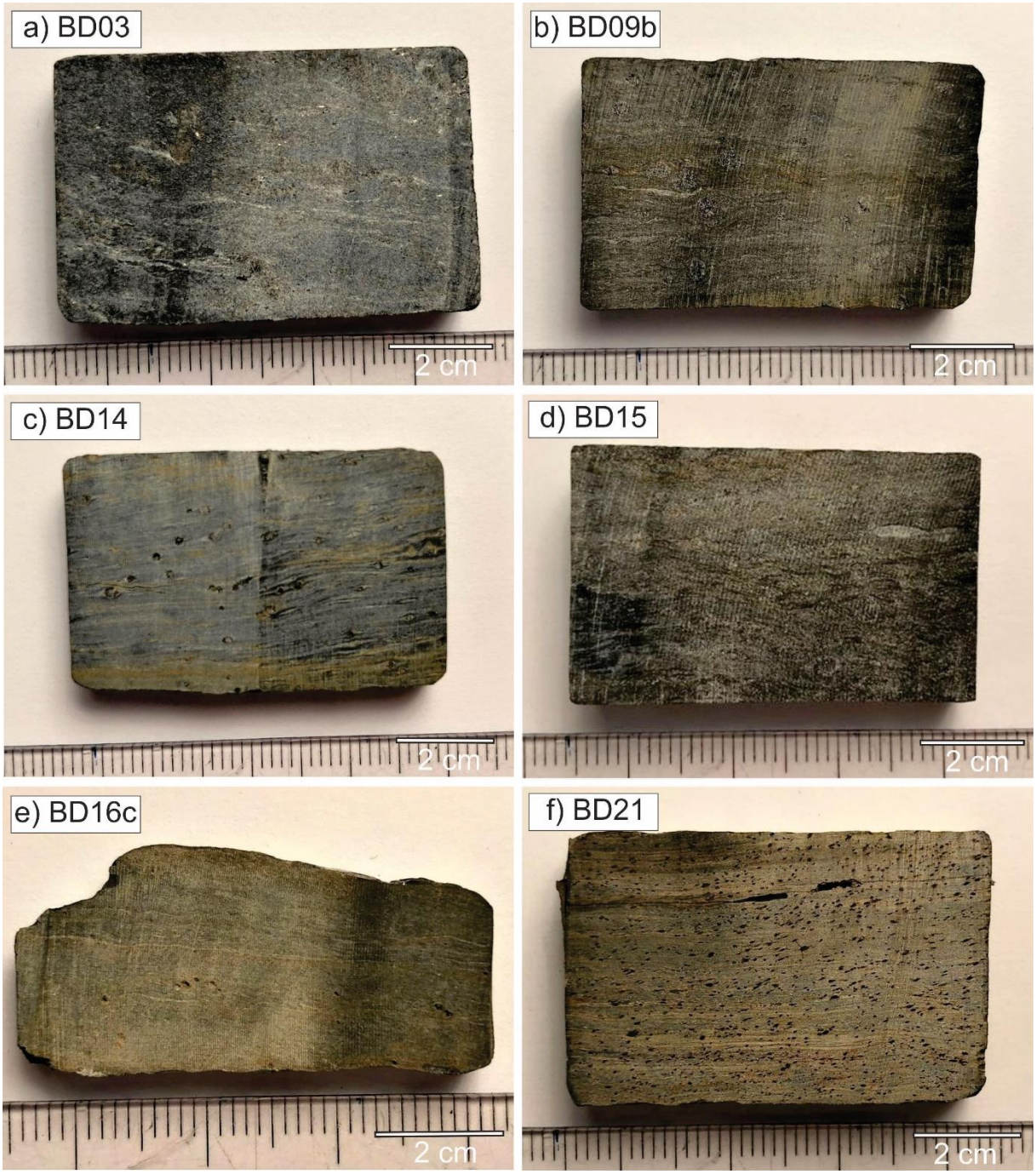

Fig. 3.5 *Photographs showing macroscopic appearance of the studied samples.*

3.3 Whole rock chemistry

Two sets of analyses were conducted. One set of analyses was made by the local XRF at the Department of Geosciences at the University of Tromsø. The same samples were also sent to the Bureau Veritas laboratories in Vancouver, Canada, for a quality control. Results of the whole rock chemical analysis of the studied samples are listed below in Table 3.1 and Table 3.2. The first table is the one used as system composition for modelling of the samples, while the latter is a cross-check set of analyses for comparison.

Table 3.1 *Whole rock chemical composition of samples used for thermodynamic modelling, determined by XRF analysis in the laboratories at the University of Tromsø.*

	BD03	BD09B	BD14	BD15	BD16C	BD21
Wt. %						
SiO2	64,13	54,99	61,49	55,09	61,42	56,32
TiO2	0,96	1,87	1,07	1,46	0,95	1,66
Al2O3	15,61	18,51	20,93	17,63	19,75	19,99
FeO	7,95	13,92	6,99	13,42	7,95	13,20
MnO	0,12	0,16	0,20	0,33	0,13	0,11
MgO	3,13	2,17	1,33	2,82	1,87	0,81
CaO	1,53	1,05	0,22	1,30	0,03	0,12
Na2O	1,81	1,44	0,97	1,43	0,35	0,98
K2O	2,60	2,72	3,89	2,97	5,49	3,77
P2O5	0,16	0,42	0,09	0,57	0,08	0,08
LOI	1,29	2,62	4,18	2,39	4,24	3,67
Total	99,28	99,87	101,36	99,41	102,25	100,70

The loss on ignition (LOI) was calculated by the following equation:

$$LOI = \frac{\left(W^{\text{f.gl.}}_{\text{pr+dig}} - W^{\text{e.gl.}}_{\text{pr.+dig.}} \right) \bullet 100}{W_{\text{pr}}}$$

where $W^{f.gl}_{pr+dig}$ is weight of sample and crucible before ignition, $W^{e.gl}_{pr+dig}$ is weight of sample and crucible after ignition, and W_{pr} is the weight of the sample before ignition.

Table 3.2 *Whole rock chemistry of samples conducted by the Bureau Veritas laboratories in Vancouver, Canada.*

	BD03	BD09B	BD14	BD15	BD16C	BD21
Wt. %						
SiO2	63,67	54,04	59,65	54,04	58,57	54,62
TiO2	0,97	1,83	1,07	1,49	0,94	1,65
Al2O3	15,83	18,29	20,61	17,74	19,42	19,67
Fe2O3	8,65	15,08	7,71	14,59	8,72	14,38
MnO	0,11	0,15	0,19	0,33	0,12	0,1
MgO	3,1	2,12	1,25	2,8	1,76	0,7
CaO	1,54	1,04	0,22	1,3	0,03	0,12
Na2O	1,74	1,38	0,9	1,38	0,29	0,93
K2O	2,58	2,69	3,84	2,94	5,36	3,72
P2O5	0,15	0,4	0,08	0,54	0,06	0,07
Cr2O3	0,052	0,03	0,017	0,022	0,016	0,022
LOI	1,40	2,60	4,10	2,60	4,40	3,80
Total	99,91	99,86	99,92	99,87	99,91	99,92

3.4 Optical petrography and mineral chemistry

Petrographic observations of the samples are presented together with their representative mineral compositions. A brief description of additional samples collected from the Passo Feio Complex is also presented for later discussion of the regional changes of metamorphic grade.

3.4.1 Sample BD03

Sample BD03 consists of approximately 2 mm large porphyroblasts of staurolite (~15 %) and < 1 mm large porphyroblasts of garnet (~5-10 %) in a medium-grained matrix of muscovite (~15 %), biotite (~15 %), plagioclase (~5 %), quartz (~30 %), chlorite (~5 %) and ilmenite (~1 %) with minor amounts of pyrrhotite, apatite and zircon (< 1 %). The main foliation is defined by the shape preferred orientation of the micas (Fig. 3.6).

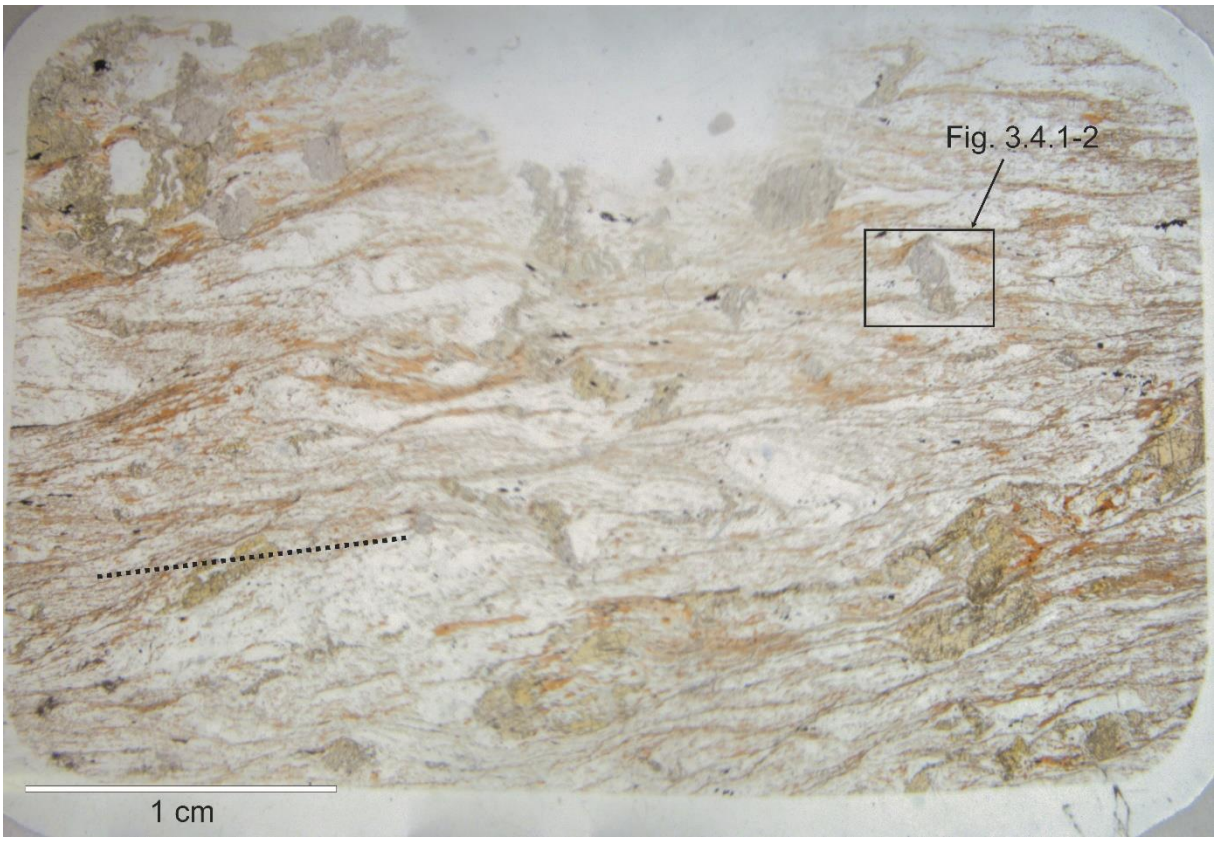

Fig. 3.6 *Overview photomicrograph of the thin section of sample BD03 in PPL. Black dotted line – main foliation (S_1).*

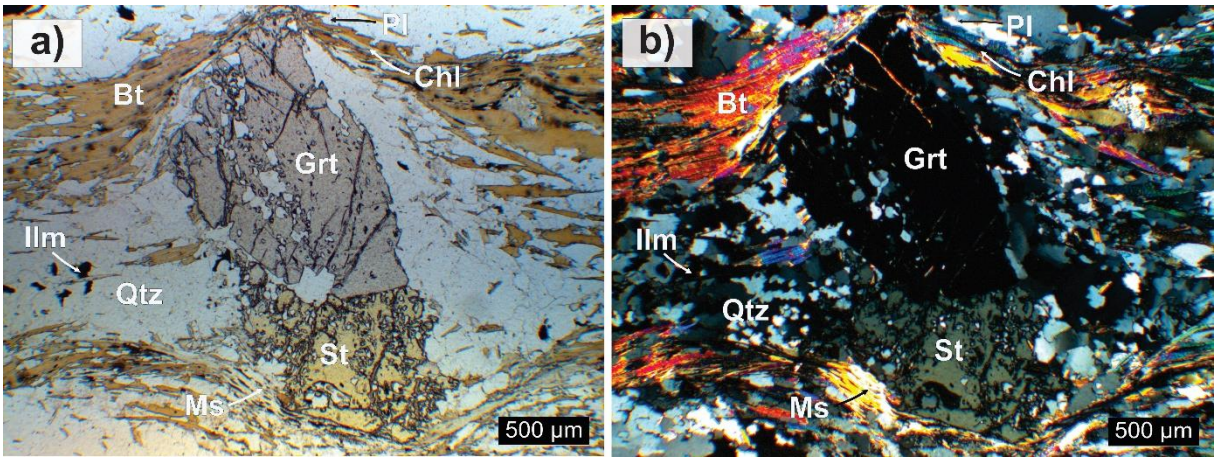

Fig. 3.7 *Photomicrographs of the sample BD03. The photomicrographs show representative minerals of the sample in* ***a)*** *PPL and* ***b)*** *XPL.*

Anhedral garnets (Fig. 3.7) display numerous inclusions of quartz, ilmenite and apatite, and some grains also display a minor amount of pyrrhotite inclusions. Measurements of garnet cores show X_{Mg} values between 0.10-0.11 and the following endmember proportions: X_{Prp} values of 0.07, X_{Alm} values of 0.59-0.63, X_{Grs} values of 0.07-0.08 and X_{Sps} values of 0.18-0.19. The chemistry changes towards the rims, where the respective values are as follows: X_{Mg} = 0.12-0.13, X_{Prp} = 0.09-0.11, X_{Alm} = 0.65-0.73, X_{Grs} = 0.06-0.08 and X_{Sps} = 0.08-0.12. There is a decrease in the endmember proportions of spessartine and grossular from core to rim, while there is an increase of pyrope and almandine. The amount of manganese is slightly decreasing and calcium is relatively stable from core to rim, while the amount of magnesium and iron is increasing. The X_{Mg} value is slightly increasing.

Chlorite is present in some cracks within garnet grains, but also in thin layers parallel to muscovite and biotite where it is mostly concentrated near the grain boundaries towards garnet or staurolite. Chlorite has X_{Mg} values between 0.51-0.53. Biotite has X_{Mg} values between 0.44 and 0.51 and muscovite has a Si content of 3.02-3.04 a.p.f.u. The $K^+/(K^+ + Na^+)$ ratio in muscovite is 0.82-0.84. Ilmenite has a Ti^{4+} and Fe^{2+} content of 1.00-1.01 and 0.0.94-0.96 a.p.f.u. respectively, corresponding to a pure ilmenite endmember. Staurolite has X_{Mg} values of 0.16-0.20.

Anhedral plagioclase does not show twinning, cleavage or zoning, and it was identified during SEM analysis. The proportions of feldspar endmembers in the measured plagioclase grains are 31-33 % anorthite, 66-68 % albite and < 1 % K-feldspar. The measured plagioclase grains therefore classify as andesine.

3.4.2 Sample BD09b

Sample BD09b consists of porphyroblasts of garnet (~10 %) and staurolite (~10 %) in a fine- to medium-grained matrix of muscovite (~15 %), biotite (~20 %), quartz (~25 %), plagioclase (~5 %), ilmenite (~5 %), andalusite (~5 %) and minor amounts of tourmaline (~1 %).

Fig. 3.8 shows an overview photomicrograph of sample BD09b, where the main foliation (S_1) is indicated by the orientation of micas and marked with a red line. Garnet porphyroblasts differ in size, from < 1 mm to approximately 3 mm, where the largest ones contain the highest amount of inclusions. Among these are quartz, ilmenite and apatite. Ilmenite is also widely distributed throughout the matrix of the rock, with a Ti^{4+} and Fe^{2+} content of 1.01 and 0.98 a.p.f.u., respectively.

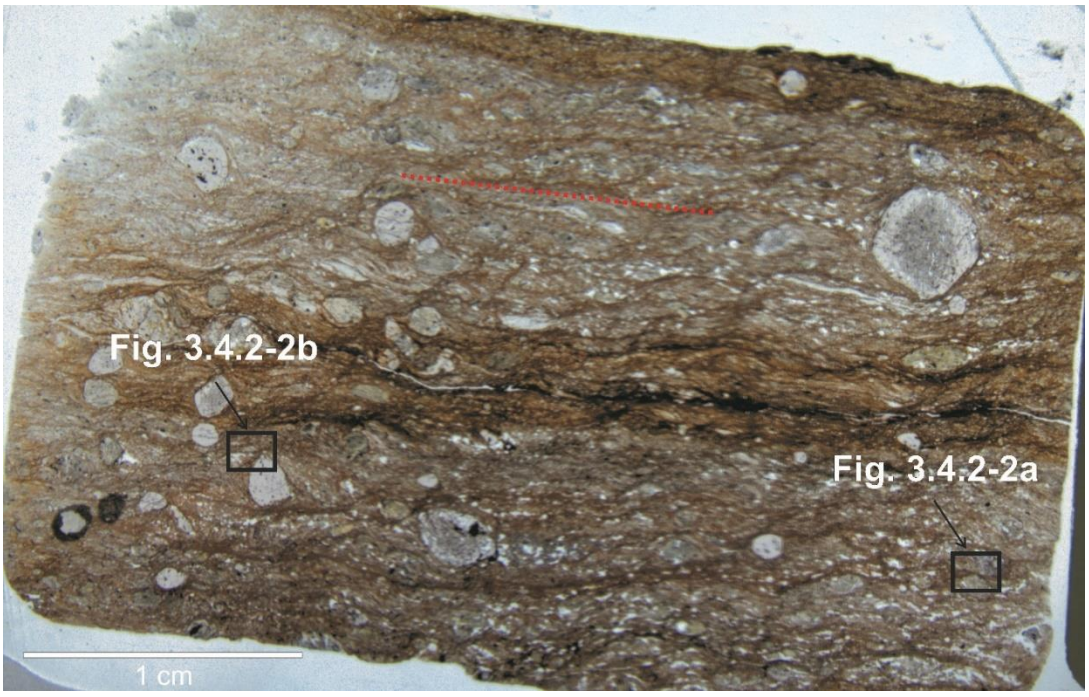

Fig. 3.8 *Overview photomicrograph of the thin section of sample BD09b in PPL. Red dotted line – main foliation (S_1).*

Anhedral garnet in the sample BD09b is rich in almandine component and has the following core composition in endmember proportions: X_{Prp} = 0.04-0.07, X_{Alm} = 0.74-0.82, X_{Grs} = 0.04, X_{Sps} = 0.03-0.11. The X_{Mg} core value is 0.06-0.08. The composition changes towards the rims, where the X_{Mg} value is 0.08, and the endmember proportions are as follows: X_{Prp} = 0.07-0.08, X_{Alm} = 0.82-0.86, X_{Grs} = 0.03-0.04, X_{Sps} = 0.01-0.02. This is the same trend as in the sample BD03, where the Mg- and Fe-content increases while the Mn content decreases and the Ca-content is relatively stable throughout the grain. The X_{Mg} value slightly increases from 0.06-0.08 to 0.08.

Anhedral plagioclase grains have the following proportions of feldspar endmembers: 13 % anorthite, 86 % albite and less than 1 % K-feldspar, and classify as oligoclase. Biotite has an X_{Mg} value of 0.33-0.34, while muscovite grains are too fine-grained for microprobe analysis. Staurolite has an X_{Mg} value of 0.11-0.13.

Fig. 3.9 show garnet and staurolite porphyroblasts and the fine-grained matrix. Andalusite grains are surrounding staurolite (Fig. 3.9b) and suggest replacement of the latter.

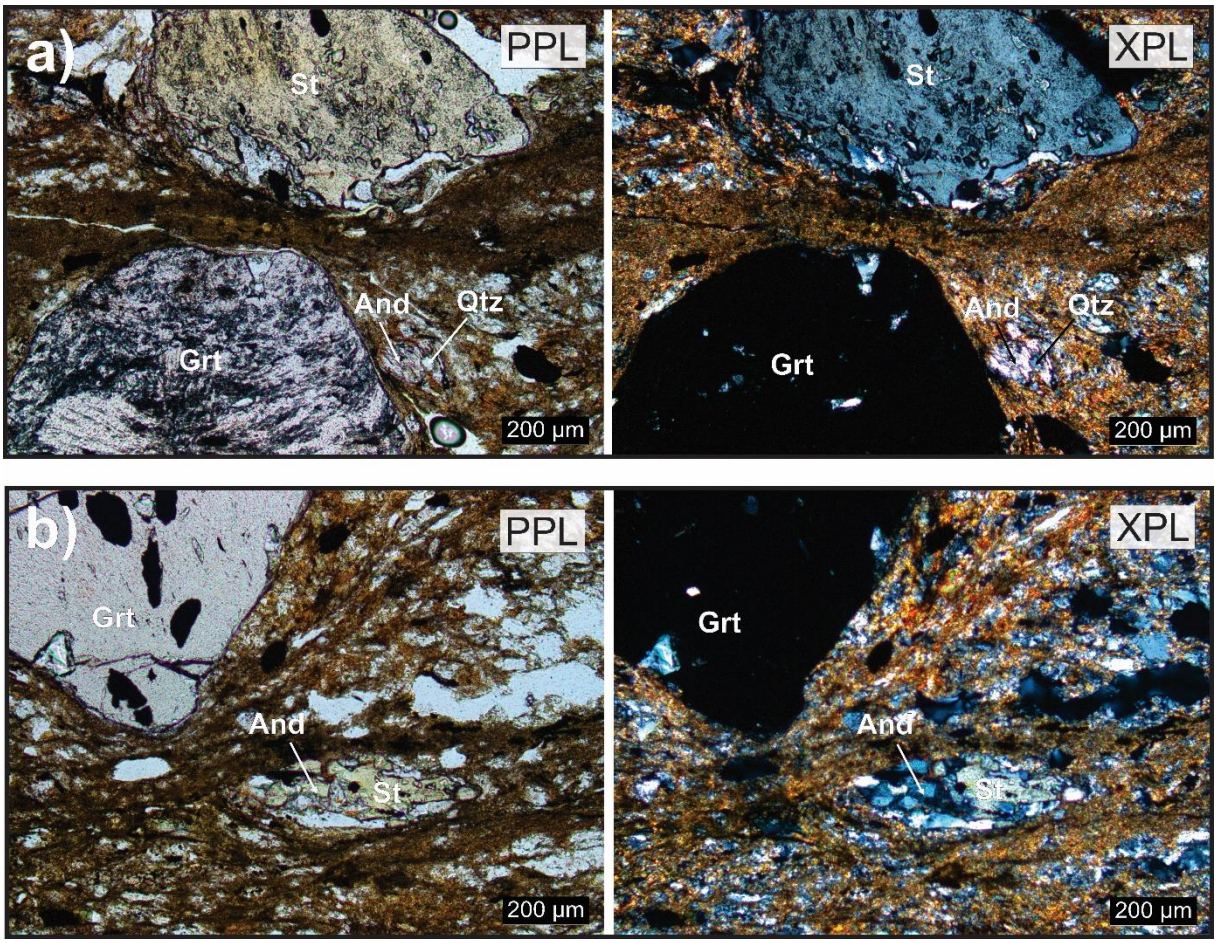

Fig. 3.9 *Photomicrographs of the sample BD09b.*

3.4.3 Sample BD14

Sample BD14 consists of porphyroblasts of garnet (~10 %) and staurolite (~5 %) in a fine- to medium-grained matrix of muscovite (~20 %), biotite (~20 %), quartz (~30 %), plagioclase (~5 %) and ilmenite (5-10 %).

Fig. 3.10 shows a porphyroblast of garnet together with surrounding matrix. The thin layers of muscovite and biotite wrap around the garnet grain, implying pre- to syn-tectonic origin of the porphyroblasts. A profile from core (a) to rim (b) is marked in red, where a point analysis with SEM was conducted.

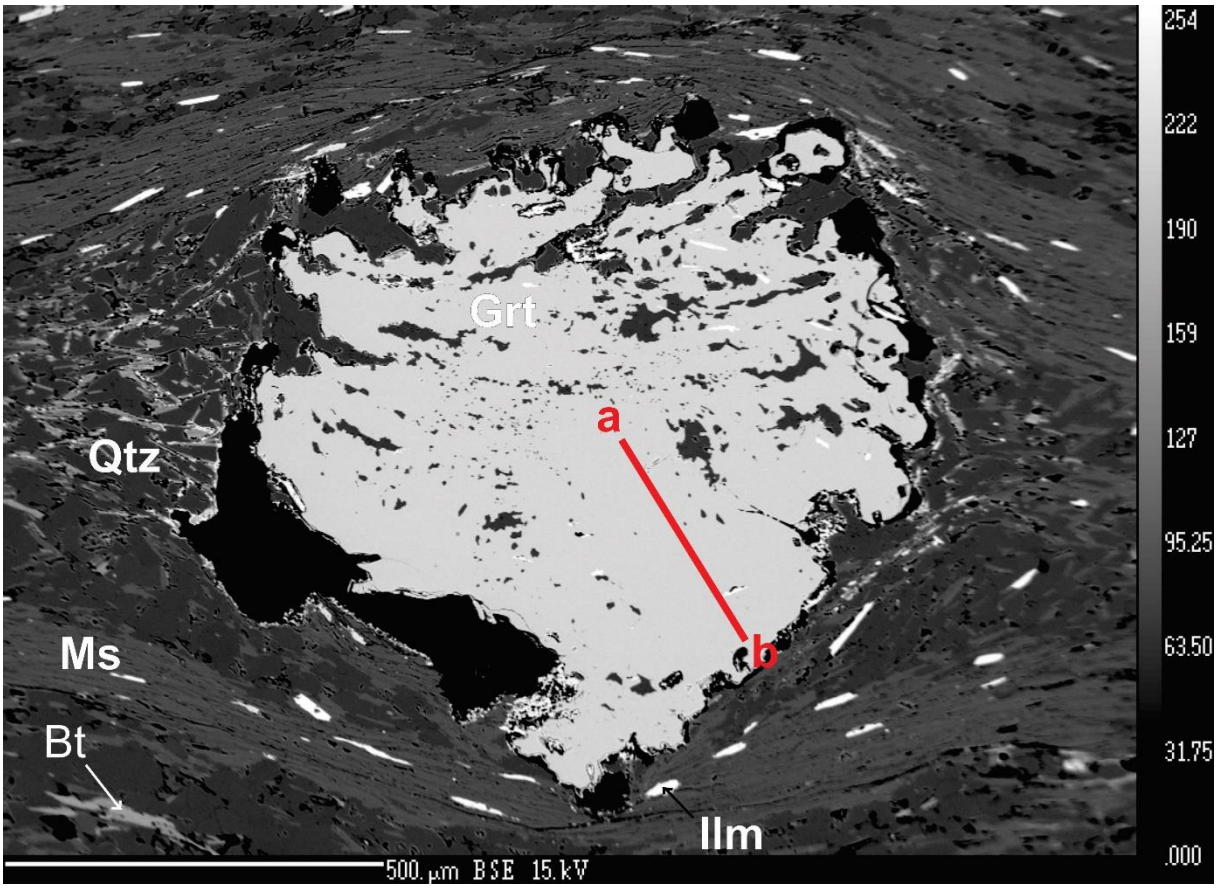

Fig. 3.10 *SEM image of a garnet grain in sample BD14. Line a-b – point analysis of garnet grain from core to rim.*

The garnet grain in Fig. 3.10 has the following core-to-rim range (line a to b) in endmember proportions: X_{Prp} = 0.04-0.07, X_{Alm} = 0.59-0.81, X_{Grs} = 0.07-0.08, X_{Sps} = 0.25-0.04. The core-to-rim range in X_{Mg} is 0.06-0.08.

An element map of the garnet grain (Fig. 3.11) shows the same compositional trends as in the previous samples. The Ca-content is more or less constant throughout the garnet grain, while the Fe- and Mg-content increases from core to rim. The Mn-content is decreasing towards the rim.

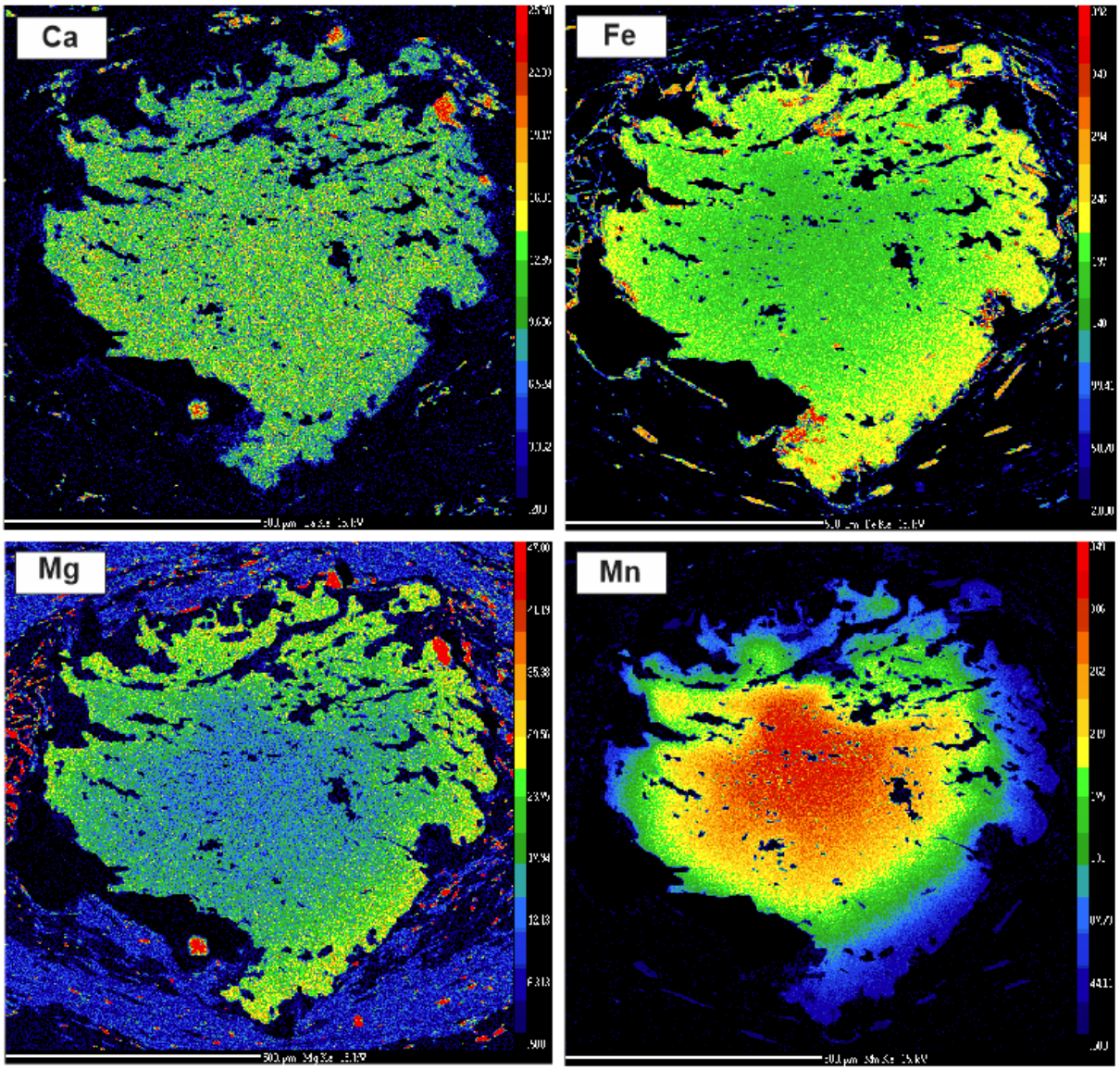

Fig. 3.11 *Garnet element maps of the sample BD14. Images are constructed through SEM analysis at the University of Oslo.*

Numerous inclusions of quartz and ilmenite are present within the anhedral garnet grains in sample BD14. Ilmenite is homogeneously distributed in the sample with an elongation parallel with the foliation defined by shape preferred orientation of muscovite and biotite. The orientation of elongated ilmenite inclusions within garnet grains is however different from that of the main foliation, implying a pre- to syn-kinematic growth of garnet in the sample.

Small anhedral plagioclase grains were identified during SEM analysis, containing the following proportions of feldspar endmembers: 21 % anorthite, 79 % albite and less than 1 % K-feldspar. It classifies as oligoclase.

Thin layers of muscovite follow the main foliation, with a Si content of 3.01-3.06 a.p.f.u. and a $K^+/(K^+ + Na^+)$ ratio of 0.75-0.79. Staurolite porphyroblasts have X_{Mg} values between 0.12-0.14.

3.4.4 Sample BD15

Sample BD15 consists of porphyroblasts of garnet (~10-15 %) and some smaller crystals of staurolite (~5 %) in a medium-grained matrix of muscovite (~15 %), biotite (~20 %), plagioclase (~5 %), quartz (~30 %), chlorite (~5 %) and ilmenite (~5 %).

Biotite and muscovite layers wrap around the garnet crystals, and inclusions of ilmenite and quartz are elongated in the direction of the main foliation (Fig. 3.11). The Si content of muscovite is between 3.03-3.05 a.p.f.u. and the $K^+/(K^+ + Na^+)$ ratio is 0.76-0.81. Staurolite has an X_{Mg} value of 0.11-0.15.

The subhedral to anhedral garnet grains (Fig. 3.13) have the following endmember proportions present in the garnet cores: X_{Prp} = 0.04-0.07, X_{Alm} = 0.66-0.79, X_{Grs} = 0.05-0.06, X_{Sps} = 0.04-0.17. The X_{Mg} value is 0.06-0.08. The garnet composition in the rims changes to X_{Prp} = 0.07-0.08, X_{Alm} = 0.78-0.84, X_{Grs} = 0.03-0.04, X_{Sps} = 0.03-0.04 and an X_{Mg} value between 0.08 and 0.09.

The compositional change from core to rim in the garnet grains has the same pattern as the previous samples. Fe- and Mg-content is increasing, Mn-content is decreasing and there is a more or less constant content of Ca as well as the X_{Mg} value.

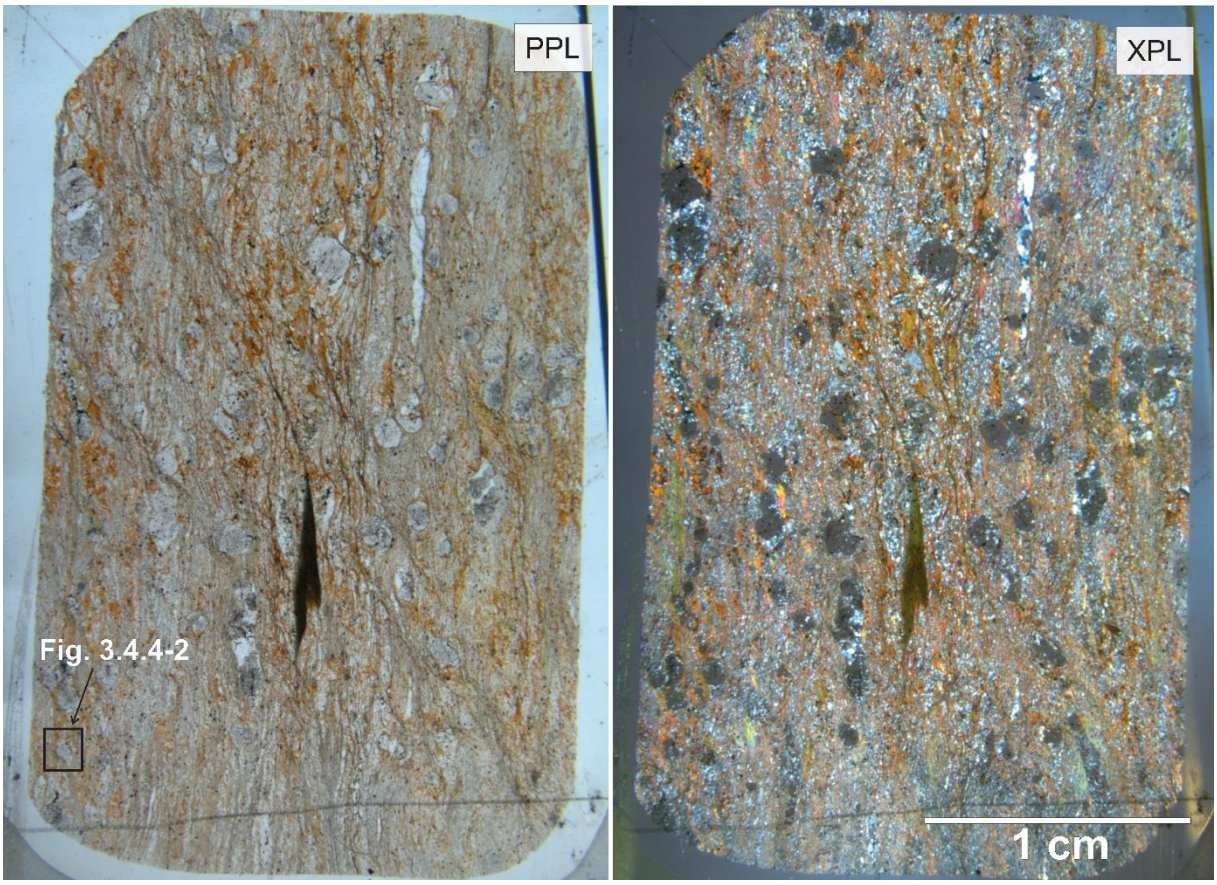

Fig. 3.12 *Overview photomicrograph of the thin section of sample BD15. The image is presented in both PPL (left) and XPL (right).*

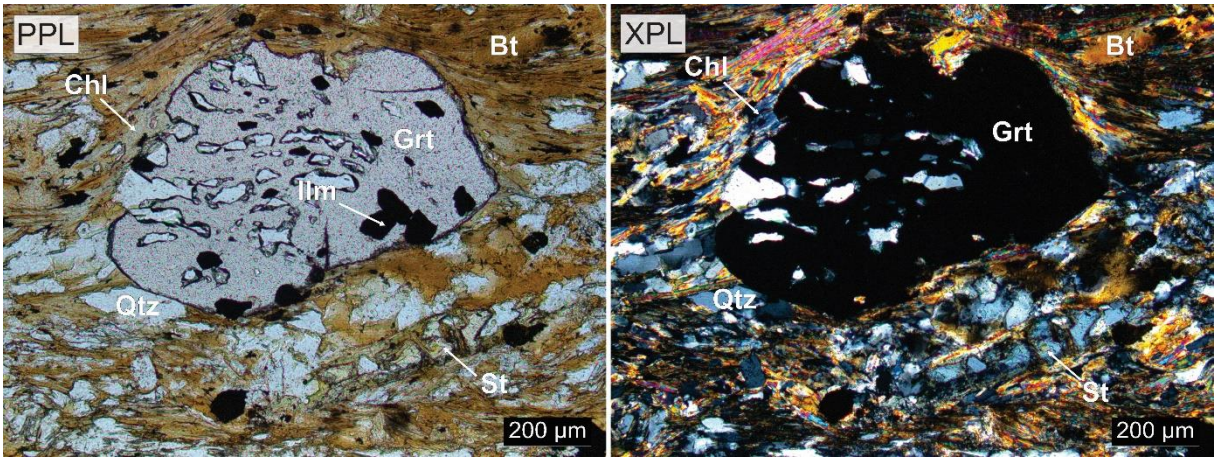

Fig. 3.13 *Photomicrograph of the sample BD15. The image is presented in PPL (left) and XPL (right).*

3.4.5 Sample BD16c

Sample BD16c consists of porphyroblasts of garnet (~5 %) in a fine-grained matrix of biotite (~30 %), muscovite (~20 %), quartz (~30 %), chlorite (~5 %), plagioclase (~5 %) and ilmenite (~1 %).

The main foliation is defined by the direction of the elongated layers of mica (Fig. 3.14). The subhedral garnet porphyroblasts are small, less than 1 mm in diameter, and their modal proportion in the sample is low. There is a high number of inclusions within the garnet grains, and among these are quartz, ilmenite and plagioclase.

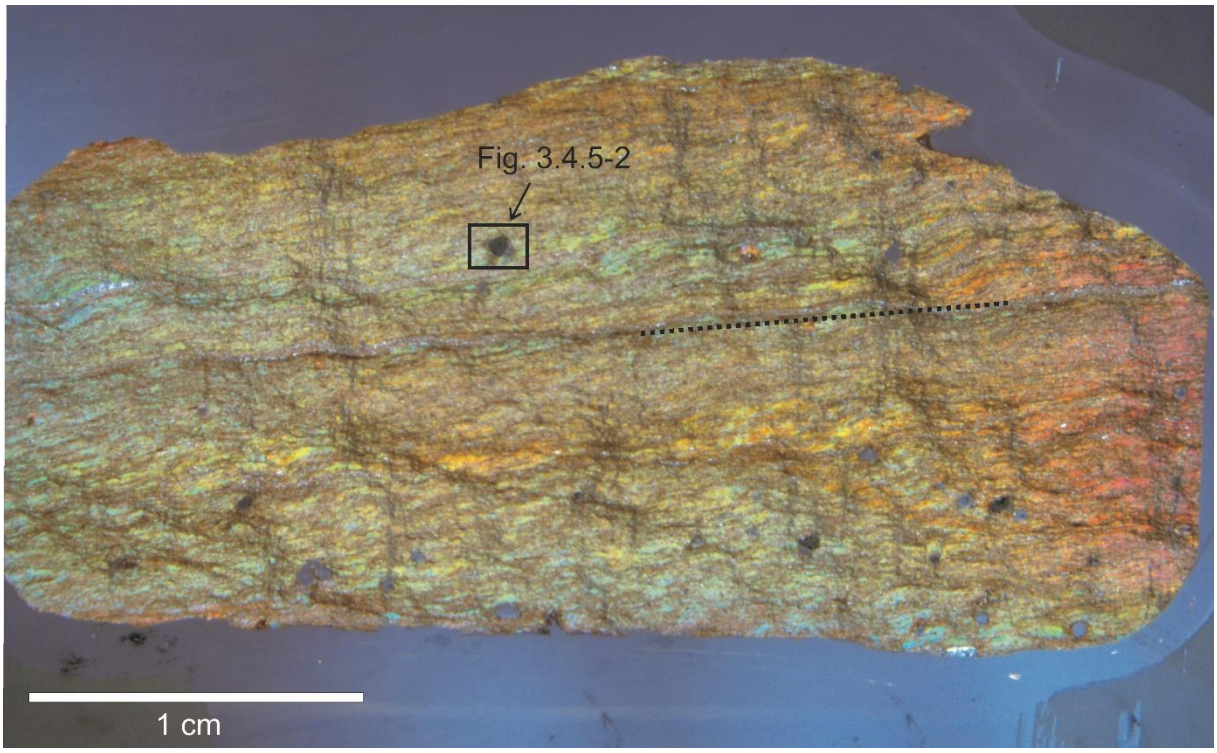

Fig. 3.14 *Overview photomicrograph of the thin section of sample BD16c in XPL. Black dotted line – orientation of main foliation.*

The endmember proportions of garnet differ from core to rim, where the amount of X_{Prp} changes from 0.03 in the core to 0.03-0.04 in the rims, X_{Alm} from 0.34-0.51 to 0.53-0.58, X_{Grs} changes slightly from 0.08-0.10 to 0.07-0.11 and X_{Sps} from 0.31-0.34 to 0.22-0.30. The X_{Mg} value remains 0.06-0.07 throughout the garnet grains measured.

The thin layers of muscovite and biotite together with the small grains of quartz wrap around the garnet grain (Figure 3.4.5-2), implying that the garnet grain was already present during dynamic (re)crystallization of the matrix. Elongated ilmenite inclusions are present in a different orientation than the main foliation of the matrix, pointing again to syn-kinematic growth of the garnet porphyroblasts.

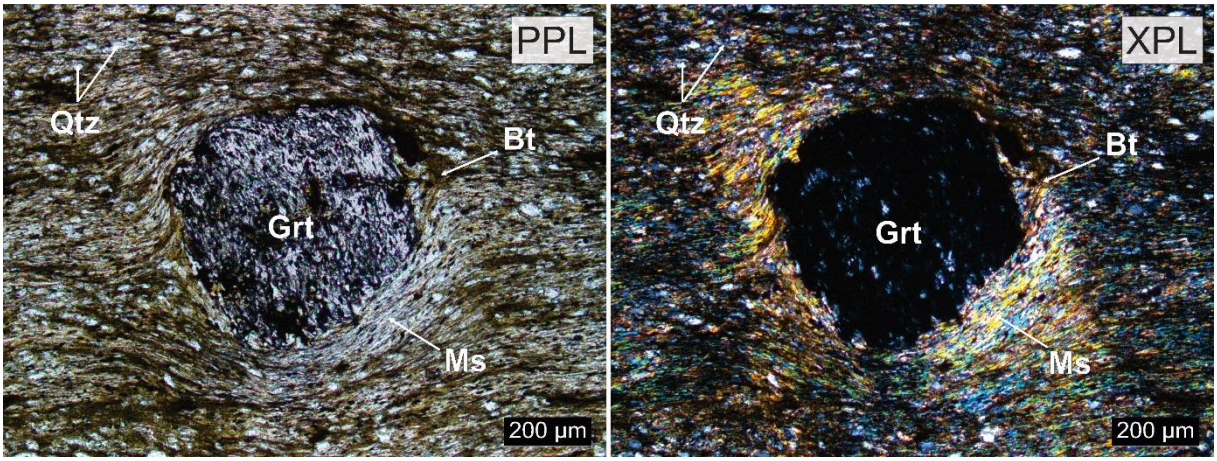

Fig. 3.15 *Photomicrograph of the sample BD16c. The image is shown in both PPL (left) and XPL (right).*

3.4.6 Sample BD21

Sample BD21 mainly consists of the mineral assemblage muscovite (~20 %), biotite (~30 %), plagioclase (~1-5 %), chlorite (~5 %), quartz (~30 %), ilmenite (~5-10 %) and accessory hematite (< 1 %).

The sample is very fine-grained and contains somewhat larger amount of opaque minerals than the other samples. Both ilmenite and hematite were identified during analysis, both in different sizes throughout the sample. A measured grain of hematite has a Fe^{3+} content of 0.98 a.p.f.u., corresponding to a pure hematite endmember. Thin muscovite layers (Fig. 3.16) with an Si content between 3.00-3.08 a.p.f.u. and $K^+/(K^+ + Na^+)$ ratio of 0.72-0.75 define the foliation of the sample, together with the rest of the matrix minerals.

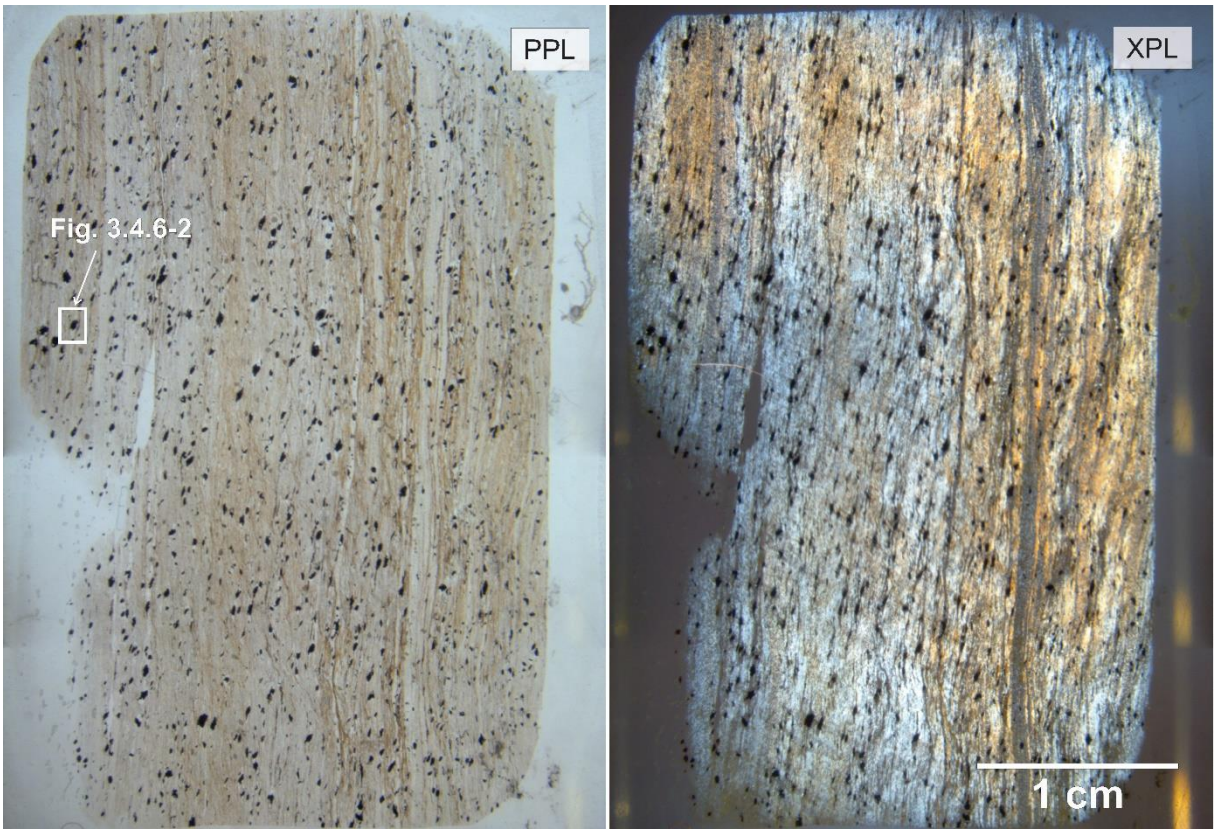

Fig. 3.16 *Overview microphotograph of the thin section of sample BD21. The thin section is presented in both PPL (left) and XPL (right).*

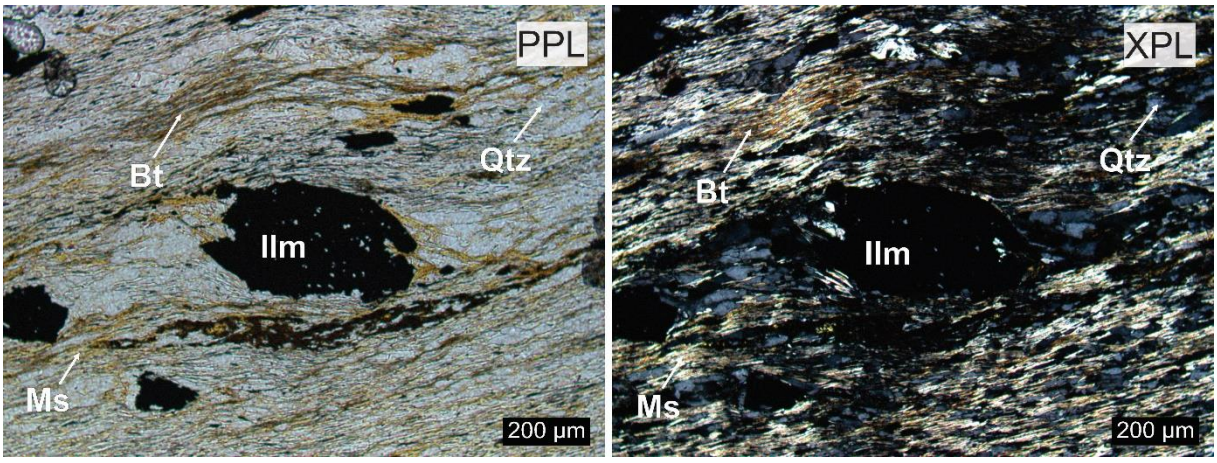

Fig. 3.17 *Microphotograph of the sample BD21. The image is presented in both PPL (left) and XPL (right).*

Unfortunately, the quality of the thin section of sample BD21 have not permitted good results. Due to e.g. big holes among other things, it is not possible do provide any further description and measurements were sparse.

3.4.7 Additional samples

Additional samples from the Passo Feio Complex involve eighteen samples that were not selected for thermobarometry due to inappropriate mineral assemblage or due to strong alteration. These are presented together with the main samples in Fig. 3.4. Table 3.3 below presents the observed mineral assemblages of these samples. Note that some of the samples, as well as some outcrops where there were not collected samples, have a mineral assemblage that consists of andalusite.

Table 3.3 *Mineral assemblages observed in additional samples from the Passo Feio Complex. Sample locations are presented in Fig. 3.4.*

Sample	Rock type	Mineral assemblage	Coordinates
BD01a	Schist	Chl + Ms + Qtz + Pl + Zrn + Op	S 30.3999160°, W 53.500843°
BD01b	Schist	Ms + Pl + Qtz + Zrn + Op	S 30.3999160°, W 53.500843°
BD02a	Schist	Grt + St + Bt + Ms + Chl + Qtz + Ilm	S 30.645278°, W 53.453611°
BD02b	Schist	Grt + St + Bt + Ms + Chl +Pl + Qtz + Ilm	S 30.645278°, W 53.453611°
BD04	Quartzite	Qtz + Bt + Zrn + Op	S 30.642778°, W 53.453056°
BD05	Schist	Grt + St + Bt + Ms + Pl + Qtz + Ilm	S 30.642500°, W 53.457222°
BD06	Schist	Grt + St + Ms + Bt + Chl + Qtz + Ilm	S 30.647500°, W 53.454722°
BD07	Schist	Grt + St + Ms + Bt + Qtz + Pl + And + Ilm	S 30.632500°, W 53.420000°
BD09a	Schist	Grt + St + Ms + Bt + Qtz + And + Ilm	S 30.631667°, W 53.418056°
BD10	Schist	Grt + Pl + Ms + Bt + Qtz	S 30.632778°, W 53.416389°
BD12	Amphibolite	Hbl + Ep + Qtz + Rt + Act	S 30.634722°, W 53.414722°
BD13	Amphibolite	Hbl + Pl + Ep + Act	S 30.646944°, W 53.453056°
BD16a	Schist	Ms + Bt + Qtz + Ilm	S 30.648100°, W 53.470817°
BD16b	Schist	Ms + Bt + Qtz + Ilm	S 30.648100°, W 53.470817°
BD17a	Amphibolite	Ep + Qtz + Pl + Hbl	S 30.636111°, W 53.475556°
BD17b	Granite	Pl + Fsp + Qtz	S 30.636111°, W 53.475556°
BD25	Rhyolite	Pl + Qtz + Ms + Bt + Op	S 30.417778°, W 53.498333°
BD26	Rhyolite	Qtz + Fsp + Chl + Op	S 30.405833°, W 53.498333°

3.5 Phase equilibrium modelling

Phase equilibrium modelling by the Perple_X software package, version 6.8.5 (Connolly, 2005) was used to estimate the pressure and temperature (P-T) conditions of formation of the studied samples. The TC-DS633 version of the thermodynamic database of Holland & Powell (2011) was used together with the Holland & Powell (1991, 1998) equation of state for H_2O-CO_2 fluids. Whole-rock analyses of the studied samples (Table 3.1) were used as system compositions in the modelling.

For samples containing no or negligible amounts of Fe_2O_3-bearing minerals, the FeO values were calculated from Fe_2O_3 determined by XRF analysis by using formula (1).

(1) $FeO = Fe_2O_3 * 0.8998$

Calculations of P-T pseudosections were performed with H_2O as an independent saturated fluid phase.

3.5.1 BD03

Sample BD03 consists of garnet, staurolite, muscovite, biotite, quartz, plagioclase, chlorite and ilmenite. The system composition used for the modelling of this sample is (in wt. %): SiO_2 = 64.13, TiO_2 = 0.96, Al_2O_3 = 15.61, FeO = 7.95, MnO = 0.12, MgO = 3.13, CaO = 1.53, Na_2O = 1.81, K_2O = 2.60.

The P-T pseudosection was calculated in a temperature interval of 400-700°C and a pressure interval of 2.5-7.5 kbar (Fig. 3.18). Compositional isopleths for observed minerals in sample BD03 (Fig. 3.19 and Fig. 3.20) were plotted in order to find the best estimate of metamorphic P-T conditions.

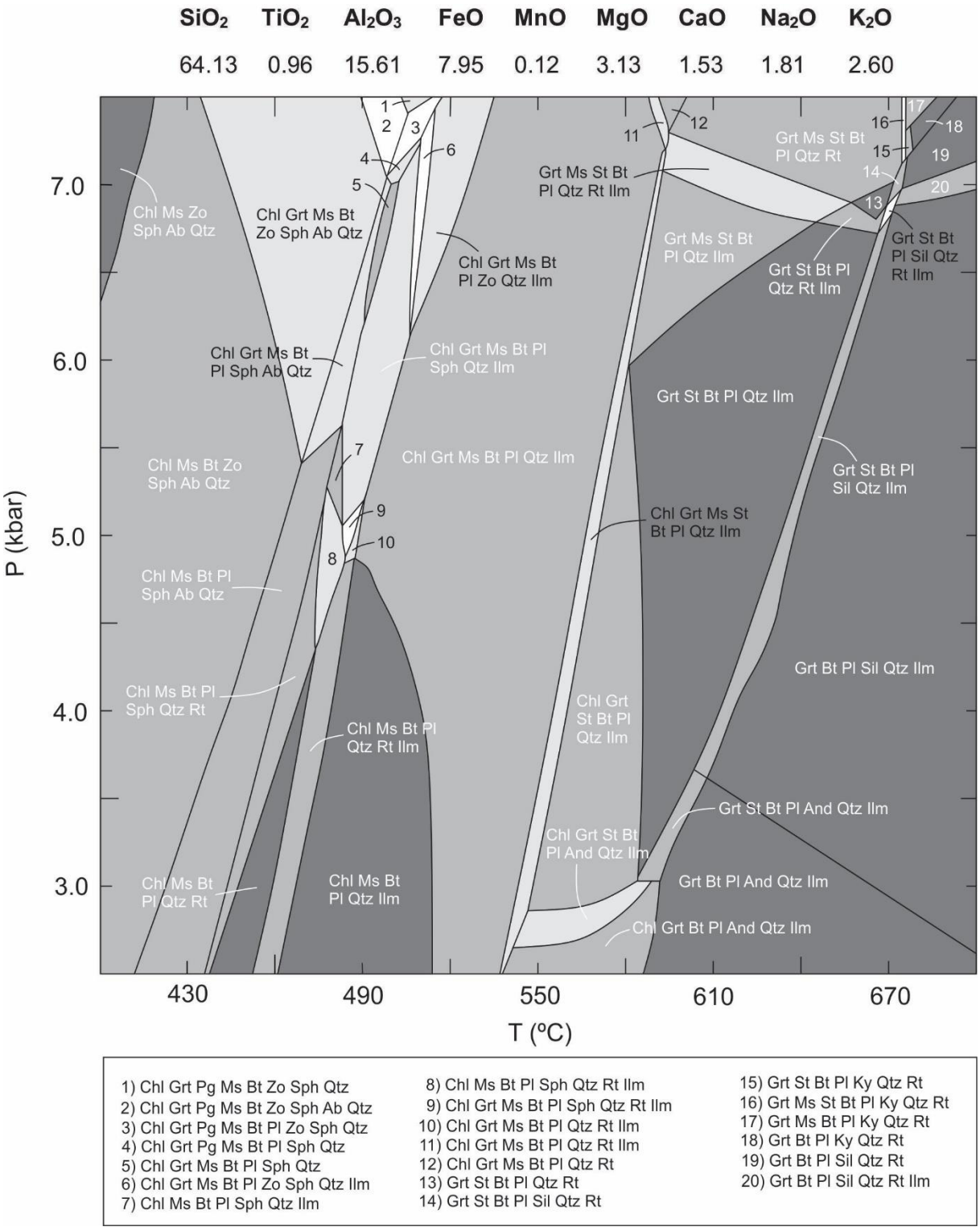

Fig. 3.18 *Calculated P-T pseudosection for the sample BD03. The bulk rock composition is indicated at the top as weight percentage of oxides.*

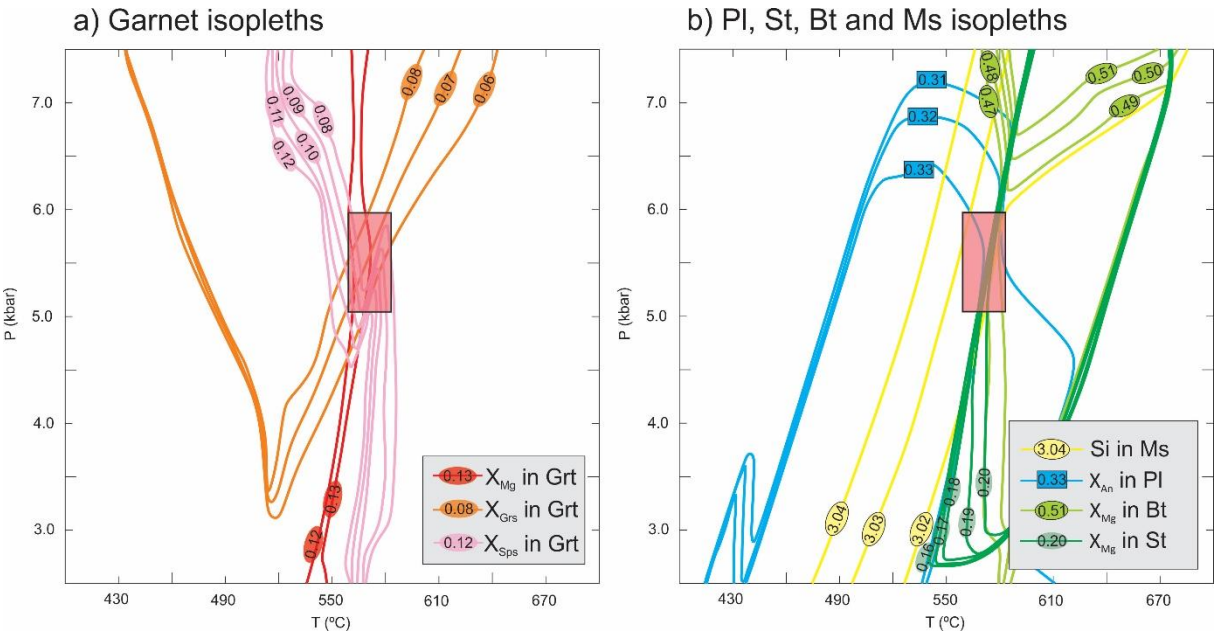

Fig. 3.19 *Compositional isopleths for the sample BD03.* ***a)*** *Compositional isopleths for garnet rims: Red – X_{Mg} values; orange – grossular (X_{Grs}); pink – spessartine (X_{Sps}). Red box – estimated P-T conditions.* ***b)*** *Compositional isopleths for matrix minerals: Blue – plagioclase (X_{An}); green – staurolite (X_{Mg}); light green - biotite (X_{Mg}); yellow – Si content in muscovite. Estimated P-T conditions are the same as in a).*

Compositional isopleths from garnet rims and matrix minerals are presented in Fig. 3.19. Fig. 3.19a shows the compositional isopleths for garnet rims, represented by X_{Mg} values together with the values for the compositional endmembers grossular (X_{Grs}) and spessartine (X_{Sps}). The compositional isopleths for the matrix minerals plagioclase (X_{An}), staurolite (X_{Mg}), biotite (X_{Mg}) and muscovite (Si) are presented in Fig. 3.19b. Isopleths in both Fig. 3.19a and Fig. 3.19b show the same stability field, as indicated by the red box that marks the area of shared stability between the isopleths. This is the estimated P-T conditions for the crystallization of sample BD03, where the temperature interval is approximately 560-585°C and the pressure interval is approximately 5-6 kbar.

Another P-T condition that is possible to calculate is the beginning of garnet growth, which may be estimated by plotting compositional isopleths for garnet core data. This is shown in Fig. 3.20, where the estimated core conditions are marked with a red circle in the area where the isopleths cross, which indicate a temperature of approximately 545°C and pressure of 4.4 kbar.

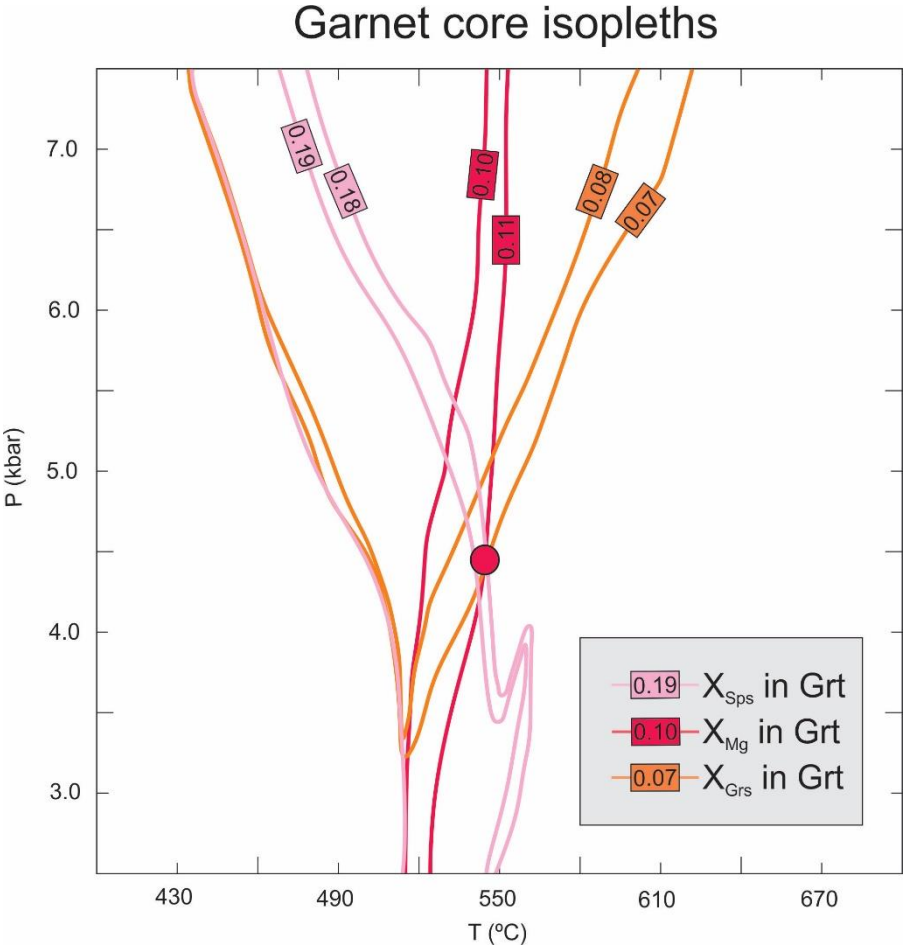

Fig. 3.20 *Compositional isopleths for garnet cores in the sample BD09b. Red circle – estimated P-T conditions for the onset of garnet growth.*

Both P-T conditions for the beginning of garnet growth (Fig. 3.20) and P-T conditions for the crystallization of the matrix minerals (Fig. 3.19) in sample BD03 are indicated in Fig. 3.21. The mineral assemblage chlorite-garnet-muscovite-staurolite-biotite-plagioclase-quartz-ilmenite is stable within the estimated P-T conditions for crystallization (red box), and this is consistent with the observed data from optical petrography and SEM analysis.

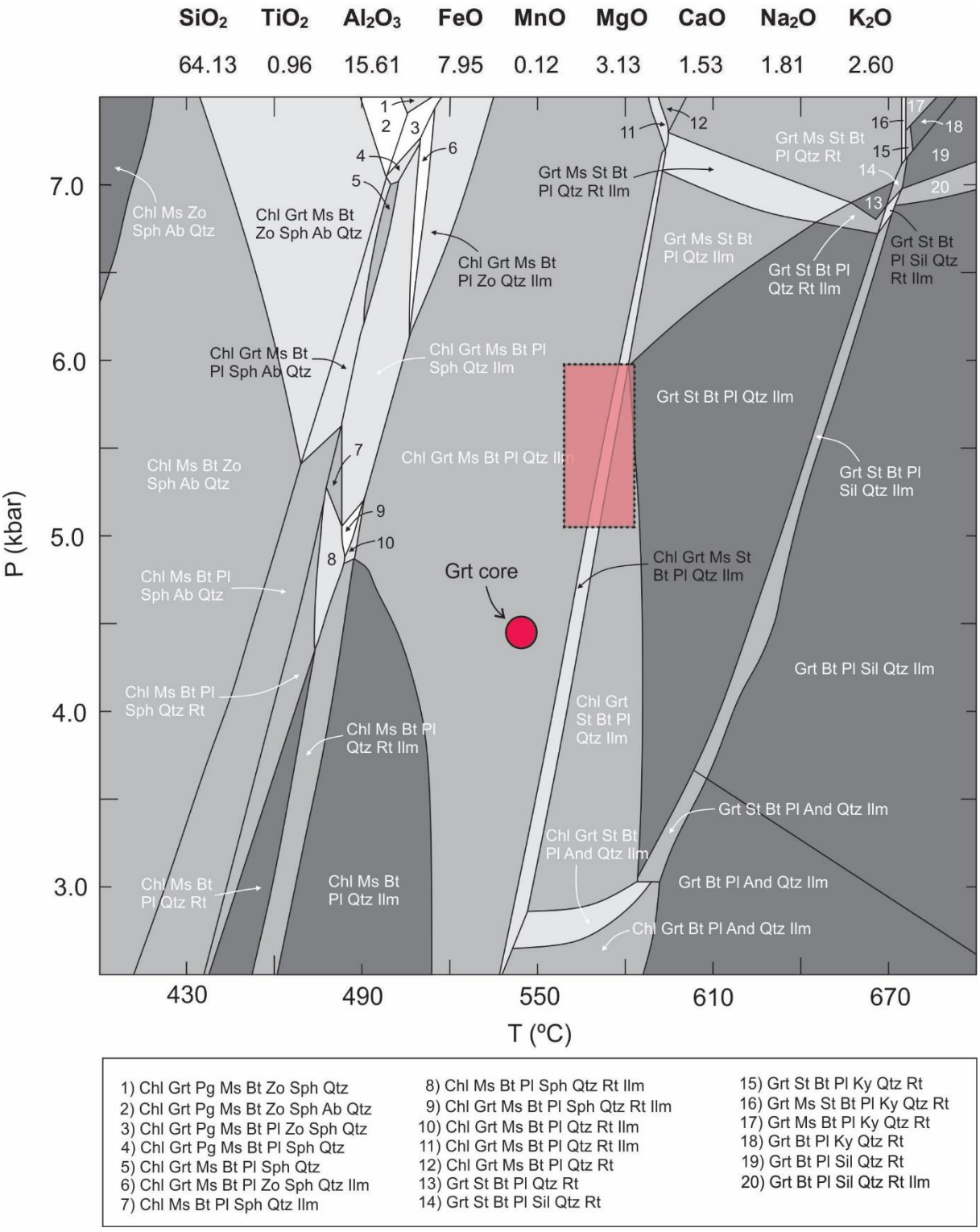

Fig. 3.21 *Calculated P-T pseudosection for the sample BD03. Bulk rock composition is indicated at the top as weight percentage of oxides. Red box – estimated P-T conditions from compositional isopleths.*

3.5.2 BD09b

Sample BD09b consists of garnet, staurolite, muscovite, biotite, quartz, plagioclase, andalusite, tourmaline and ilmenite. The system composition used for the modelling of this sample is (in wt. %): SiO_2 = 54.99, TiO_2 = 1.87, Al_2O_3 = 18.51, FeO = 13.92, MnO = 0.16, MgO = 2.17, CaO = 1.05, Na_2O = 1.44, K_2O = 2.72.

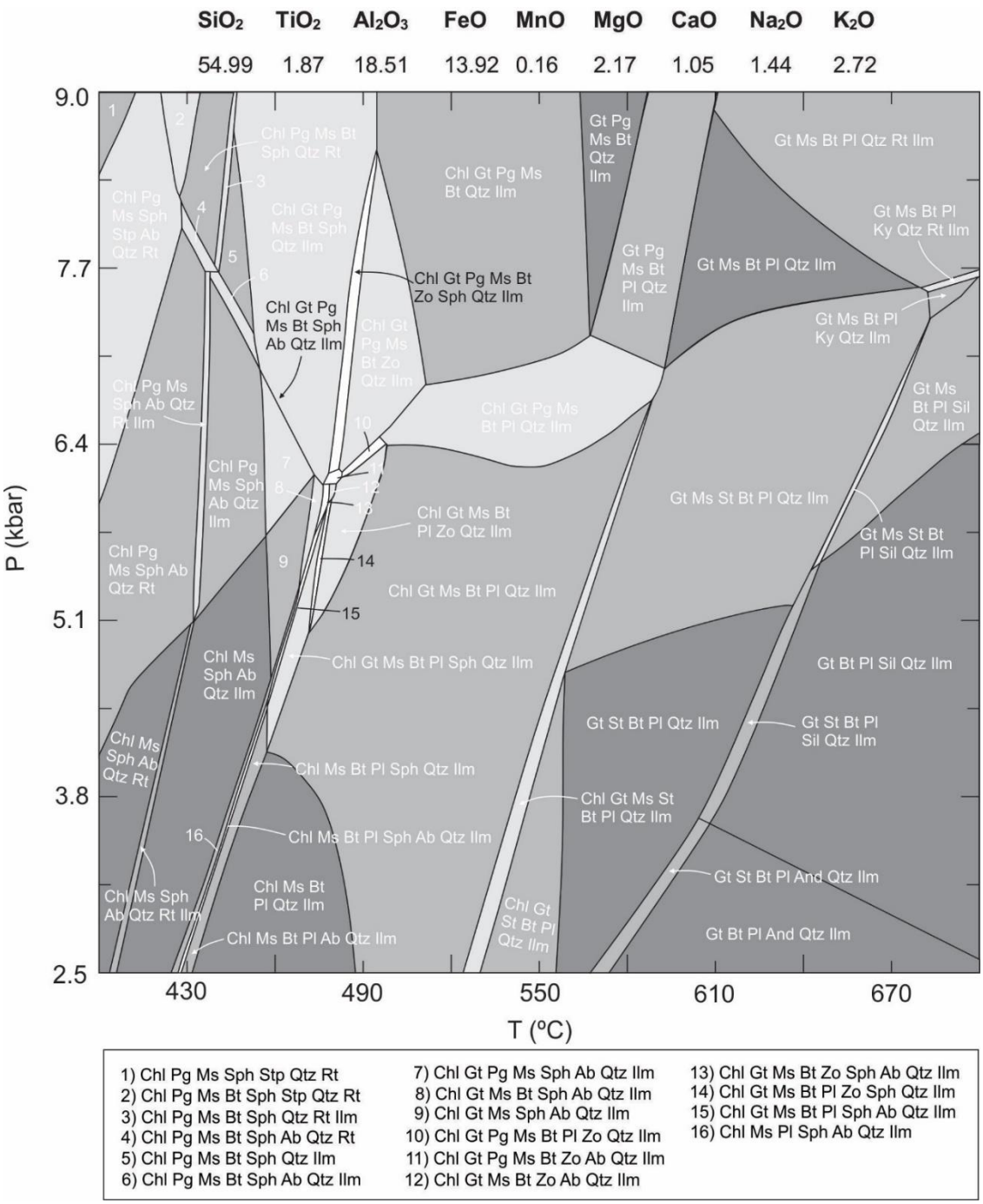

Fig. 3.22 *Calculated P-T pseudosection for the sample BD09b. The bulk rock composition is indicated at the top as weight percentage of oxides.*

The P-T pseudosection was calculated in a temperature interval of 400-700°C and a pressure interval of 2.5-9.0 kbar (Fig. 3.22). Compositional isopleths for observed minerals in sample BD09b (Fig. 3.23) were plotted in order to find the best estimate of metamorphic P-T conditions.

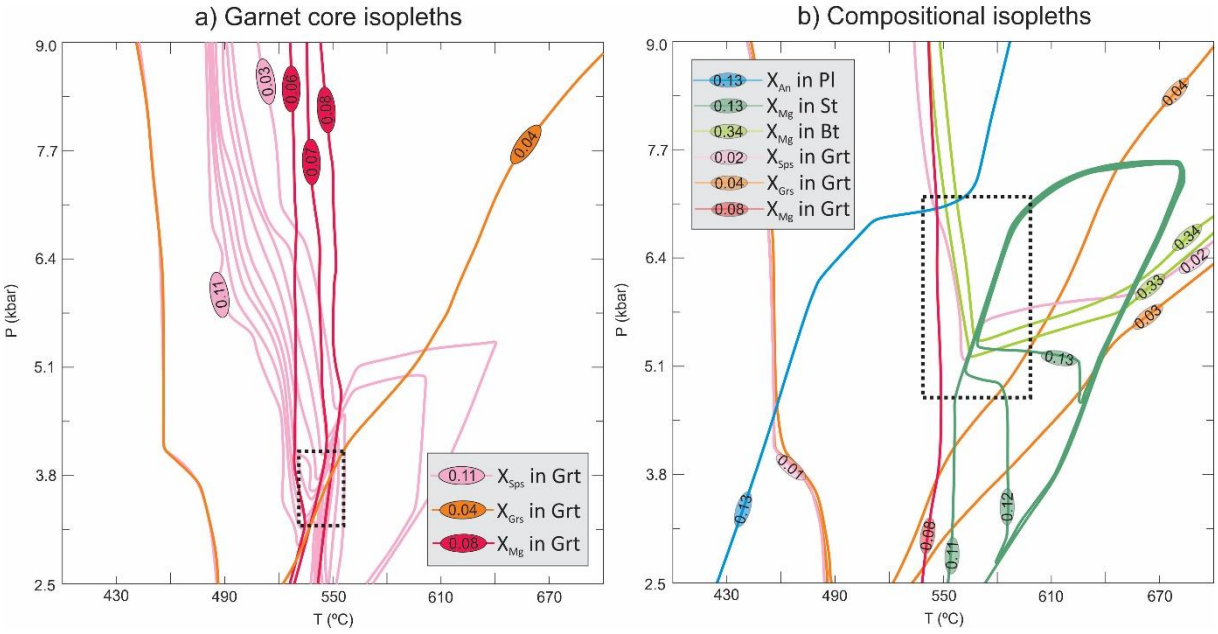

Fig. 3.23 *Compositional isopleths for the sample BD09b.* ***a)*** *Compositional isopleths for garnet cores, represented by the following: red lines – X_{Mg} values; pink lines – spessartine (X_{Sps}) endmember values; orange lines – grossular (X_{Grs}) endmember values.* ***b)*** *Compositional isopleths for garnet rims and matrix minerals, represented by: blue line – plagioclase (X_{An}); green lines – staurolite (X_{Mg}); light green lines – biotite (X_{Mg}); red lines – garnet (X_{Mg}); orange lines – grossular (X_{Grs}); pink lines – spessartine (X_{Sps}). Black dotted boxes – estimated P-T conditions.*

Data from the garnet cores (Fig. 3.23a) indicate an estimated temperature and pressure interval of approximately 530-555°C and 3.2-4.1 kbar for the beginning of garnet growth. Garnet rims together with the rest of the compositional minerals (Fig. 3.23b) indicate an estimated P-T interval of approximately 535-590°C and 4.7-7.0 kbar for crystallization.

The estimated P-T conditions from both the onset of garnet growth (Fig. 3.23a) and crystallization of the sample (Fig. 3.23b) are shown in the P-T pseudosection in Fig. 3.24. There are several stable phases within this area, but the mineral assemblage Gt-Ms-St-Bt-Pl-Qtz-Ilm corresponds well to observed optical petrography and SEM.

Andalusite is not stable within the estimated P-T conditions for the staurolite-bearing assemblage, but given its maximum pressure stability of ca. 4.0-4.5 kbar, its presence suggests low-pressure replacement of the peak mineral assemblage.

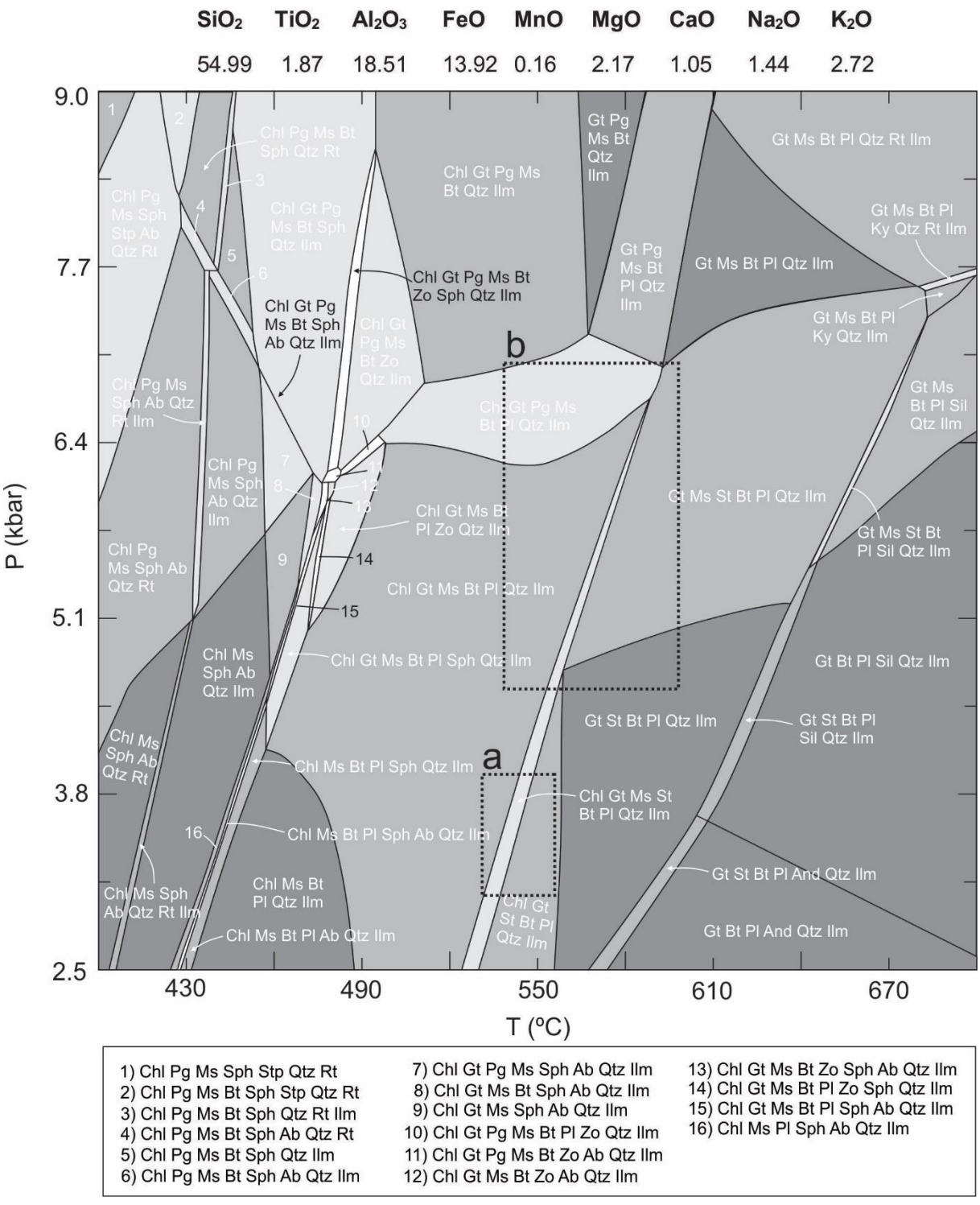

Fig. 3.24 *Calculated P-T pseudosection for the sample BD09b. The bulk rock composition is indicated at the top as weight percentage of oxides.* ***a)*** *Estimated P-T conditions from garnet core isopleths.* ***b)*** *Estimated P-T conditions from compositional isopleths of matrix minerals and garnet rims.*

3.5.3 BD14

Sample BD14 consists of garnet, staurolite, muscovite, biotite, quartz, plagioclase, chlorite and ilmenite. The system composition used for the modelling of this sample is (in wt. %): SiO_2 = 61.49, TiO_2 = 1.07, Al_2O_3 = 20.93, FeO = 6.99, MnO = 0.20, MgO = 1.33, CaO = 0.22, Na_2O = 0.97, K_2O = 3.89.

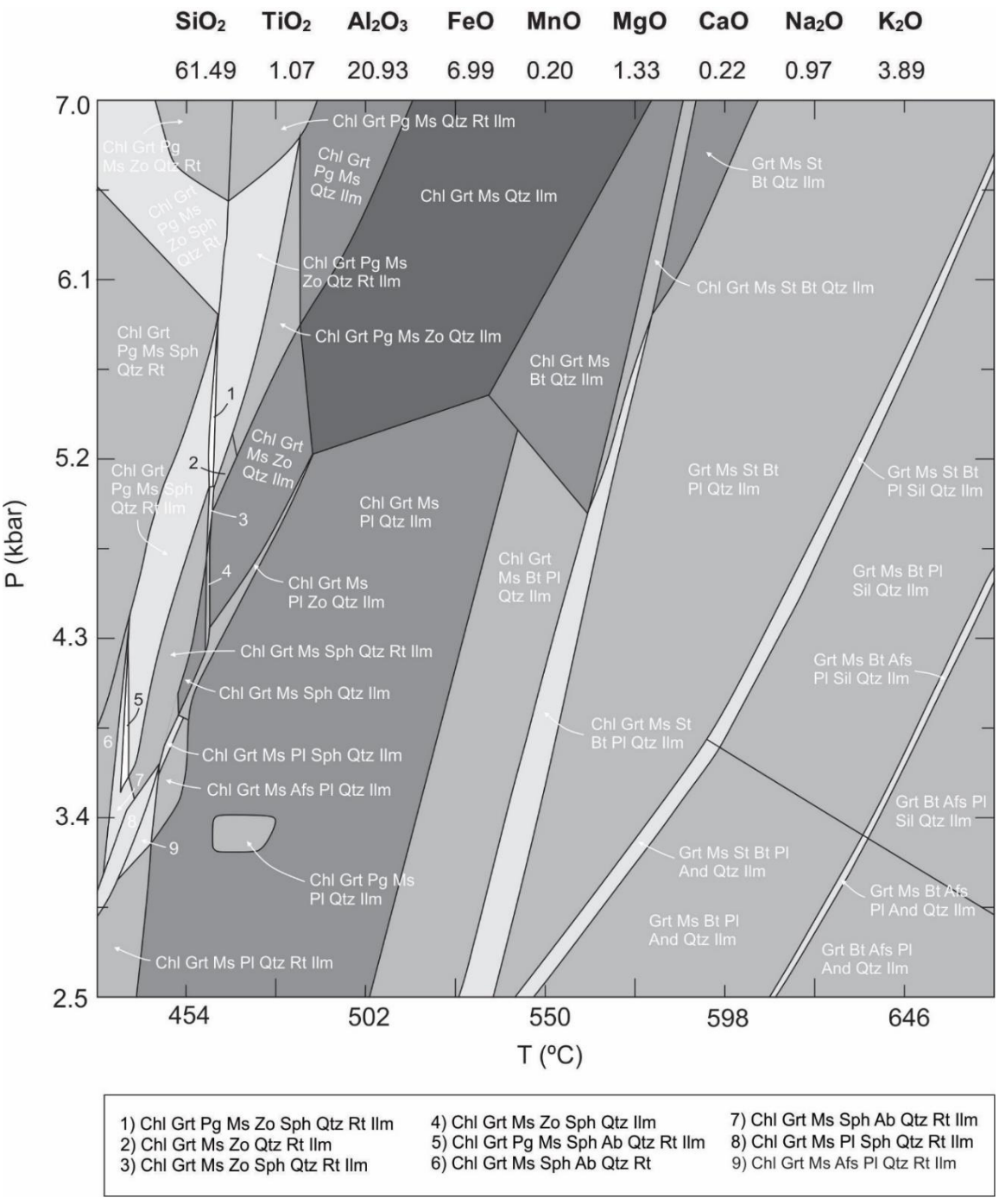

Fig. 3.25 *Calculated P-T pseudosection for the sample BD14. The bulk rock composition is indicated at the top as weight percentage of oxides.*

The P-T pseudosection was calculated in a temperature interval of 430-670°C and a pressure interval of 2.5-7.0 kbar (Fig. 3.25). Compositional isopleths calculated to find the best estimate of metamorphic P-T conditions are shown in Fig. 3.26.

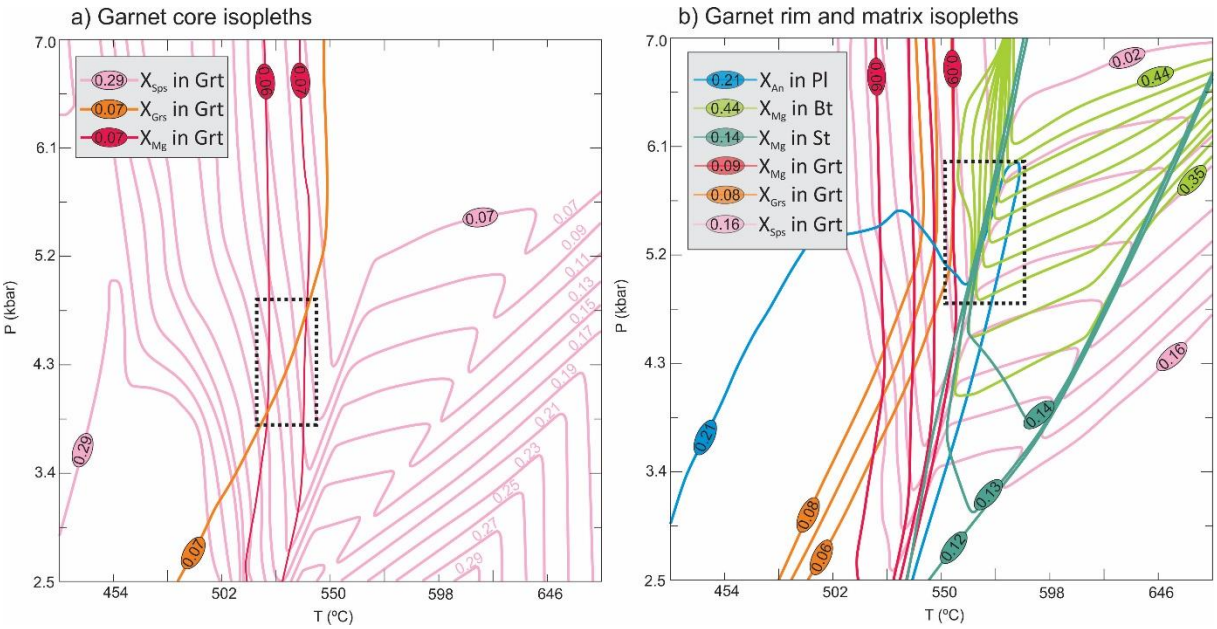

Fig. 3.26 *Compositional isopleths for the sample BD14.* ***a)*** *Compositional isopleths from garnet core data: Red – X_{Mg} values; orange – grossular (X_{Grs}); pink – spessartine (X_{Sps}).* ***b)*** *Compositional isopleths from garnet rims, shown by X_{Mg} values, grossular (X_{Grs}) and spessartine (X_{Sps}), together with compositional isopleths for the matrix minerals: blue – plagioclase (X_{An}); green – staurolite (X_{Mg}); light green – biotite (X_{Mg}).*

The garnet core isopleths (Fig. 3.26a) cross at two different places in the contour diagram, resulting in an estimated pressure and temperature of approximately 3.8-4.8 kbar and 515-540°C for the beginning of garnet growth. Isopleths for the garnet rim data and the matrix minerals (Fig. 3.26b) indicate a pressure and temperature of 4.8-5.9 kbar and 550-585°C for the matrix recrystallization. X_{Mg} and X_{Grs} values are somewhat off, compared to the X_{Sps} and matrix values. The Si content of muscovite is 3.02 a.p.f.u. within the estimated PT conditions from Fig. 3.26b, which corresponds to measured values of 3.01 to 3.06 a.p.f.u. throughout the sample.

The P-T conditions estimated from compositional isopleths are shown in the P-T pseudosection for sample BD14 in Fig. 3.27. The estimated P-T conditions for crystallization of the matrix span four different phase fields, where one of these corresponds to the mineral assemblage Chl-Grt-Ms-St-Bt-Pl-Qtz-Ilm observed during optical microscopy and SEM analysis.

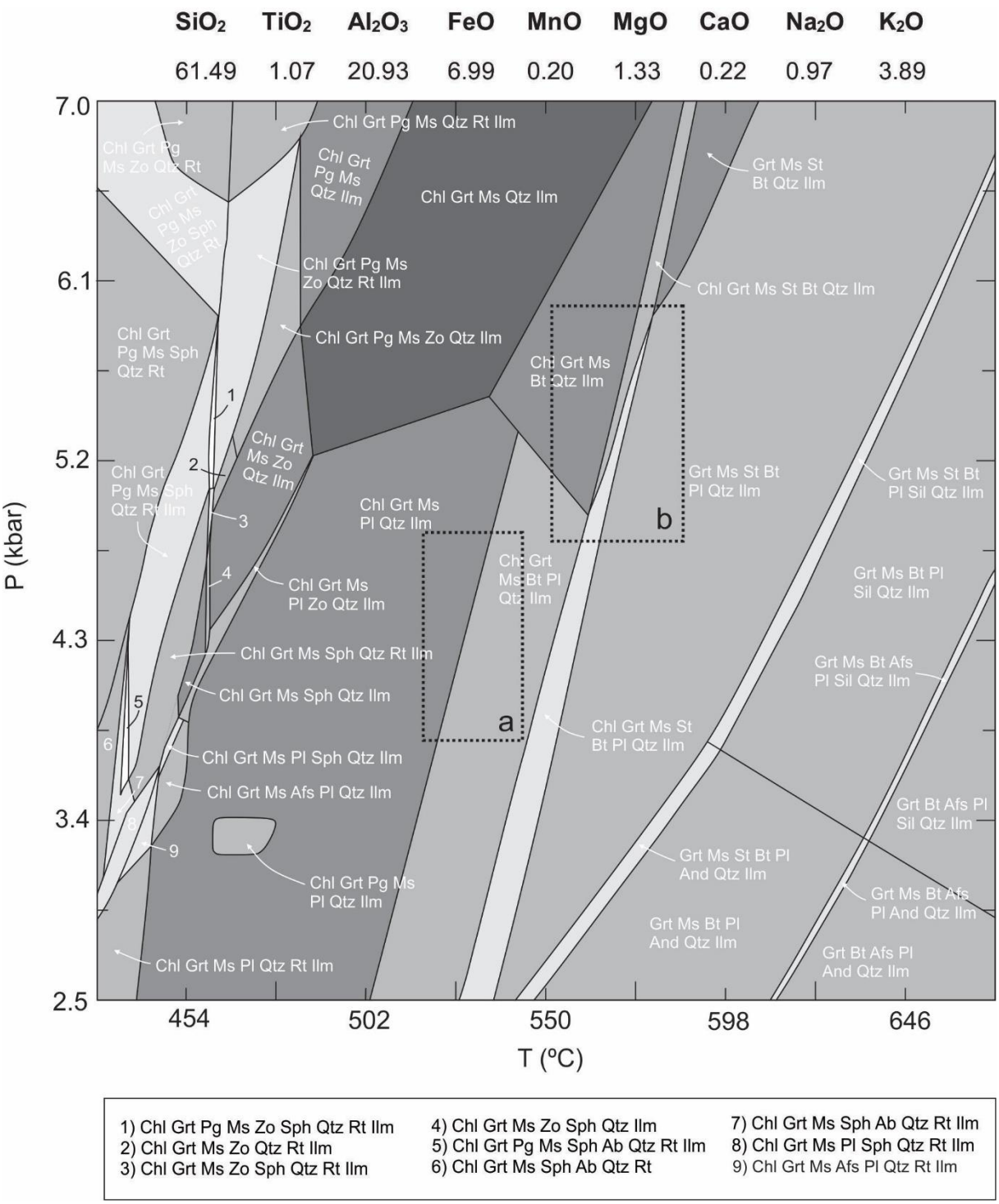

Fig. 3.27 *Calculated P-T pseudosection for the sample BD14. The bulk rock composition is indicated at the top as weight percentage of oxides.* ***a)*** *Estimated P-T conditions of garnet cores.* ***b)*** *Estimated P-T conditions of garnet rims and matrix minerals.*

3.5.4 BD15

Sample BD15 consists of garnet, staurolite, muscovite, biotite, quartz, plagioclase, chlorite and ilmenite. The system composition used for the modelling of this sample is (in wt. %): SiO_2 = 55.09, TiO_2 = 1.46, Al_2O_3 = 17.63, FeO = 13.42, MnO = 0.33, MgO = 2.82, CaO = 1.30, Na_2O = 1.43, K_2O = 2.97.

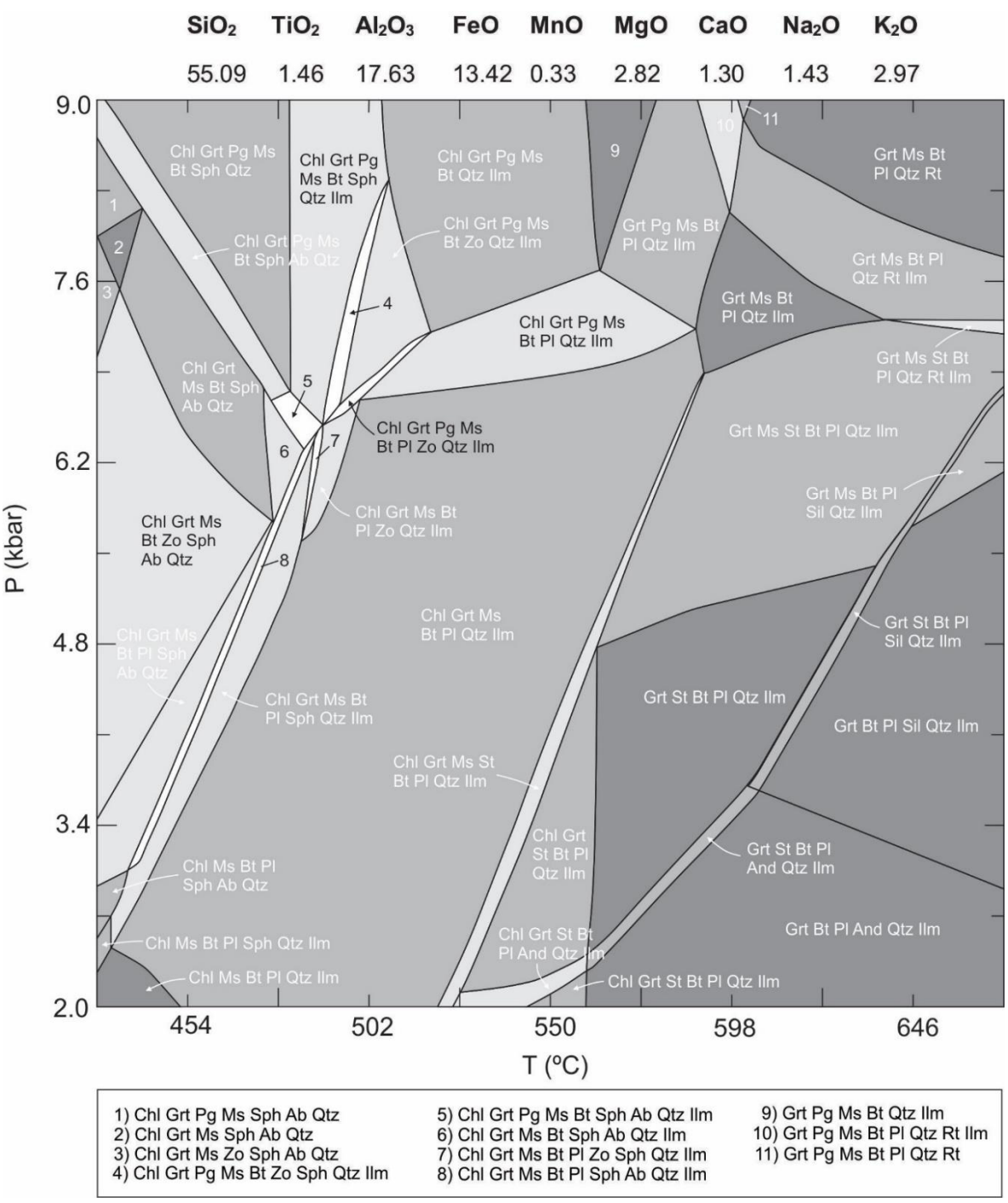

Fig. 3.28 *Calculated P-T pseudosection for the sample BD15. The bulk rock composition is indicated at the top as weight percentage of oxides.*

The P-T pseudosection was calculated in a temperature interval of 430-670°C and a pressure interval of 2.5-7.0 kbar (Fig. 3.28). Compositional isopleths calculated to find the best estimate of metamorphic P-T conditions are shown in Fig. 3.29.

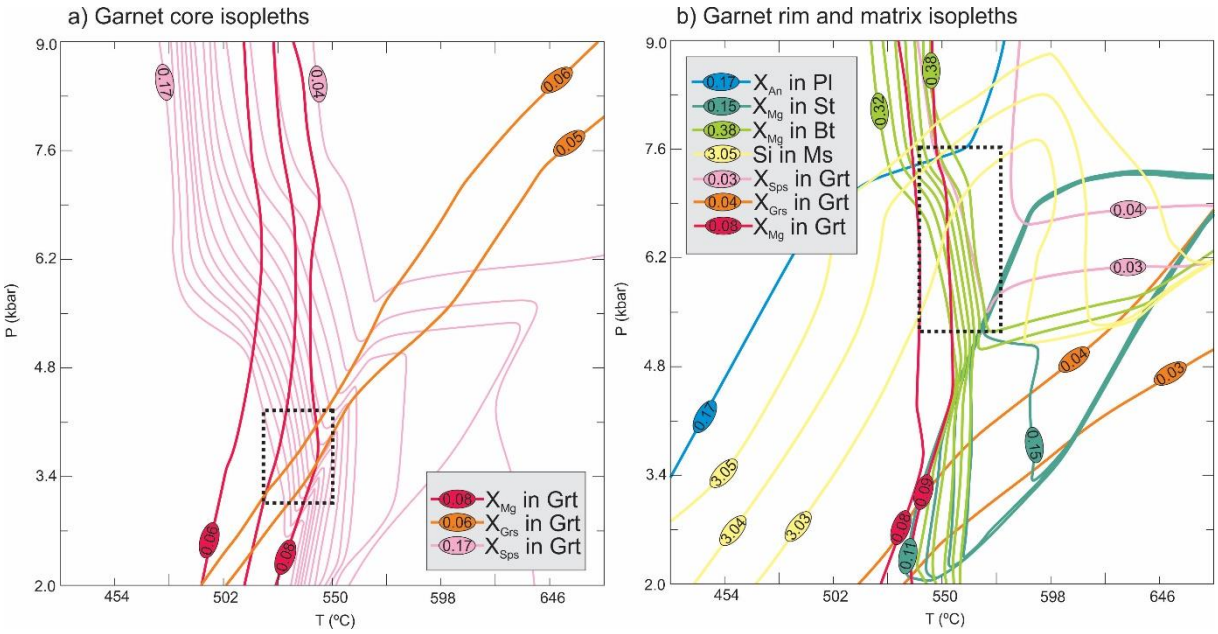

Fig. 3.29 *Compositional isopleths for the sample BD15.* ***a)*** *Compositional isopleths of garnet cores, shown by X_{Mg} values (red), X_{Grs} values (orange) and X_{Sps} values (pink).* ***b)*** *Compositional isopleths of garnet rims and matrix minerals: X_{Mg} of garnet (red), X_{Grs} in garnet (orange), X_{Sps} in garnet (pink), X_{An} in plagioclase (blue), X_{Mg} in staurolite (dark green), X_{Mg} in biotite (light green), Si content in muscovite (yellow). Black dotted boxes – estimated P-T conditions.*

The estimated P-T conditions from garnet cores show a temperature and pressure interval of approximately 520-550°C and 2.7-4.3 kbar for the beginning of garnet growth (Fig. 3.29a). In Fig. 3.29b, the temperature and pressure interval is approximately 540-575°C and 5.5-7.6 kbar. The estimated P-T conditions for crystallization in Fig. 3.29b have a wide pressure interval, which may be due to the low amount of measured plagioclase data. Both estimates of P-T conditions are presented together in the calculated P-T pseudosection in Fig. 3.30.

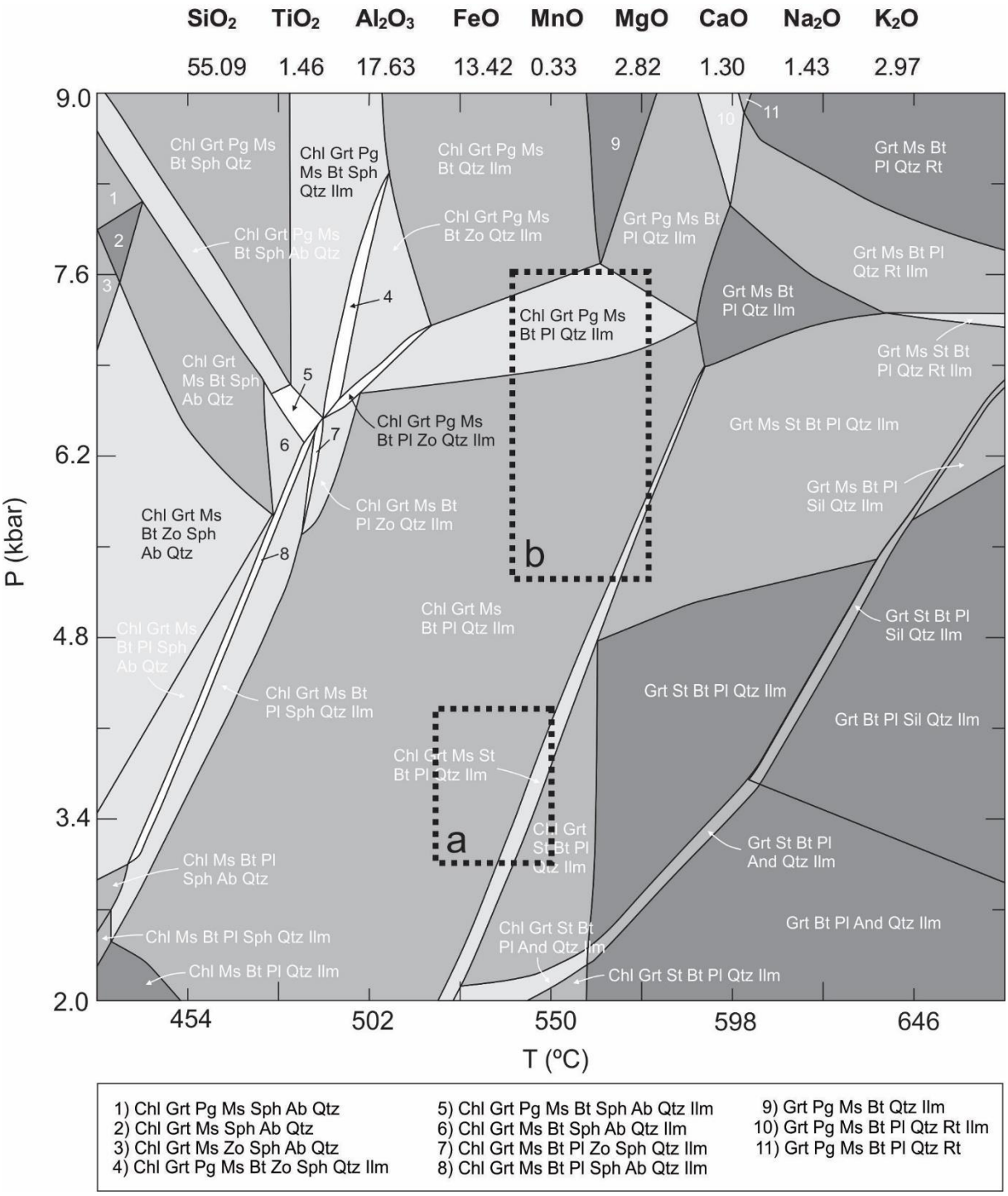

Fig. 3.30 *Calculated P-T pseudosection for the sample BD15.* ***a)*** *Estimated P-T conditions of garnet cores.* ***b)*** *Estimated P-T conditions of garnet rims and matrix minerals.*

The mineral assemblage Chl-Grt-Ms-St-Bt-Pl-Qtz-Ilm is stable within the estimated P-T windows for both the beginning of garnet growth and the matrix assemblage crystallization. This is the only phase field where the staurolite is stable, and correspond to optical petrography and SEM analysis of sample BD15.

3.5.5 BD16c

Sample BD16c consists of garnet, muscovite, biotite, quartz and ilmenite. The system composition used for the modelling of this sample is (in wt. %): SiO_2 = 61.42, TiO_2 = 0.95, Al_2O_3 = 19.75, FeO = 7.95, MnO = 0.13, MgO = 1.87, CaO = 0.03, Na_2O = 0.35, K_2O = 5.49.

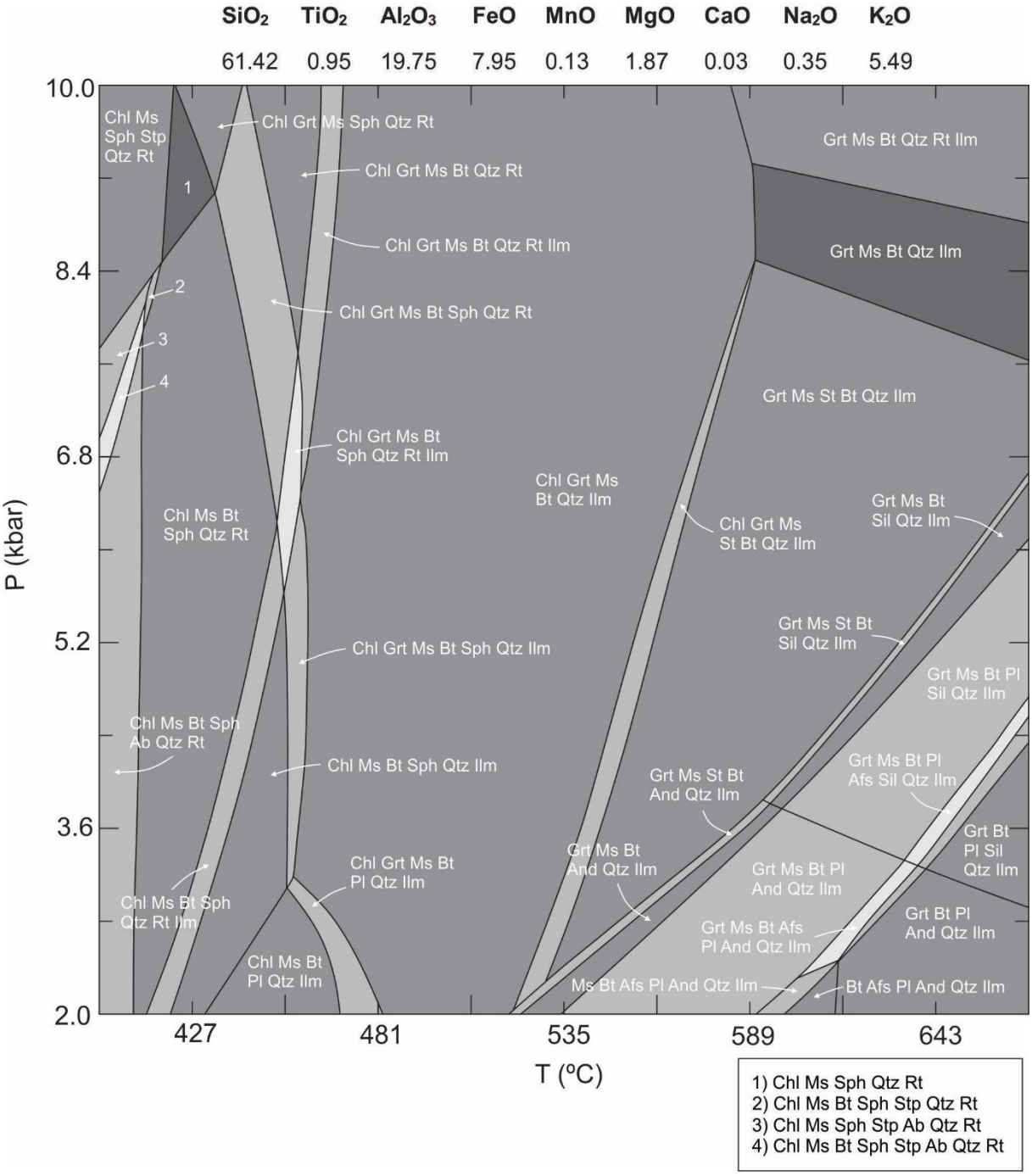

Fig. 3.31 *Calculated P-T pseudosection for the sample BD16c. The bulk rock composition is indicated at the top as weight percentage of oxides.*

The P-T pseudosection was calculated in a temperature interval of 430-670°C and a pressure interval of 2-10 kbar (Fig. 3.31). Compositional isopleths were calculated to find the best estimate of metamorphic P-T conditions (Fig. 3.32).

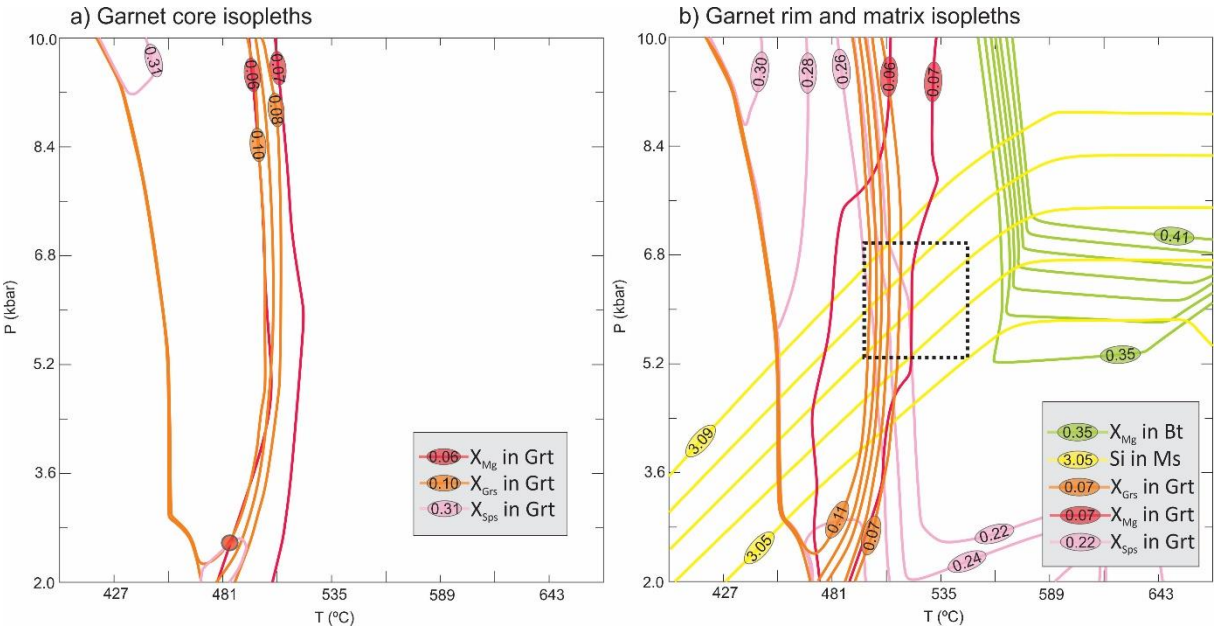

Fig. 3.32 *Compositional isopleths for the sample BD16c.* ***a)*** *Compositional isopleths of garnet cores. Red – X_{Mg} values; Orange – grossular (X_{Grs}); pink – spessartine (X_{Sps}); Red circle – estimated P-T conditions.* ***b)*** *Compositional isopleths of garnet rims, biotite and muscovite. Green – biotite (X_{Mg}); yellow – muscovite (Si-content); red – garnet (X_{Mg}); orange – grossular (X_{Grs}); pink – spessartine (X_{Sps}); Dotted box – estimated P-T conditions.*

The calculated isopleths for the garnet core composition (Fig. 3.32a) cross at approximately 485°C and 2.6 kbar, illustrated by a red circle. This is the estimated temperature and pressure for the beginning of garnet growth. Calculated compositional isopleths of garnet rims and matrix minerals (Fig. 3.32b) show a temperature interval of approximately 500-550°C and a pressure interval of approximately 5.3-7.0 kbar. The estimated P-T conditions are presented in the P-T pseudosection of sample BD16c in Fig. 3.33.

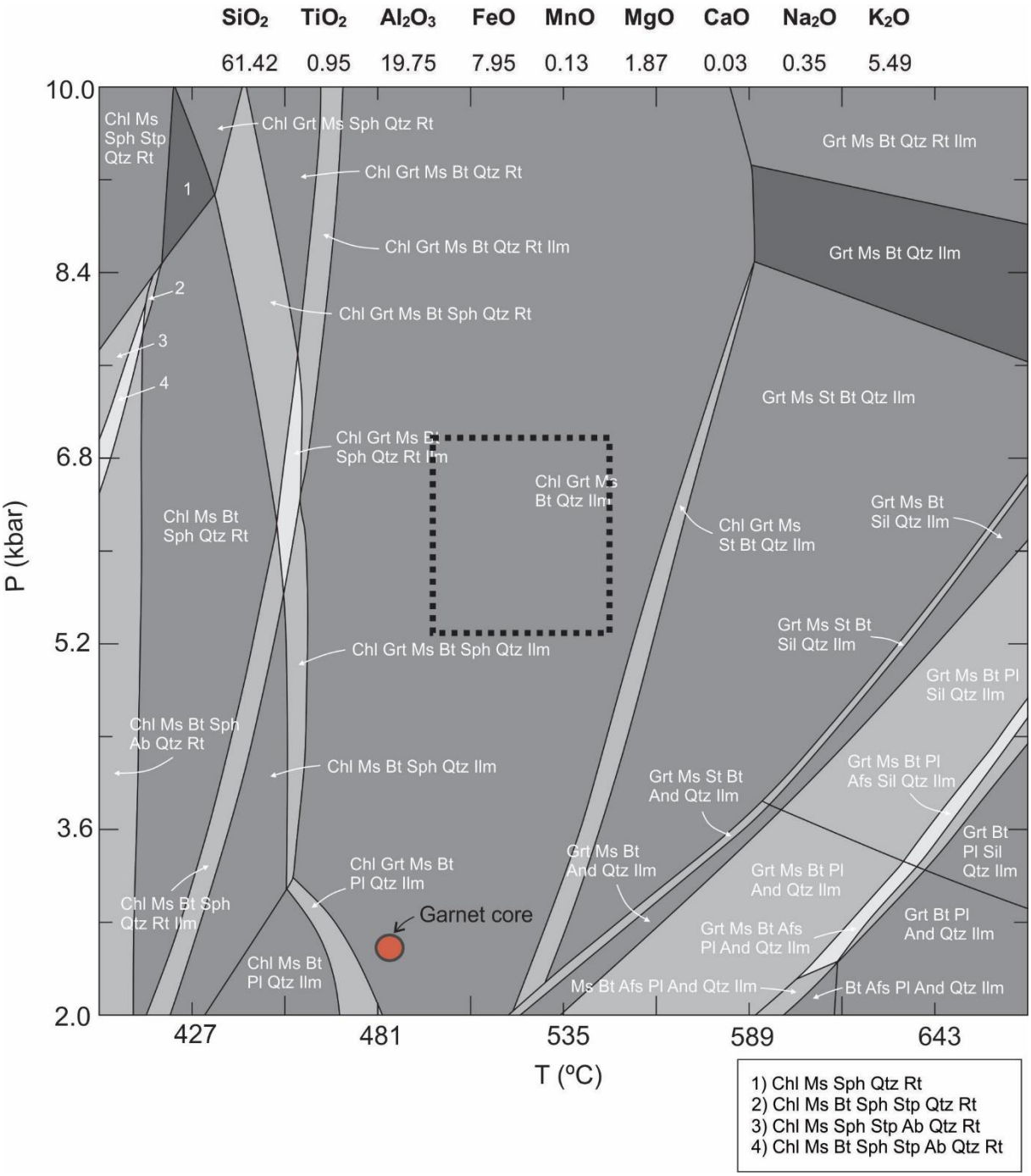

Fig. 3.33 *Calculated P-T pseudosection for the sample BD16c. The bulk rock composition is indicated in top as weight percentage of oxides. Black box – estimated P-T conditions from compositional isopleths.*

There are three phase fields stable within the area of estimated P-T conditions of crystallization (Fig. 3.33). As no staurolite is observed in the sample, the mineral assemblage Chl-Grt-Ms-Bt-Qtz-Ilm in the P-T pseudosection corresponds more or less to observations. Chlorite is not observed in optical petrography or during SEM analysis due to a very fine-grained matrix, but it is possible that the sample contains some small chlorite grains.

3.5.6 BD21

Sample BD21 consists of muscovite, biotite, quartz, hematite and ilmenite. Due to the fact that it contains both FeO (ilmenite) and Fe_2O_3 (hematite), it is very difficult to model. In addition, the SEM imaging did not provide enough data for the estimation of metamorphic conditions.

3.6 Chlorite geothermometry

In addition to the P-T pseudosections, chlorite geothermometry was applied to estimate the temperature of chlorite equilibration in the studied samples. This was done by using Excel spreadsheets prepared for the calibrations published by Vidal et al. (2001). The purpose of this publication was to derive a solid solution model and thermodynamic data for equilibration of aluminous (Si < 3 a.p.f.u.) chlorites encountered in metapelites (Vidal et al., 2001).

Among the studied samples, only three (sample BD03, BD14 and BD15) of the total six samples had reliable chlorite measurements from electron microprobe analysis. Chlorite geothermometry for these samples is presented below.

3.6.1 Results of chlorite geothermometry

Chlorite in sample BD03 crystallized at a temperature from approximately 477°C to 511°C (Fig. 3.34). These values are ca. 50-80°C lower than predicted by the pseudosection for this sample, and 30-65°C lower than the value estimated for the garnet core conditions.

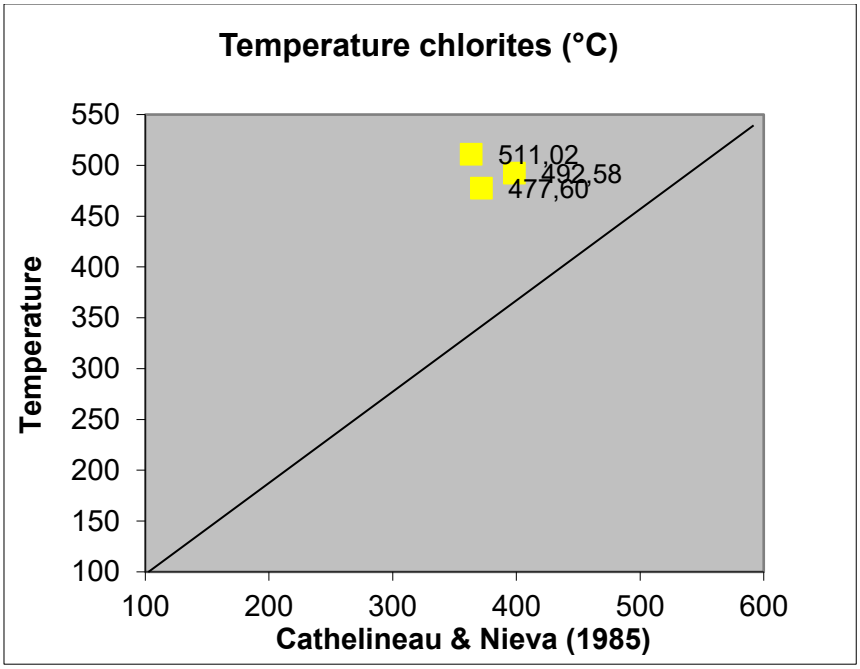

Fig. 3.34 *Chlorite geothermometry for the sample BD03.*

Two chlorite grains in sample BD14 crystallized at temperatures of approximately 306°C and 533°C (Fig. 3.35). The chlorite measured to have crystallized at ca. 533°C is around 20-50°C lower than the metamorphic peak estimated in the pseudosection, but fits together with the garnet core conditions estimated. The value of 306°C does not fit and is probably wrong, based on the comparison of the other chlorite temperatures calculated.

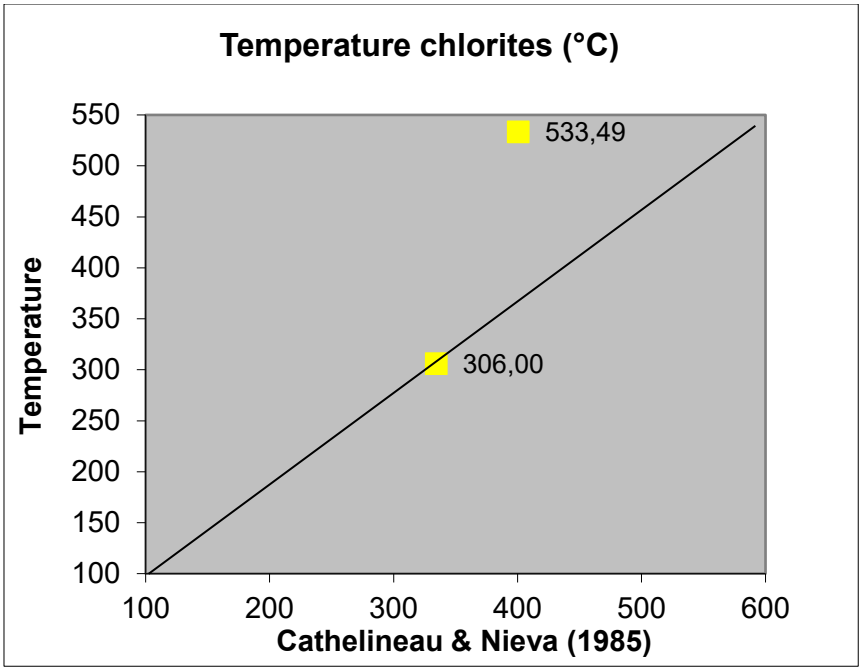

Fig. 3.35 *Chlorite geothermometry for the sample BD14.*

Chlorite in sample BD15 crystallized at a temperature of approximately 479°C (Fig. 3.36), which is ca. 60°C less than the metamorphic peak predicted by the respective pseudosection and 40°C lower than the value estimated for the beginning of garnet growth.

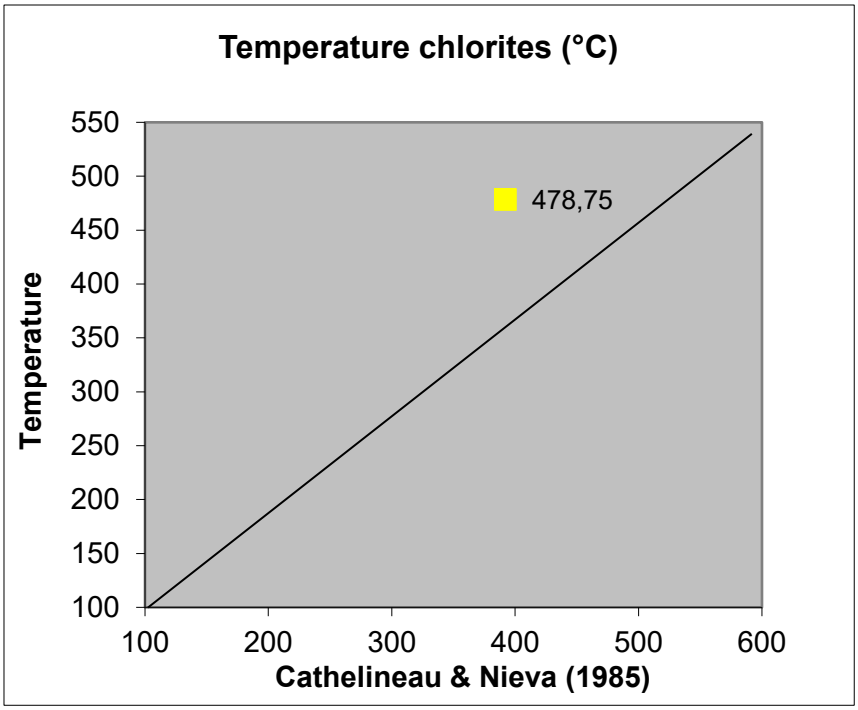

Fig. 3.36 *Chlorite geothermometry for the sample BD15.*

4 Discussion

4.1 Metamorphism related to deformational events

Structural data presented in this thesis do not provide enough information to allow for any complete and conclusive reconstruction of the deformational history of the Passo Feio Complex and the São Gabriel Block alone. However, by combining field and petrographic observations one can provide some information regarding how metamorphism relates to deformational events.

The first deformational event (D_1) involved progressive shearing of originally sedimentary rocks, and resulted in the development of S_1 foliation and in its local progressive folding producing tight to isoclinal folding (F_1). Lineation (L_1) formed parallel to the fold axes. Petrographic studies suggest that the peak metamorphic conditions in the PFC were reached during the D_1 deformational event, as garnet porphyroblasts show a syn-kinematic growth with respect to the S_1 fabric. Folded quartz veins could have been developed in a variety of ways, either parallel or perpendicular to the sedimentary layering or early S_1 foliation. In any case, the veins are assumed to be folded progressively during the S_1 fabric development (Fig. 4.1).

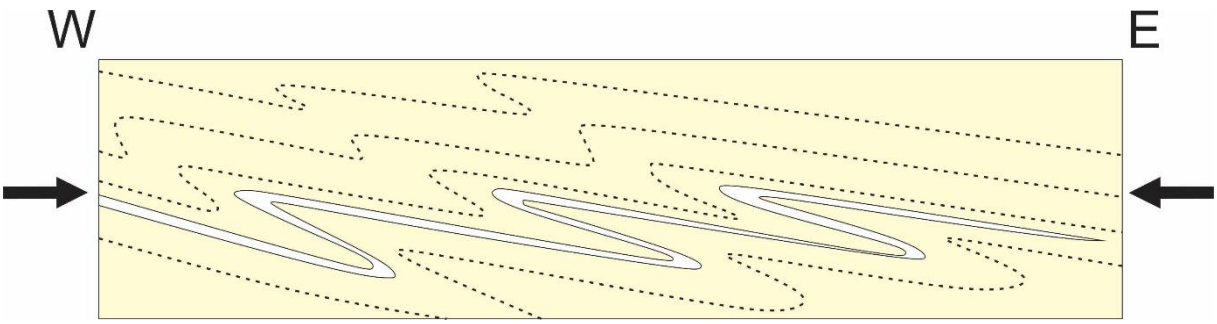

Fig. 4.1 *Illustration of the first deformational event (D_1): Progressive shearing resulting in isoclinal folding (F_1) of the S_1 foliation. The fold axes have an orientation sub-parallel with the S_1 fabric.*

Both field observations and stereographic projection of foliation orientation show that there has been a regional compression (D_2) that resulted in folding of the S_1 foliation by larger-scale open folds (F_3). The projected foliation poles in the stereonet in Fig. 3.2 show dip towards both NW and SE, consistent with NW-SE-oriented compression. Measured fold axes in Fig. 3.1 are sub-horizontal and striking in NE-SW-direction, which also is consistent with the interpreted NW-SE-direction of compression. However, a few of the projected axial planes and fold axes measured in the field have a different dip direction, which could either be interpreted as a result of a competence difference within the rocks of the PFC, or possibly as a later folding event that produced open folds. The latter is the scenario interpreted and discussed by e.g. Battisti et al. (2018) for the neighboring complexes towards the east, so there is a possibility that a third folding event also occurred in the PFC. This would indicate a D_3 event with the folding (F_3) of S_1 fabric. This however remains a matter of debate, as there is too little data and evidence of three separate folding events were not observed directly during fieldwork in the study area.

It is argued in this thesis that there are at least two deformational events that have occurred within the Passo Feio Complex, and possibly three. These deformational events can briefly be summarized as follows: 1) a regional shearing leading to the development of S_1 foliation and its progressive tight/isoclinal folding (F_1) including folding of quartz veins (D_1), 2) a new compressional event leading to open folding (F_2) of S_1 foliation. Another deformation event reorienting the S_1 foliation, after F_2 folding remains speculative, as there is not enough data to discuss in detail.

4.2 Metamorphic zones in the Passo Feio Complex

Pelitic rocks show a systematic appearance of new minerals with increasing metamorphic grade known as the Barrovian mineral succession, first described by Barrow (1893). Metapelitic rocks are often used as indicators of metamorphic conditions during orogenesis because the succession of Fe-Mg-Al minerals is largely dependent on temperature, and can be used to describe the change in metamorphic grade through an area as separate metamorphic zones with distinct index minerals within each of the zones (Bucher & Grapes, 2011). However, interpretations might be complicated because the appearance of index minerals is dependent on the bulk chemistry of the rock. Additionally, an index mineral might persist to higher grades than the zone it characterizes. For this reason, any study in metamorphic terranes should be accompanied by independent estimation of metamorphic conditions.

The observed mineral assemblages of metapelite samples collected from the southern part of the PFC can be analyzed regarding the interpretation of the change in metamorphic grade. Petrographic observation of mineral assemblages indicates that the southern part of the PFC can be subdivided into three zones in terms of metamorphic conditions (Fig. 4.2). Distinction between different zones is based on phase equilibrium modelling and observed mineral assemblages from additional samples within the area (Table 3.3).

Zone 1

Metapelitic samples collected from the southeastern part of the PFC (BD02, BD03, BD04, BD05, BD06, BD07, BD09, BD14, BD15) have mineral assemblages of St + Grt + Bt + Ms + Qtz + Pl + Ilm ± Chl. Phase equilibrium modelling suggests that these samples equilibrated at temperatures between 535-590°C, which indicates that this zone experienced middle amphibolite facies (staurolite zone) conditions during metamorphism. The presence of staurolite also suggests these conditions, as staurolite is the index mineral for amphibolite facies conditions.

Zone 2

One metapelitic sample from the southern part of the PFC (sample BD16) consists of the mineral assemblage Grt + Ms + Bt + Qtz + Ilm + Chl. Phase equilibrium modelling suggests that this sample equilibrated at a temperature between 500-550°C, which is consistent with the absence of staurolite. This zone experienced the lower amphibolite facies conditions during metamorphism. A more accurate determination of extent of this metamorphic zone is not possible due to the scarcity of samples collected in this area.

Zone 3

One metapelitic sample from the southwestern part of the PFC (sample BD21) consists of the mineral assemblage Ms + Bt + Qtz + Ilm + Hem. Observations of outcrops nearby indicate that this area is dominated by phyllites with low-grade metamorphic mineral assemblages. The absence of garnet indicate that this zone experienced greenschist facies conditions during metamorphism and did not reach as high temperatures as the two previous zones.

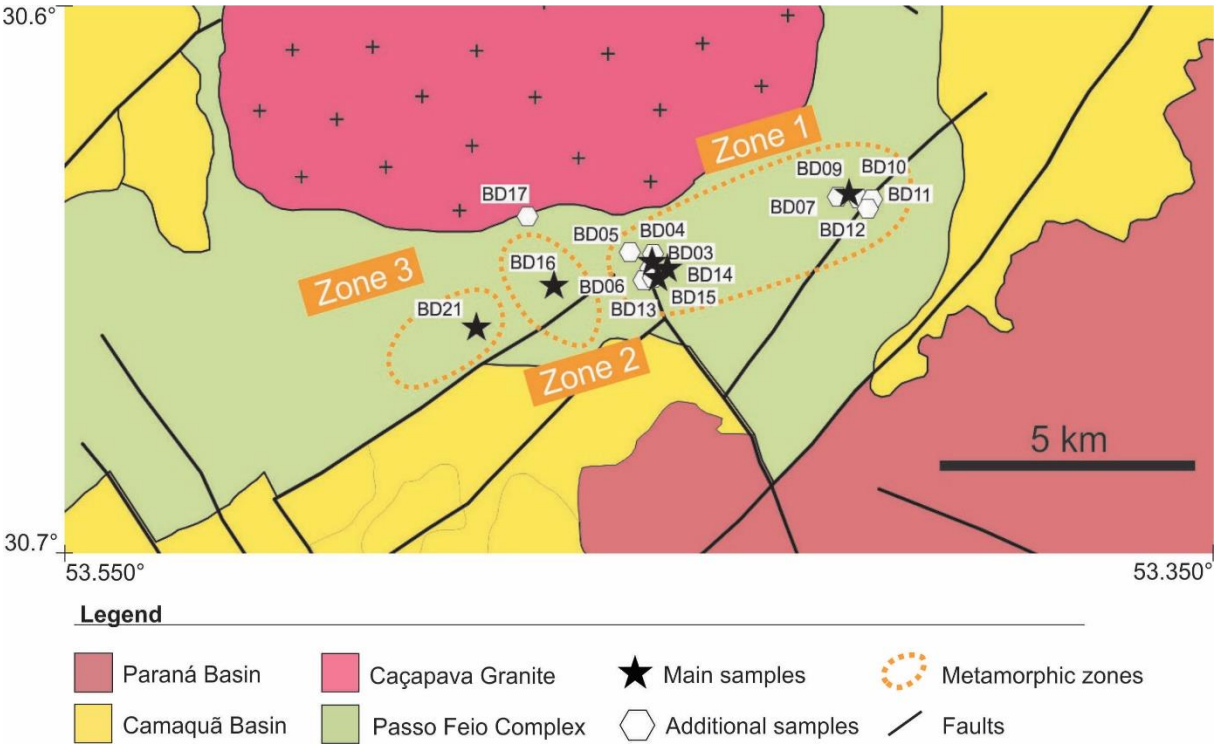

Fig. 4.2 *Illustration of the different metamorphic zones suggested for the southern PFC.*

Fig. 4.2 illustrates the three different metamorphic zones determined from observed mineral assemblages and modelling of metamorphic conditions. The metamorphic grade is highest in the eastern part of the southern PFC (zone 1), in the staurolite-garnet zone. The metamorphic grade decreases towards W/SW, through the garnet zone (zone 2) and to the westernmost chlorite zone (zone 3).

From optical petrographic observations, signs of contact metamorphism have been observed in the samples. Andalusite has grown at the expense of staurolite and is overgrowing the matrix mineral assemblage, indicating that a local thermal event occurred after peak metamorphic conditions. Andalusite is not stable within the stability field of the peak metamorphic conditions estimated for the PFC samples, as it is restricted to lower pressures. This is visible in the pseudosections in chapter 4. Contact metamorphism, commonly described as Buchan-type metamorphism, is characterized by low pressures and high temperatures which takes place during intrusions of magmatic bodies into (meta)sediments in a shallow crust (Bucher & Grapes, 2011). This thermal event (M_2) probably took place at the time of the Caçapava Granite intrusion around 560 Ma (Remus et al., 2000), as a local metamorphism occurring only close to the intrusion.

4.3 Age of metamorphism

Based on the mineral composition of the metapelite samples, it was assumed that it could be possible to separate monazites and to date them. This turned out to be more difficult than expected, and did not work out as first imagined. Staurolite grains were difficult to separate magnetically from the presumed monazites, due to their very similar magnetic properties. For this reason, this work does not provide any age data for the metamorphism of metapelites of the Passo Feio Complex.

The only age constraint that is associated with this study suggests that metamorphism must have happened before ca. 560 Ma, which is the age of the intrusion of the Caçapava Granite. This interpretation can be made, because there is evidence of contact metamorphism. It is clear from microscopic observations that the contact minerals overgrow the medium-pressure mineral assemblage of the staurolite-bearing samples. The contact minerals are younger than

the main mineral assemblage, which is a strong indication that regional metamorphism and stabilization of St-bearing mineral assemblages must have occurred before the granite intrusion.

4.4 P-T estimates and geothermal gradient

The largest uncertainty in the use of the Perple_X software comes from the thermodynamic mixing models, which may not entirely represent the mixing behavior of natural minerals. Therefore, the thermodynamic modelling is regarded as a good method for estimation of metamorphic conditions, but it has some limitations. These limitations are visible during work with compositional isopleths for the minerals present in the studied samples, as some of the isopleths do not perfectly match with the position of other isopleths in the model P-T diagram. Consequently, there are some relatively large uncertainties in the estimated P-T conditions for some of the samples.

Other uncertainties, besides the thermodynamic mixing models and their accuracy, is the amount of available data from electron microprobe analysis. During this process, some minerals were too fine-grained to get a range of measurements, which resulted in a pseudosection with low to no compositional isopleths to work with. This is unfortunately the outcome for the sample BD21.

Chlorite geothermometry was performed to compare the results with estimates from the Perple_X software. This method provided temperature values for the matrix equilibration that do not fit with those calculated in the P-T pseudosections. However, SEM analysis revealed a chloritization of biotite in various samples, so there is a possibility that the chlorite is retrograde and that the temperatures estimated by the chlorite thermometry says something about the retrogression rather than about peak metamorphic conditions. Nevertheless, the estimates of metamorphic conditions through thermodynamic modelling are based on the composition of several minerals stable in a metamorphic assemblage, and for this reason it provides more plausible and accurate results than chlorite geothermometry alone.

The resulting estimates of P-T conditions from calculated pseudosections and compositional isopleths provide valuable information regarding the interpretation of the depth in which the metapelitic samples equilibrated.

P-T estimates of the St-bearing samples (BD03, BD09b, BD14 and BD15) suggest that the matrix mineral assemblage equilibrated at temperatures of ca. 535-590°C and pressures of ca. 4.7-7.6 kbar. These pressure conditions correspond to depths of ca. 17-28 km assuming an average crust density of 2.8 g/cm^3. This suggest an apparent thermal gradient of 19-35°C/km for these samples. The mineral assemblage in the Grt-bearing sample BD016c is estimated to have equilibrated at a temperature of ca. 500-550°C and a pressure between ca. 5.3-7.0 kbar. These pressure conditions correspond to depths of ca. 19-26 km and an apparent thermal gradient of 20-29°C/km. The estimated apparent thermal gradient during deformation ranges between 19-35°C/km (Fig. 4.3). It is interpreted that the rocks were thrust down to an approximate maximum depth of 28 km within the crust during the metamorphism of the complex.

P-T estimates of garnet cores in all of the studied samples suggest that the beginning of garnet growth occurred at temperatures of ca. 485-555°C and pressures of ca. 2.6-4.8 kbar. These pressure conditions correspond to depths of ca. 9.5-17.5 km, and suggest an apparent thermal gradient of 35-55°C/km. The garnet cores suggest higher apparent thermal gradients than that suggested for the garnet rims and matrix minerals, and thus the whole evolution of garnet from core to rim suggests a lowering of the regional gradient during crustal thickening.

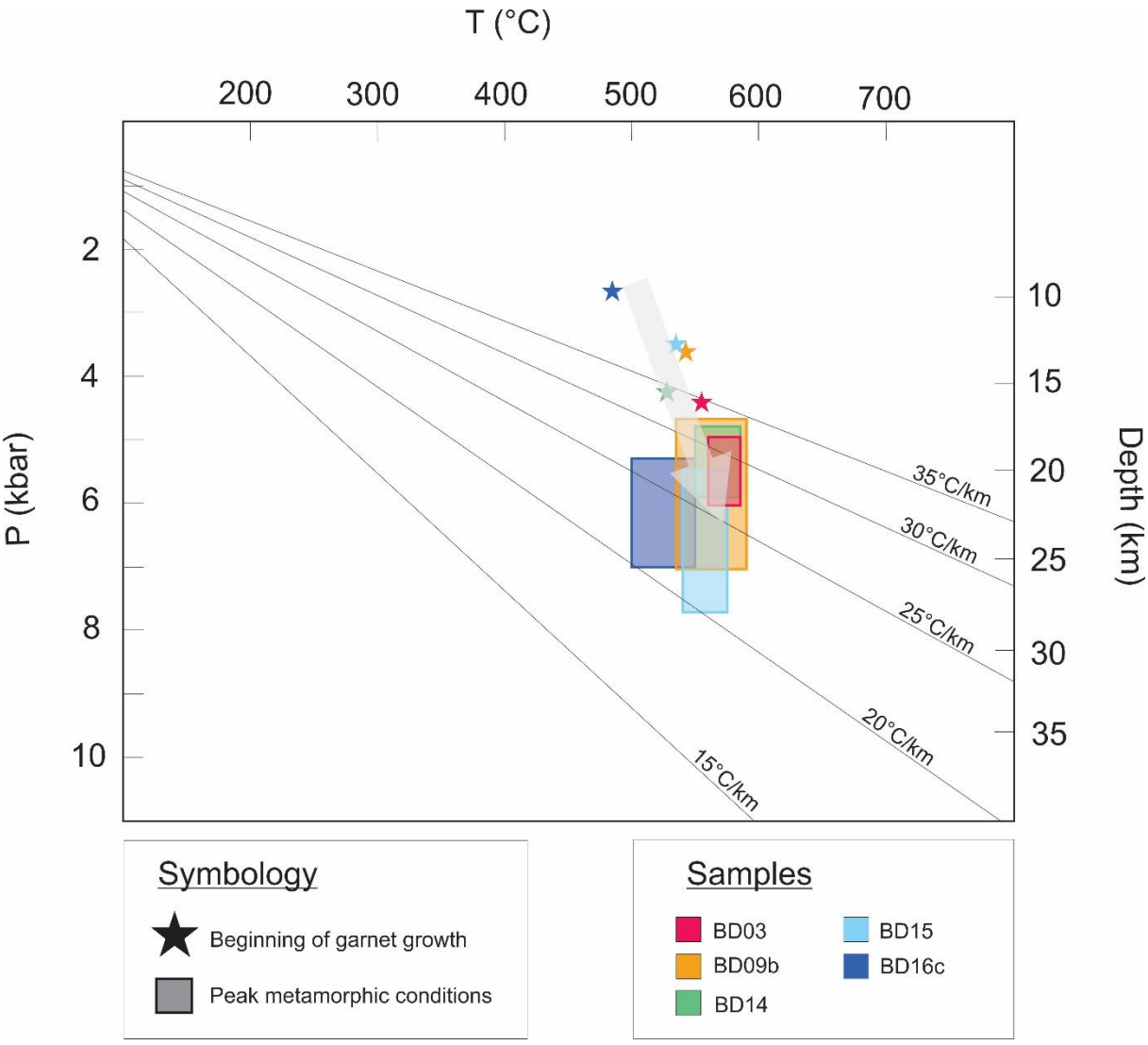

Fig. 4.3 *Summary of P-T conditions for samples from the Passo Feio Complex. Geothermal gradients are presented together with the respective peak metamorphic conditions and estimated P-T conditions for the beginning of garnet growth in each of the samples. The grey arrow indicates the P-T path of garnet growth.*

4.4.1 Comparison with other metasedimentary complexes of the Dom Feliciano Belt

The metamorphic conditions during the deformation of the Passo Feio Complex (PFC) can be compared to those of the neighboring Porongos Metamorphic Complex (PMC) and the Brusque Metamorphic Complex (BMC) in the state of Santa Catarina. Both of these other complexes are a part of the Schist Belt, i.e. metamorphosed sedimentary rocks of the Dom Feliciano Belt foreland, and the peak metamorphic conditions of metapelites within the complexes will be discussed here in relation to the PFC.

The PMC has often been correlated with the BMC and their respective basements, as they both are part of the Schist Belt of the Dom Feliciano Belt and contain Neoproterozoic metapelites and felsic volcanic rocks (Hartmann et al. 2000). Basei et al. (2011) suggested greenschist facies metamorphic conditions of the metapelites in the BMC, with a maximum temperature of 570°C and pressure of 4.0 kbar. Recent estimates by Percival (in prep.), on the other hand, suggest temperatures of 540-555°C and pressures of 6.5-7.0 kbar during the metamorphic peak of the northern part of the BMC. Ongoing research by De Toni et al. (in prep.) has estimated metamorphic conditions of staurolite-garnet schists in the PMC at ca. 560-580°C and 5.8-6.3 kbar. The inferred geothermal gradient during deformation is estimated at ca. 30°C/km (De Toni et al., in prep.). The peak metamorphic conditions from both the PMC and the BMC are compared with the estimates of metamorphic conditions for the PFC in Fig. 4.4.

The P-T estimates from the PMC and the BMC correspond to the estimated peak metamorphic conditions in the PFC (Fig. 4.4). Based on these estimates, metapelites of the PMC equilibrated at depths of 21-23 km during deformation, and metapelites of the BMC equilibrated 23.7-25.5 km. These depths correspond to the depths at which samples from the PFC reached their peak metamorphic conditions, approximately somewhere between 19-28 km. The geothermal gradient is another similarity between the three complexes, as the metapelites in each of them have been calculated to have a gradient of 24-28°C/km (PMC), 21-23°C/km (BMC) and 18-35°C/km (PFC). These results suggest an overall similarity of metamorphic temperatures and maximum depths reached in different parts of the Dom Feliciano foreland during Neoproterozoic crustal thickening.

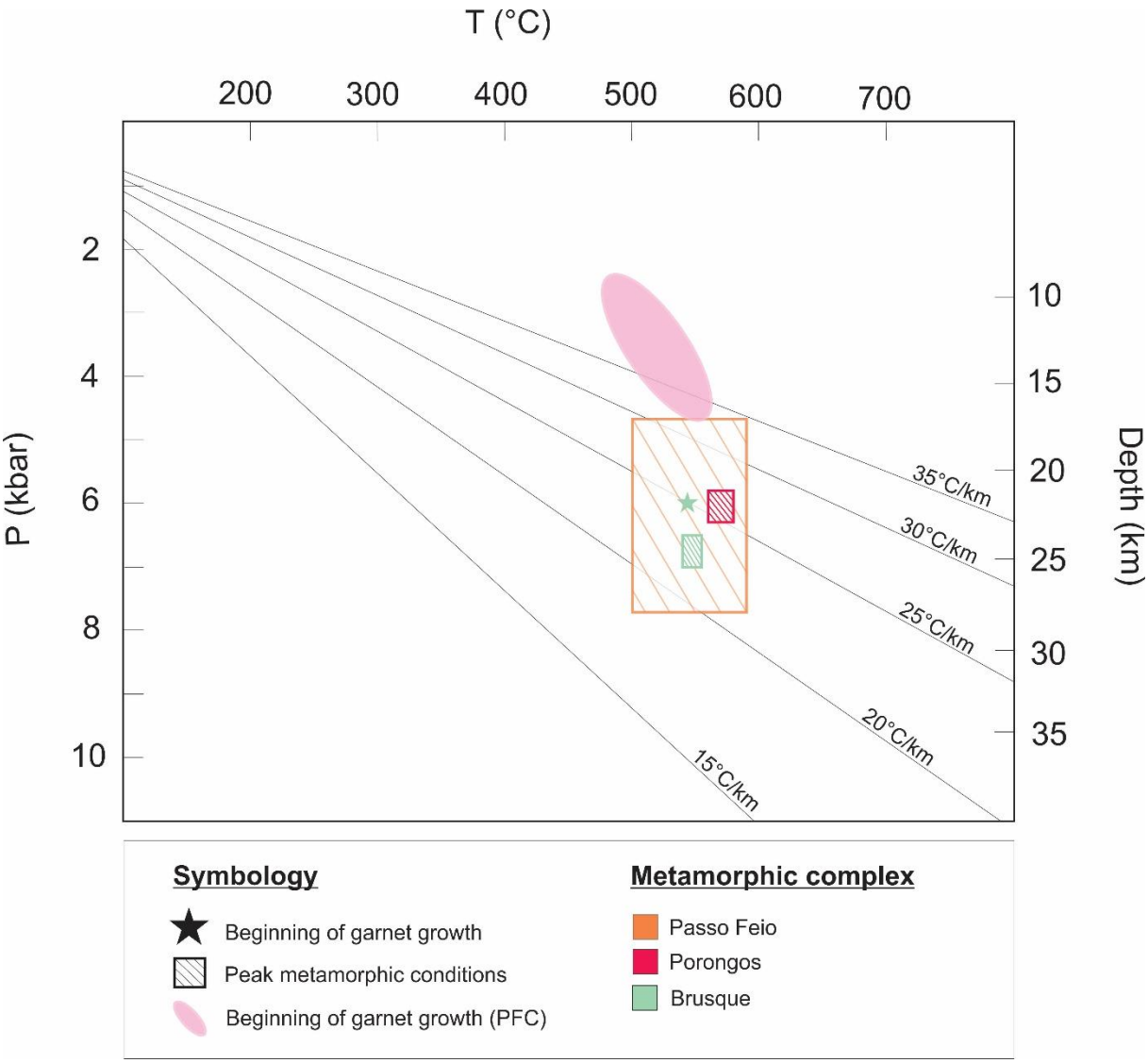

Fig. 4.4 *Estimates of peak metamorphic conditions in the Passo Feio Complex (PFC), Porongos Metamorphic Complex (PMC) and Brusque Metamorphic Complex (BMC).*

Recently, Battisti et al. (2018) correlated the PMC and the Várzea do Capivarita Complex (VCC) and suggested that the two complexes could have originated in the same volcano-sedimentary environment. The VCC comprises high-grade metamorphic rocks unlike the PMC and its metapelitic sequence of low to medium metamorphic grade, but protoliths of metasedimentary and metaigneous rocks of both complexes yielded ages of ca. 790 Ma (Battisti et al., 2018; Martil et al., 2017). The similar age and the difference in metamorphic grade is interpreted as the result of the two complexes being metamorphosed at different depths of the same depositional basin, later intruded by granitic magmas (Battisti et al., 2018).

The PFC, similar to both the BMC and the PMC, consists of low to medium grade metamorphic sequences of metavolcano-sedimentary rocks. Remus et al. (2000) indicated an opening of the Passo Feio Basin around 760-780 Ma and subsequent closure at ca. 700 Ma during compressional deformation and regional metamorphism. Due to the similarity in metamorphic grade estimated from metapelitic rocks in the PFC and the PMC, and the arguments from Battisti et al. (2018) regarding deposition of the PMC and the VCC, one should not exclude the possibility of the PFC being a part of this depositional basin as well, specifically its westernmost extension. This is considered in the next section regarding the tectonic history of the PFC in relation to PMC and VCC.

4.5 Tectonic evolution of the Dom Feliciano Belt in the state of Rio Grande do Sul

Results presented in this thesis can be combined with previously published works in a schematic model that summarizes a suggested pre-, syn- and post-collisional evolution of the Dom Feliciano Belt in the state of Rio Grande do Sul.

Pre-collisional setting

Interpretation of the early tectonic evolution, especially prior to the main collision, differs substantially among various authors. There is a common consensus that the supercontinent Rodinia began its break-up by subduction/accretion activity along the continental margins around 900-850 Ma, and that evidence of subduction is present in the juvenile São Gabriel Terrane. However, the placement of the different cratons and microcontinents, as well as the rifting event itself has been a matter of debate.

Basei et al. (2000) proposed a scenario where a continental rift system developed during Early Neoproterozoic (ca. 820 Ma) and preceeded into the development of an oceanic domain ("Adamastor Ocean") that was later subducted during Neoproterozoic convergence. Konopásek et al. (2018) later argued that the continental rift system ("Adamastor Rift") did not evolve into an oceanic domain, and explained it as a peripheral orogeny with a long-lasting subduction system along the periphery of the continental domain with extension in its interior. The proposed scenario involved the assembly of the Congo and Kalahari cratons rimmed by the Nico Pérez-Luís Alves Terrane, with an open oceanic domain west of these old landmasses and ongoing subduction activity towards the east (Konopásek et al., 2018).

The pre-collisional setting and early evolution of the São Gabriel Terrane is presented in a proposed tectonic model in Fig. 4.5a. A long-lasting subduction system along the western edge of the Congo and Kalahari cratons, rimmed by the Nico Pérez-Luís Alves Terrane, resulted in two separate episodes of magmatic arc construction (Konopásek et al., 2018; Philipp et al., 2016; Philipp et al., 2018; Saalmann et al., 2011). The first episode is the formation of an intra-

oceanic island arc (Passinho Arc) dated at ca. 880 Ma. Eastward subduction is presumed to have occurred closer to the Nico Pérez-Luís Alves Terrane and created a continental margin arc (São Gabriel Arc) between ca. 780 and 720 Ma. A simultaneous back-arc extension led to the development of a back-arc rift basin with thinned continental crust (Fig. 4.5b). The back-arc extension is assumed to be related to the formation of the Adamastor Rift, whose occurrence is argued and described by Konopásek et al. (2018). Erosion of the surrounding Nico Pérez-Luís Alves Terrane and the São Gabriel Arc filled the basin with volcano-sedimentary material, which is nowadays represented by the metavolcano-sedimentary sequences of the Passo Feio, Porongos and Várzea do Capivarita complexes.

700-650 Ma collision of the orogenic system

Subduction activity west of the Nico Pérez-Luís Alves Terrane could have eventually caused an accretion of the Passinho Arc to the São Gabriel Arc approximately around 700 Ma, which is consistent with the first metamorphic event suggested for the Passo Feio Complex (Remus et al., 2000) and metamorphism in the Porongos Metamorphic Complex (Salsmann et al., 2006). This is illustrated in Fig. 4.5c. A change from extensional to compressional tectonics in the Late Neoproterozoic (Basei et al., 2018; Konopásek et al., 2018) caused the rifting in the back-arc region between the Nico Pérez Terrane and the Congo and Kalahari cratons to cease, and the convergence led to thrusting, isoclinal folding and shearing in the sediments deposited in the back-arc basin. The VCC, originally assumed to have been deposited in the deeper part of the rift basin, was thrust westwards and over the PMC. The westward thrusting also led to folding in the PFC, as Fig. 4.5c indicates.

The two magmatic arcs, Passinho and São Gabriel, are from this point on considered as the São Gabriel Terrane (Fig. 4.5c-e).

Late- and post-collisional setting

After the change of tectonic forces from extensional to compressional, it is assumed to have been a relatively short tectonic relaxation stage (Fig. 4.5d) in the orogenic system (Battisti et al., 2018). Erosion of the São Gabriel Terrane and the complexes originating within the previously back-arc basin resulted in the deposition of several successions of flysch/molasse

sediments (Camaquã Basin) between approximately 620-580 Ma (Basei et al., 2000; de Oliveira et al., 2014). An emplacement of late-tectonic granites occurred throughout the São Gabriel Terrane and the metavolcano-sedimentary complexes, together with syenites at the boundary between the Porongos and Várzea do Capivarita complexes (Battisti et al., 2018). The Caçapava Granite is a part of the post-collisional granitic magmatism, with an intrusion age of ca. 560 Ma (Remus et al., 2000). The batholiths of the Dom Feliciano Belt is also a part of the post-collisional granitic magmatism, and the Pelotas Batholith was constructed during more or less continuous magmatic activity between ca. 650-550 Ma (Basei et al., 2018; Hueck et al., 2018).

A reactivation of contractional structures around ca. 580 Ma generated open folds and/or thrust piles in the Porongos and Várzea do Capivarita complexes, and possibly also in the Passo Feio Complex (Fig. 4.5e). Successions of the Camaquã Basin were deformed and weakly metamorphosed during this time (Basei et al., 2000; de Oliveira et al., 2014). The Río de la Plata Craton could have been accreted to the São Gabriel Terrane around this time, despite suggestions of an earlier timing of such event (Höfig et al., 2018; Saalmann et al., 2006; Saalmann et al., 2011).

After the last contractional stage, the Brasiliano Cycle ended with the assembly of Gondwana in Ediacaran-Cambrian times, around ca. 500 Ma.

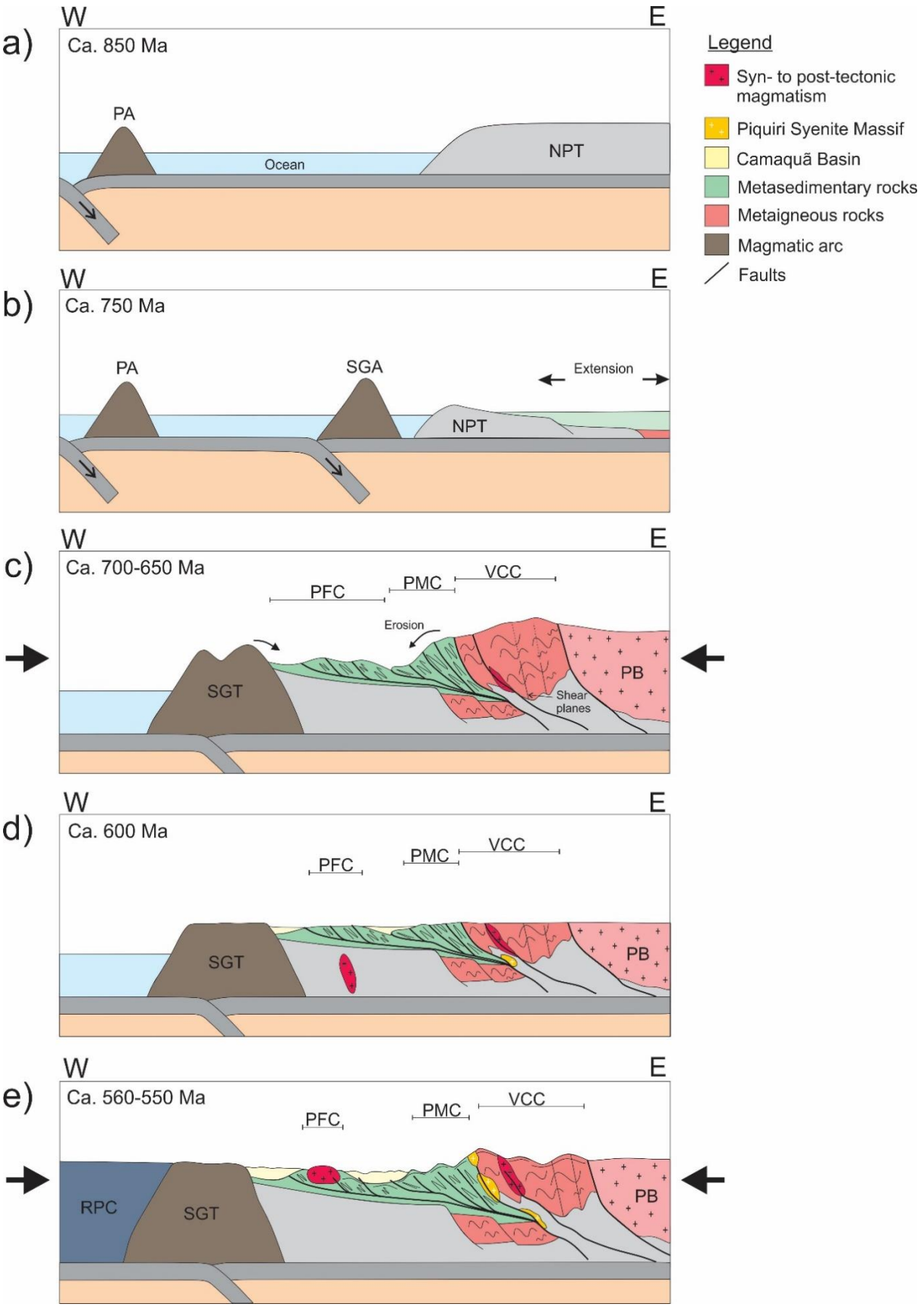

Fig. 4.5 *Proposed model for the Neoproterozoic tectonic evolution of the Dom Feliciano Belt in the state of Rio Grande do Sul. NPT – Nico Pérez Terrane; PA – Passinho Arc; SGA – São Gabriel Arc; PFC – Passo Feio Complex; PMC – Porongos Metamorphic Complex; VCC – Várzea do Capivarita Complex; PB – Pelotas Batholith; RPC – Río de la Plata Craton.*

5 Conclusions

A total of six samples have been studied and analyzed in detail, together with observation and measurements from additional samples, with an aim to better understand the metamorphic evolution of the Passo Feio Complex. A focus has been to correlate these to the easterly Porongos Metamorphic Complex. The main conclusions of this study can be summarized as follows:

- Metapelitic samples collected from the southern part of the Passo Feio Complex contain mineral assemblages suggesting a westward decrease in metamorphic grade. The southeastern part has the highest metamorphic grade (middle amphibolite facies) compared to the lower amphibolite facies and greenschist facies conditions towards the southwestern part of the complex.

- P-T phase equilibrium modelling of the samples collected suggests an apparent thermal gradient of between ca. 19-35°C/km during the metamorphic peak (M_1). This is similar to that for the evolution of the Porongos Metamorphic Complex exposed further to the east. Higher apparent thermal gradiens during the beginning of garnet growth suggest a lowering of the regional gradient during crustal thickening.

- Contact metamorphism is evident close to the Caçapava Granite, indicating that a local thermal event (M_2) occurred after peak metamorphic conditions around the time of the intrusion, at ca. 560 Ma.

- The conclusion of this thesis is that estimates of metamorphic conditions for both the Passo Feio Complex and the Porongos Metamorphic Complex are similar, suggesting that the protolith rocks from both complexes could have originally represented the same rift basin. This rift basin was inverted during the formation of the Dom Feliciano Belt in the state of Rio Grande do Sul in the time interval between ca. 650 and 560 Ma

Work cited

Babinski, M., Chemale Jr, F., Hartmann, L. A., Van Schmus, W. R., & Carlos da Silva, L. (1996). Juvenile accretion at 750–700 Ma in southern Brazil. *Geology*, *24*(5), 439-442.

Basei, M. A. S., Frimmel, H. E., Neto, M. D. C. C., de Araujo, C. E. G., de Castro, N. A., & Passarelli, C. R. (2018). The Tectonic history of the Southern Adamastor ocean based on a correlation of the Kaoko and Dom Feliciano Belts. In Geology of Southwest Gondwana (pp. 63-85). Springer, Cham.

Basei, M. A. S., Frimmel, H. E., Nutman, A. P., & Preciozzi, F. (2008). West Gondwana amalgamation based on detrital zircon ages from Neoproterozoic Ribeira and Dom Feliciano belts of South America and comparison with coeval sequences from SW Africa. Geological Society, London, Special Publications, 294(1), 239-256.

Basei, M. A. S., Neto, M. C., Castro, N. A., Nutman, A. P., Wemmer, K., Yamamoto, M. T., Hueck, M., Osako, L., Siga, O., & Passarelli, C. R. (2011). Tectonic evolution of the Brusque Group, Dom Feliciano belt, Santa Catarina, Southern Brazil. *Journal of South American Earth Sciences*, *32*(4), 324-350.

Basei, M., Siga, O., Masquelin, H., Harara, O., Reis, N., & Preciozzi, F. (2000). The Dom Feliciano belt (Brazil-Uruguay) and its fore land (Rio de la Plata Craton): framework, tectonic evolution and correlations with similar terranes of southwestern Africa.

Battisti, M. A., de Fátima Bitencourt, M., De Toni, G. B., Nardi, L. V. S., & Konopásek, J. (2018). Metavolcanic rocks and orthogneisses from Porongos and Várzea do Capivarita complexes: A case for identification of tectonic interleaving at different crustal levels from structural and geochemical data in southernmost Brazil. *Journal of South American Earth Sciences*, *88*, 253-274.

Bitencourt M.F. (1983). *Geologia, Petrologia e Estrutura dos Metamorfitos da Região de Caçapava do Sul, RS.* MS Dissertation, Universidade Federal do Rio Grande do Sul, Porto Alegre, 161 p.

Bucher, K., & Grapes, R. (2011). *Petrogenesis of metamorphic rocks*. Springer Science & Business Media.

Chemale Jr, F., Hartmann, L. A., & Silva, L. D. (1995). Stratigraphy and tectonism of the Brasiliano Cycle in southern Brazil. *Communications of the Geological Survey of Namibia*, *10*, 151-166.

Connolly, J. A. (2005). Computation of phase equilibria by linear programming: a tool for geodynamic modeling and its application to subduction zone decarbonation. *Earth and Planetary Science Letters*, *236*(1-2), 524-541.

De Toni et al., (in prep.). Correlation of structural and metamorphic evolution in the central Dom Feliciano Belt, southernmost Brazil.

Hartmann, L. A., Leite, J. A. D., Da Silva, L. C., Remus, M. V. D., McNaughton, N. J., Groves, D. I., ... & Vasconcellos, M. A. Z. (2000). Advances in SHRIMP geochronology and their impact on understanding the tectonic and metallogenic evolution of southern Brazil. *Australian Journal of Earth Sciences*, *47*(5), 829-844.

Höfig, D. F., Marques, J. C., Basei, M. A. S., Giusti, R. O., Kohlrausch, C., & Frantz, J. C. (2018). Detrital zircon geochronology (U-Pb LA-ICP-MS) of syn-orogenic basins in SW Gondwana: New insights into the Cryogenian-Ediacaran of Porongos Complex, Dom Feliciano Belt, southern Brazil. *Precambrian Research*, *306*, 189-208.

Hueck, M., Oyhantçabal, P., Philipp, R. P., Basei, M. A. S., & Siegesmund, S. (2018). The Dom Feliciano Belt in Southern Brazil and Uruguay. In *Geology of Southwest Gondwana* (pp. 267-302). Springer, Cham.

Konopásek, J., Janoušek, V., Oyhantçabal, P., Sláma, J., & Ulrich, S. (2018). Did the circum-Rodinia subduction trigger the Neoproterozoic rifting along the Congo–Kalahari Craton margin? *International Journal of Earth Sciences*, *107*(5), 1859-1894.

Lopes, C. G., Pimentel, M. M., Philipp, R. P., Gruber, L., Armstrong, R., & Junges, S. (2015). Provenance of the Passo Feio Complex, Dom Feliciano Belt: implications for the age of supracrustal rocks of the São Gabriel Arc, southern Brazil. *Journal of South American Earth Sciences*, *58*, 9-17.

Martil, M. M. D., de Fátima Bitencourt, M., Nardi, L. V. S., Koester, E., & Pimentel, M. M. (2017). Pre-collisional, Tonian (ca. 790 Ma) continental arc magmatism in southern Mantiqueira Province, Brazil: geochemical and isotopic constraints from the Várzea do Capivarita Complex. *Lithos*, *274*, 39-52.

de Oliveira, C. H. E., Junior, F. C., Jelinek, A. R., Bicca, M. M., & Philipp, R. P. (2014). U–Pb and Lu–Hf isotopes applied to the evolution of the late to post-orogenic transtensional basins of the dom feliciano belt, Brazil. *Precambrian Research*, *246*, 240-255.

Percival, J.J. (in prep.).

Pertille, J., Hartmann, L. A., Santos, J. O. S., McNaughton, N. J., & Armstrong, R. (2017). Reconstructing the Cryogenian–Ediacaran evolution of the Porongos fold and thrust belt, Southern Brasiliano Orogen, based on Zircon U–Pb–Hf–O isotopes. *International Geology Review*, *59*(12), 1532-1560.

Philipp R.P., Pimentel M.M., Basei M.A.S. (2018) The Tectonic Evolution of the São Gabriel Terrane, Dom Feliciano Belt, Southern Brazil: The Closure of the Charrua Ocean. In: Siegesmund S., Basei M., Oyhantçabal P., Oriolo S. (eds) Geology of Southwest Gondwana. Regional Geology Reviews. Springer, Cham.

Philipp, R. P., Pimentel, M. M., & Chemale Jr, F. (2016). Tectonic evolution of the Dom Feliciano Belt in southern Brazil: Geological relationships and U-Pb geochronology. *Brazilian Journal of Geology*, *46*, 83-104.

Porada, H. (1989). Pan-African rifting and orogenesis in southern to equatorial Africa and eastern Brazil. Precambrian Research, 44(2), 103-136.

Rapalini A.E. (2018) The Assembly of Western Gondwana: Reconstruction Based on Paleomagnetic Data. In: Siegesmund S., Basei M., Oyhantçabal P., Oriolo S. (eds) Geology of Southwest Gondwana. Regional Geology Reviews. Springer, Cham.

Remus, M. V. D., Hartmann, L. A., McNaughton, N. J., Groves, D. I., & Fletcher, I. R. (2000). The link between hydrothermal epigenetic copper mineralization and the Caçapava Granite of the Brasiliano Cycle in southern Brazil. *Journal of South American Earth Sciences*, *13*(3), 191-216.

Saalmann, K., Gerdes, A., Lahaye, Y., Hartmann, L. A., Remus, M. V. D., & Läufer, A. (2011). Multiple accretion at the eastern margin of the Rio de la Plata craton: the prolonged Brasiliano orogeny in southernmost Brazil. *International Journal of Earth Sciences*, *100*(2-3), 355-378.

Saalmann, K., Remus, M. V. D., & Hartmann, L. A. (2006). Structural evolution and tectonic setting of the Porongos belt, southern Brazil. *Geological Magazine*, *143*(1), 59-88.

Silva, V. B. D. (2018). Geoquímica e ambiente geotectônico dos metabasitos da região de Caçapava do Sul, RS.

Vidal, O., Parra, T., & Trotet, F. (2001). A thermodynamic model for Fe-Mg aluminous chlorite using data from phase equilibrium experiments and natural pelitic assemblages in the 100 to 600 C, 1 to 25 kb range. *American Journal of Science*, *301*(6), 557-592.

Appendix A

Sample BD03

Mineral	**Garnet**											
Point	1/1.	2/1.	3/1.	5/1.	13/1.	14/1.	23/1.	24/1.	25/1.	26/1.	27/1.	28/1.
Position	Core	Core	Rim	Rim	Core	Rim	Rim			Core	Core	Core
Wt. %												
SiO_2	36,62	36,57	37,40	36,54	36,75	37,20	36,84	36,73	36,60	36,70	36,93	36,66
TiO_2	0,04	0,07	0,06	0,08	0,05	0,06	0,03	0,09	0,08	0,02	0,06	0,07
Cr_2O_3	0,02	0,01	0,03	0,06	0,00	0,00	0,01	0,04	0,00	0,00	0,05	0,02
Al_2O_3	20,76	20,90	20,95	21,02	20,68	21,16	20,84	21,15	20,83	20,78	21,01	20,85
FeO	29,01	29,28	33,02	32,56	28,97	31,69	33,56	30,89	29,86	29,38	28,72	29,44
MnO	8,78	8,91	3,93	4,88	8,45	5,41	3,41	6,31	7,69	8,64	8,70	8,17
MgO	1,92	1,84	2,64	2,44	1,78	2,32	2,72	2,12	2,02	1,84	1,85	1,89
CaO	2,66	2,83	2,68	2,65	2,98	2,69	2,20	3,00	2,75	2,94	2,82	2,93
Na_2O	0,05	0,01	0,03	0,02	0,00	0,00	0,00	0,04	0,03	0,01	0,05	0,02
K_2O	0,00	0,00	0,00	0,01	0,00	0,00	0,00	0,00	0,00	0,00	0,00	0,00
ZnO	0,00	0,00	0,00	0,00	0,00	0,00	0,00	0,00	0,00	0,00	0,00	0,00
Total	99,87	100,41	100,75	100,25	99,65	100,53	99,60	100,37	99,86	100,30	100,20	100,04
12 O												
Si	2,97	2,95	2,99	2,94	2,99	2,99	2,98	2,96	2,97	2,97	2,98	2,97
Ti	0,00	0,00	0,00	0,00	0,00	0,00	0,00	0,01	0,00	0,00	0,00	0,00
Cr	0,00	0,00	0,00	0,00	0,00	0,00	0,00	0,00	0,00	0,00	0,00	0,00
Al	1,98	1,99	1,98	2,00	1,98	2,00	1,99	2,01	1,99	1,98	2,00	1,99
Fe^{3+}	0,08	0,10	0,03	0,11	0,04	0,01	0,04	0,07	0,07	0,09	0,03	0,07
Fe^{2+}	1,89	1,88	2,17	2,09	1,93	2,11	2,23	2,01	1,95	1,90	1,91	1,92
Mn	0,60	0,61	0,27	0,33	0,58	0,37	0,23	0,43	0,53	0,59	0,60	0,56
Mg	0,23	0,22	0,32	0,29	0,22	0,28	0,33	0,25	0,24	0,22	0,22	0,23
Ca	0,23	0,24	0,23	0,23	0,26	0,23	0,19	0,26	0,24	0,25	0,24	0,25
Na	0,01	0,00	0,00	0,00	0,00	0,00	0,00	0,01	0,01	0,00	0,01	0,00
K	0,00	0,00	0,00	0,00	0,00	0,00	0,00	0,00	0,00	0,00	0,00	0,00
Zn	0,00	0,00	0,00	0,00	0,00	0,00	0,00	0,00	0,00	0,00	0,00	0,00
Total	8,00	8,00	8,00	8,00	8,00	8,00	8,00	8,00	8,00	8,00	8,00	8,00
X_{Mg}	0,11	0,11	0,13	0,12	0,10	0,12	0,13	0,11	0,11	0,10	0,10	0,11
X_{Grs}	0,07	0,08	0,08	0,07	0,08	0,08	0,06	0,08	0,08	0,08	0,08	0,08
X_{Sps}	0,19	0,19	0,09	0,10	0,19	0,12	0,08	0,14	0,17	0,19	0,19	0,18

Sample BD03

Mineral	Staurolite							Biotite					
Point	8/1.	11/1.	19/1.	22/1.	33/1.	34/1.	38/1.	7/1.	17/1.	18/1.	30/1.	37/1.	40/1.
Position								Matrix	Matrix	Matrix	Matrix	Matrix	Matrix
Wt. %													
SiO_2	27,14	27,31	27,57	27,65	27,12	27,16	27,39	35,28	35,75	35,60	35,63	35,13	34,90
TiO_2	0,83	0,56	0,63	0,67	0,82	0,81	0,52	1,41	0,75	1,19	1,63	1,47	1,37
Cr_2O_3	0,08	0,03	0,10	0,06	0,11	0,08	0,12	0,13	0,00	0,09	0,04	0,07	0,09
Al_2O_3	53,21	54,09	53,59	53,66	53,14	53,12	54,38	18,58	19,20	19,91	19,34	20,08	19,73
FeO	13,42	12,55	13,28	13,37	13,66	13,74	12,87	19,61	18,23	18,03	17,42	19,22	18,54
MnO	0,18	0,24	0,20	0,19	0,26	0,18	0,26	0,11	0,09	0,10	0,09	0,13	0,09
MgO	1,39	1,36	1,87	1,73	1,67	1,72	1,61	9,75	10,39	10,01	10,20	8,62	9,99
CaO	0,00	0,00	0,00	0,04	0,00	0,00	0,00	0,00	0,00	0,00	0,00	0,00	0,00
Na_2O	0,01	0,01	0,02	0,03	0,03	0,00	0,01	0,08	0,06	0,16	0,20	0,11	0,07
K_2O	0,02	0,01	0,00	0,00	0,00	0,00	0,00	9,42	9,48	9,06	9,29	9,37	9,19
ZnO	0,16	0,19	0,14	0,15	0,17	0,19	0,17	0,00	0,00	0,00	0,00	0,00	0,00
Total	96,43	96,34	97,39	97,55	97,00	97,02	97,33	94,38	93,94	94,12	93,84	94,20	93,97
24 O								*11 O*					
Si	3,91	3,92	3,92	3,93	3,88	3,89	3,89	2,78	2,81	2,79	2,80	2,78	2,75
Ti	0,09	0,06	0,07	0,07	0,09	0,09	0,06	0,08	0,04	0,07	0,10	0,09	0,08
Cr	0,01	0,00	0,01	0,01	0,01	0,01	0,01	0,01	0,00	0,01	0,00	0,00	0,01
Al	9,03	9,16	8,98	8,99	8,97	8,96	9,11	1,73	1,78	1,84	1,79	1,87	1,83
Fe^{3+}	0,00	0,00	0,00	0,00	0,00	0,00	0,00	0,00	0,00	0,00	0,00	0,00	0,00
Fe^{2+}	1,62	1,51	1,58	1,59	1,64	1,64	1,53	1,29	1,20	1,18	1,15	1,27	1,22
Mn	0,02	0,03	0,02	0,02	0,03	0,02	0,03	0,01	0,01	0,01	0,01	0,01	0,01
Mg	0,30	0,29	0,40	0,37	0,36	0,37	0,34	1,14	1,22	1,17	1,20	1,02	1,17
Ca	0,00	0,00	0,00	0,01	0,00	0,00	0,00	0,00	0,00	0,00	0,00	0,00	0,00
Na	0,00	0,00	0,00	0,01	0,01	0,00	0,00	0,01	0,01	0,02	0,03	0,02	0,01
K	0,00	0,00	0,00	0,00	0,00	0,00	0,00	0,95	0,95	0,91	0,93	0,95	0,92
Zn	0,02	0,02	0,01	0,02	0,02	0,02	0,02	0,00	0,00	0,00	0,00	0,00	0,00
Total	15,00	15,00	15,00	15,00	15,00	15,00	15,00	8,00	8,00	8,00	8,00	8,00	8,00
X_{Mg}	0,16	0,16	0,20	0,19	0,18	0,18	0,18	0,47	0,50	0,50	0,51	0,44	0,49

Sample BD03

Mineral	Muscovite					Plagioclase				
Point	6/1.	15/1.	21/1.	32/1.	41/1.	12/1.	16/1.	20/1.	29/1.	39/1.
Position	Matrix	Matrix	Matrix	Matrix	Matrix	Matrix	Matrix	In St	Matrix	Matrix
Wt. %										
SiO_2	45,59	45,40	45,81	45,75	45,71	59,53	60,42	60,30	59,57	59,95
TiO_2	0,39	0,31	0,43	0,45	0,40	0,00	0,00	0,00	0,00	0,03
Cr_2O_3	0,03	0,10	0,17	0,18	0,15	0,00	0,03	0,00	0,00	0,00
Al_2O_3	37,33	36,91	36,96	37,13	36,63	24,95	24,63	24,88	24,98	24,63
FeO	0,81	0,80	0,75	0,73	0,74	0,12	0,03	0,25	0,08	0,08
MnO	0,03	0,01	0,00	0,04	0,00	0,01	0,00	0,00	0,01	0,00
MgO	0,53	0,49	0,58	0,56	0,52	0,00	0,00	0,00	0,00	0,00
CaO	0,00	0,00	0,00	0,01	0,00	7,01	7,06	6,75	6,86	6,95
Na_2O	1,29	1,19	1,16	1,23	1,24	7,76	8,18	8,11	7,85	7,95
K_2O	9,19	9,48	9,39	9,41	9,46	0,08	0,10	0,09	0,10	0,10
ZnO	0,00	0,00	0,00	0,00	0,00	0,00	0,00	0,00	0,00	0,00
Total	95,18	94,68	95,25	95,48	94,84	99,47	100,46	100,37	99,45	99,68
11 O						*8 O*				
Si	3,02	3,03	3,04	3,03	3,04	2,66	2,67	2,67	2,66	2,68
Ti	0,02	0,02	0,02	0,02	0,02	0,00	0,00	0,00	0,00	0,00
Cr	0,00	0,01	0,01	0,01	0,01	0,00	0,00	0,00	0,00	0,00
Al	2,92	2,90	2,89	2,89	2,87	1,32	1,28	1,30	1,32	1,30
Fe^{3+}	0,00	0,00	0,00	0,00	0,00	0,00	0,00	0,01	0,00	0,00
Fe^{2+}	0,04	0,04	0,04	0,04	0,04	0,00	0,00	0,00	0,00	0,00
Mn	0,00	0,00	0,00	0,00	0,00	0,00	0,00	0,00	0,00	0,00
Mg	0,05	0,05	0,06	0,06	0,05	0,00	0,00	0,00	0,00	0,00
Ca	0,00	0,00	0,00	0,00	0,00	0,34	0,33	0,32	0,33	0,33
Na	0,17	0,15	0,15	0,16	0,16	0,67	0,70	0,70	0,68	0,69
K	0,78	0,81	0,79	0,79	0,80	0,00	0,01	0,01	0,01	0,01
Zn	0,00	0,00	0,00	0,00	0,00	0,00	0,00	0,00	0,00	0,00
Total	7,00	7,00	7,00	7,00	7,00	5,00	5,00	5,00	5,00	5,00
X_{Mg}	0,54	0,52	0,58	0,58	0,55					
X_{An}						0,33	0,32	0,31	0,32	0,32

Sample BD03

Mineral	Chlorite			Ilmenite		
Point	31/1.	36/1.	42/1.	4/1.	10/1.	35/1.
Position	Matrix	Matrix	Matrix	In Grt	In St	In St
Wt. %						
SiO_2	24,74	24,16	24,78	0,03	0,00	0,24
TiO_2	0,13	0,08	0,10	52,57	52,85	53,13
Cr_2O_3	0,03	0,03	0,04	0,02	0,03	0,01
Al_2O_3	23,29	23,30	22,56	0,04	0,03	0,21
FeO	23,48	24,70	23,73	44,70	45,55	44,49
MnO	0,17	0,16	0,12	0,97	0,85	1,52
MgO	15,02	14,36	15,23	0,53	0,30	0,18
CaO	0,02	0,06	0,02	0,07	0,00	0,05
Na_2O	0,00	0,00	0,00	0,01	0,01	0,00
K_2O	0,03	0,03	0,06	0,00	0,00	0,05
ZnO	0,00	0,00	0,00	0,00	0,00	0,00
Total	86,92	86,88	86,65	98,94	99,61	99,88
14 O				*3 O*		
Si	2,62	2,57	2,63	0,00	0,00	0,01
Ti	0,01	0,01	0,01	1,00	1,01	1,01
Cr	0,00	0,00	0,00	0,00	0,00	0,00
Al	2,90	2,92	2,82	0,00	0,00	0,01
Fe^{3+}	0,00	0,00	0,00	0,00	0,00	0,00
Fe^{2+}	2,08	2,20	2,11	0,95	0,96	0,94
Mn	0,02	0,01	0,01	0,02	0,02	0,03
Mg	2,37	2,28	2,41	0,02	0,01	0,01
Ca	0,00	0,01	0,00	0,00	0,00	0,00
Na	0,00	0,00	0,00	0,00	0,00	0,00
K	0,00	0,00	0,01	0,00	0,00	0,00
ZnO	0,00	0,00	0,00	0,00	0,00	0,00
Total	10,00	10,00	10,00	2,00	2,00	2,00
X_{Mg}	0,53	0,51	0,53	0,02	0,01	0,01

Sample BD09b

Mineral	Garnet													
Point	43/1.	44/1.	45/1.	46/1.	47/1.	55/1.	56/1.	57/1.	58/1.	59/1.	63/1.	64/1.	65/1.	67/1.
Position	Core	Core	Rim		Rim	Rim			Core	Core	Core		Rim	Rim
Wt. %														
SiO_2	36,61	36,32	36,30	36,47	36,65	36,77	36,28	36,44	36,10	36,10	36,34	36,70	36,40	36,54
TiO_2	0,05	0,03	0,02	0,05	0,00	0,05	0,06	0,07	0,07	0,08	0,07	0,04	0,05	0,04
Cr_2O_3	0,00	0,00	0,00	0,02	0,00	0,01	0,01	0,08	0,03	0,04	0,00	0,00	0,02	0,00
Al_2O_3	20,78	20,73	20,56	20,58	20,62	20,83	20,55	20,75	20,83	20,35	20,83	20,97	20,96	20,98
FeO	37,16	37,85	38,03	37,92	38,91	38,90	39,00	37,70	35,86	35,75	36,10	37,58	38,25	38,82
MnO	1,56	1,27	1,07	1,52	0,76	0,74	1,14	1,88	4,52	4,94	3,59	1,75	0,51	0,95
MgO	1,82	1,87	1,83	1,85	1,93	1,91	1,76	1,51	1,24	1,13	1,27	1,48	1,79	1,78
CaO	1,51	1,25	1,39	1,70	1,33	1,19	1,25	1,71	1,42	1,46	1,74	1,73	1,35	1,23
Na_2O	0,05	0,03	0,05	0,02	0,03	0,00	0,00	0,01	0,00	0,02	0,03	0,00	0,02	0,03
K_2O	0,01	0,00	0,01	0,01	0,00	0,00	0,01	0,01	0,00	0,01	0,00	0,01	0,01	0,01
ZnO	0,00	0,00	0,00	0,00	0,00	0,00	0,00	0,00	0,00	0,00	0,00	0,00	0,00	0,00
Total	99,55	99,36	99,26	100,13	100,23	100,41	100,05	100,16	100,05	99,88	99,97	100,26	99,35	100,37
12 O														
Si	2,99	2,97	2,98	2,97	2,98	2,98	2,96	2,97	2,95	2,96	2,97	2,98	2,98	2,96
Ti	0,00	0,00	0,00	0,00	0,00	0,00	0,00	0,00	0,00	0,00	0,00	0,00	0,00	0,00
Cr	0,00	0,00	0,00	0,00	0,00	0,00	0,00	0,01	0,00	0,00	0,00	0,00	0,00	0,00
Al	2,00	2,00	1,99	1,97	1,97	1,99	1,98	1,99	2,01	1,97	2,01	2,01	2,02	2,01
Fe^{3+}	0,03	0,05	0,07	0,09	0,08	0,04	0,10	0,06	0,08	0,10	0,06	0,02	0,01	0,06
Fe^{2+}	2,51	2,54	2,54	2,49	2,57	2,60	2,56	2,51	2,37	2,35	2,41	2,53	2,60	2,57
Mn	0,11	0,09	0,07	0,10	0,05	0,05	0,08	0,13	0,31	0,34	0,25	0,12	0,04	0,07
Mg	0,22	0,23	0,22	0,22	0,23	0,23	0,21	0,18	0,15	0,14	0,15	0,18	0,22	0,22
Ca	0,13	0,11	0,12	0,15	0,12	0,10	0,11	0,15	0,12	0,13	0,15	0,15	0,12	0,11
Na	0,01	0,01	0,01	0,00	0,00	0,00	0,00	0,00	0,00	0,00	0,00	0,00	0,00	0,00
K	0,00	0,00	0,00	0,00	0,00	0,00	0,00	0,00	0,00	0,00	0,00	0,00	0,00	0,00
Zn	0,00	0,00	0,00	0,00	0,00	0,00	0,00	0,00	0,00	0,00	0,00	0,00	0,00	0,00
Total	8,00	8,00	8,00	8,00	8,00	8,00	8,00	8,00	8,00	8,00	8,00	8,00	8,00	8,00
X_{Mg}	0,08	0,08	0,08	0,08	0,08	0,08	0,08	0,07	0,06	0,06	0,06	0,07	0,08	0,08
X_{Grs}	0,04	0,04	0,04	0,05	0,04	0,03	0,03	0,05	0,04	0,04	0,05	0,05	0,04	0,03
X_{Sps}	0,04	0,03	0,02	0,03	0,02	0,02	0,02	0,04	0,10	0,11	0,08	0,04	0,01	0,02

Sample BD09b

Mineral	Staurolite				Biotite		Plagioclase		Ilmenite
Point	49/1.	50/1.	68/1.	70/1.	66/1.	69/1.	53/1.	60/1.	51/1.
Position					Matrix	Matrix	Matrix	Matrix	In St
Wt. %									
SiO_2	27,25	27,36	27,66	27,52	34,01	33,64	65,35	65,27	0,07
TiO_2	0,46	0,47	0,46	0,66	2,98	2,10	0,00	0,01	52,17
Cr_2O_3	0,00	0,02	0,08	0,15	0,11	0,10	0,04	0,02	0,05
Al_2O_3	53,68	53,96	53,63	54,21	19,18	21,24	21,93	21,82	0,05
FeO	13,96	14,63	14,66	13,80	22,94	21,21	0,12	0,07	45,57
MnO	0,08	0,09	0,04	0,05	0,06	0,04	0,01	0,02	0,35
MgO	1,02	0,99	1,19	1,03	6,24	6,26	0,00	0,00	0,07
CaO	0,02	0,02	0,00	0,00	0,00	0,00	2,87	2,76	0,02
Na_2O	0,00	0,03	0,03	0,03	0,10	0,14	10,14	10,18	0,00
K_2O	0,01	0,01	0,00	0,01	9,26	9,37	0,18	0,16	0,00
ZnO	0,27	0,20	0,34	0,38	0,00	0,00	0,00	0,00	0,00
Total	96,76	97,77	98,09	97,84	94,87	94,09	100,65	100,32	98,34
24 O					*11 O*		*8 O*		*3 O*
Si	3,92	3,90	3,93	3,91	2,73	2,70	2,86	2,86	0,00
Ti	0,05	0,05	0,05	0,07	0,18	0,13	0,00	0,00	1,01
Cr	0,00	0,00	0,01	0,02	0,01	0,01	0,00	0,00	0,00
Al	9,09	9,06	8,97	9,09	1,82	2,01	1,13	1,13	0,00
Fe^{3+}	0,00	0,00	0,00	0,00	0,00	0,00	0,00	0,00	0,00
Fe^{2+}	1,68	1,74	1,74	1,64	1,54	1,42	0,00	0,00	0,98
Mn	0,01	0,01	0,00	0,01	0,00	0,00	0,00	0,00	0,01
Mg	0,22	0,21	0,25	0,22	0,75	0,75	0,00	0,00	0,00
Ca	0,00	0,00	0,00	0,00	0,00	0,00	0,13	0,13	0,00
Na	0,00	0,01	0,01	0,01	0,02	0,02	0,86	0,87	0,00
K	0,00	0,00	0,00	0,00	0,95	0,96	0,01	0,01	0,00
Zn	0,03	0,02	0,04	0,04	0,00	0,00	0,00	0,00	0,00
Total	15,00	15,00	15,00	15,00	8,00	8,00	5,00	5,00	2,00
X_{Mg}	0,12	0,11	0,13	0,12	0,33	0,34			
X_{An}							0,13	0,13	

Sample BD14

Mineral	Garnet														
Point	1/1.	2/1.	8/1.	9/1.	10/1.	12/1.	13/1.	17/1.	19/1.	20/1.	25/1.	26/1.	27/1.	32/1.	33/1.
Position	Core	Rim	Rim	Core	Core	Rim	Rim	Rim	Core	Rim	Rim	Core	Rim	Core	Rim
Wt. %															
SiO_2	36,26	36,85	37,10	36,50	35,52	36,38	36,55	36,31	36,24	36,26	36,14	35,76	36,07	36,53	36,26
TiO_2	0,10	0,02	0,10	0,02	0,07	0,07	0,02	0,00	0,08	0,07	0,03	0,03	0,07	0,06	0,06
Cr_2O_3	0,00	0,04	0,00	0,00	0,05	0,02	0,02	0,01	0,02	0,02	0,04	0,03	0,03	0,00	0,00
Al_2O_3	20,82	20,91	20,90	20,63	20,28	20,39	20,75	20,87	20,12	20,54	20,73	20,28	20,43	20,85	20,76
FeO	28,21	37,29	36,48	29,67	28,59	31,49	36,46	36,87	28,19	31,59	36,55	35,85	37,37	26,59	34,78
MnO	12,11	1,26	1,50	9,97	10,97	6,79	1,39	1,86	11,09	7,11	2,07	3,31	1,36	12,85	3,67
MgO	0,89	1,86	1,75	1,03	1,01	1,18	1,93	1,80	0,95	1,09	1,66	1,48	1,81	0,88	1,46
CaO	2,49	2,10	2,68	2,46	2,59	2,77	2,31	2,13	2,63	2,97	2,33	2,46	2,26	2,51	2,61
Na_2O	0,00	0,00	0,00	0,00	0,02	0,00	0,00	0,00	0,05	0,00	0,02	0,01	0,00	0,00	0,01
K_2O	0,01	0,01	0,00	0,00	0,00	0,01	0,02	0,00	0,00	0,00	0,00	0,00	0,01	0,00	0,00
ZnO	0,00	0,00	0,00	0,00	0,00	0,00	0,00	0,00	0,00	0,00	0,00	0,00	0,00	0,00	0,00
Total	100,88	100,33	100,51	100,28	99,10	99,10	99,44	99,85	99,35	99,65	99,54	99,20	99,39	100,28	99,62
12 O															
Si	2,94	2,98	3,00	2,97	2,93	2,99	2,98	2,96	2,98	2,97	2,95	2,94	2,95	2,97	2,96
Ti	0,01	0,00	0,01	0,00	0,00	0,00	0,00	0,00	0,00	0,00	0,00	0,00	0,00	0,00	0,00
Cr	0,00	0,00	0,00	0,00	0,00	0,00	0,00	0,00	0,00	0,00	0,00	0,00	0,00	0,00	0,00
Al	1,99	2,00	1,99	1,98	1,97	1,98	1,99	2,00	1,95	1,98	2,00	1,96	1,97	2,00	2,00
Fe^{3+}	0,12	0,03	0,01	0,07	0,16	0,03	0,04	0,09	0,09	0,07	0,10	0,16	0,12	0,04	0,07
Fe^{2+}	1,79	2,49	2,46	1,95	1,81	2,13	2,45	2,42	1,85	2,09	2,40	2,31	2,44	1,77	2,30
Mn	0,83	0,09	0,10	0,69	0,77	0,47	0,10	0,13	0,77	0,49	0,14	0,23	0,09	0,89	0,25
Mg	0,11	0,22	0,21	0,13	0,12	0,14	0,23	0,22	0,12	0,13	0,20	0,18	0,22	0,11	0,18
Ca	0,22	0,18	0,23	0,21	0,23	0,24	0,20	0,19	0,23	0,26	0,20	0,22	0,20	0,22	0,23
Na	0,00	0,00	0,00	0,00	0,00	0,00	0,00	0,00	0,01	0,00	0,00	0,00	0,00	0,00	0,00
K	0,00	0,00	0,00	0,00	0,00	0,00	0,00	0,00	0,00	0,00	0,00	0,00	0,00	0,00	0,00
Zn	0,00	0,00	0,00	0,00	0,00	0,00	0,00	0,00	0,00	0,00	0,00	0,00	0,00	0,00	0,00
Total	8,00	8,00	8,00	8,00	8,00	8,00	8,00	8,00	8,00	8,00	8,00	8,00	8,00	8,00	8,00
X_{Mg}	0,06	0,08	0,08	0,06	0,06	0,06	0,09	0,08	0,06	0,06	0,08	0,07	0,08	0,06	0,07
X_{Grs}	0,07	0,06	0,08	0,07	0,07	0,08	0,07	0,06	0,07	0,08	0,06	0,07	0,06	0,07	0,07
X_{Sps}	0,26	0,03	0,03	0,22	0,23	0,15	0,03	0,04	0,24	0,16	0,05	0,07	0,03	0,29	0,08

Sample BD14

Mineral	Staurolite			Biotite				Muscovite			
Point	5/1.	16/1.	18/1.	6/1.	15/1.	21/1.	23/1.	3/1.	14/1.	22/1.	30/1.
Position				Matrix	Matrix	Matrix	Matrix	Matrix	Matrix	Matrix	Matrix
Wt. %											
SiO_2	27,28	27,67	26,81	34,31	21,37	24,70	34,54	45,92	45,89	45,50	45,43
TiO_2	0,53	0,23	0,36	1,48	0,09	0,10	1,65	0,29	0,21	0,28	0,24
Cr_2O_3	0,01	0,00	0,03	0,03	0,04	0,01	0,00	0,05	0,03	0,07	0,00
Al_2O_3	54,71	53,63	54,35	19,55	20,52	23,54	19,30	36,95	36,63	36,92	37,67
FeO	13,19	12,80	13,39	22,12	34,33	27,63	19,97	1,14	0,89	0,85	1,03
MnO	0,04	0,09	0,07	0,03	0,10	0,07	0,00	0,01	0,00	0,01	0,02
MgO	1,11	0,96	1,22	7,43	9,97	12,08	8,21	0,48	0,44	0,41	0,32
CaO	0,01	0,00	0,01	0,00	0,19	0,01	0,00	0,00	0,00	0,01	0,00
Na_2O	0,03	0,03	0,03	0,38	0,05	0,02	0,35	1,77	1,60	1,75	1,83
K_2O	0,01	0,01	0,00	7,97	0,20	0,06	8,63	8,43	8,83	8,45	8,29
ZnO	1,21	1,00	0,94	0,00	0,00	0,00	0,00	0,00	0,00	0,00	0,00
Total	98,14	96,42	97,23	93,29	86,87	88,22	92,65	95,03	94,51	94,24	94,84
24 O				*11 O*				*11 O*			
Si	3,87	3,99	3,83	2,77	1,90	2,11	2,79	3,04	3,06	3,04	3,01
Ti	0,06	0,03	0,04	0,09	0,01	0,01	0,10	0,01	0,01	0,01	0,01
Cr	0,00	0,00	0,00	0,00	0,00	0,00	0,00	0,00	0,00	0,00	0,00
Al	9,14	9,11	9,15	1,86	2,15	2,37	1,84	2,89	2,88	2,91	2,95
Fe^{3+}	0,00	0,00	0,00	0,00	0,06	0,00	0,00	0,00	0,00	0,00	0,00
Fe^{2+}	1,56	1,54	1,60	1,49	2,50	1,97	1,35	0,06	0,05	0,05	0,06
Mn	0,01	0,01	0,01	0,00	0,01	0,00	0,00	0,00	0,00	0,00	0,00
Mg	0,23	0,21	0,26	0,89	1,32	1,53	0,99	0,05	0,04	0,04	0,03
Ca	0,00	0,00	0,00	0,00	0,02	0,00	0,00	0,00	0,00	0,00	0,00
Na	0,01	0,01	0,01	0,06	0,01	0,00	0,05	0,23	0,21	0,23	0,24
K	0,00	0,00	0,00	0,82	0,02	0,01	0,89	0,71	0,75	0,72	0,70
Zn	0,13	0,11	0,10	0,00	0,00	0,00	0,00	0,00	0,00	0,00	0,00
Total	15,00	15,00	15,00	8,00	8,00	8,00	8,00	7,00	7,00	7,00	7,00
X_{Mg}	0,13	0,12	0,14	0,37	0,35	0,44	0,42	0,43	0,47	0,46	0,36

Sample BD14

Mineral	Chlorite		Plagioclase	Ilmenite			
Point	4/1.	29/1.	28/1.	7/1.	11/1.	24/1.	31/1.
Position	Matrix	Matrix	Matrix	In St	In Grt	Matrix	Matrix
Wt. %							
SiO_2	23,76	24,17	62,62	0,04	0,02	0,13	0,04
TiO_2	0,07	0,31	0,01	52,46	52,71	56,57	54,99
Cr_2O_3	0,00	0,05	0,00	0,00	0,05	0,00	0,00
Al_2O_3	23,26	22,46	23,07	0,05	0,04	0,14	0,06
FeO	28,56	26,46	0,15	44,92	45,95	39,01	42,53
MnO	0,10	0,09	0,01	1,96	1,58	0,47	0,60
MgO	11,80	10,71	0,00	0,22	0,17	0,01	0,04
CaO	0,03	0,02	4,58	0,05	0,06	0,02	0,01
Na_2O	0,00	0,03	9,49	0,00	0,00	0,03	0,00
K_2O	0,02	0,37	0,09	0,01	0,01	0,10	0,08
ZnO	0,00	0,00	0,00	0,00	0,00	0,00	0,00
Total	87,60	84,67	100,03	99,70	100,59	96,47	98,36
14 O			*8 O*	*3 O*			
Si	2,56	2,70	2,76	0,00	0,00	0,00	0,00
Ti	0,01	0,03	0,00	1,00	0,99	1,12	1,06
Cr	0,00	0,00	0,00	0,00	0,00	0,00	0,00
Al	2,95	2,95	1,20	0,00	0,00	0,00	0,00
Fe^{3+}	0,00	0,00	0,01	0,00	0,01	0,00	0,00
Fe^{2+}	2,57	2,47	0,00	0,95	0,95	0,86	0,92
Mn	0,01	0,01	0,00	0,04	0,03	0,01	0,01
Mg	1,89	1,78	0,00	0,01	0,01	0,00	0,00
Ca	0,00	0,00	0,22	0,00	0,00	0,00	0,00
Na	0,00	0,01	0,81	0,00	0,00	0,00	0,00
K	0,00	0,05	0,01	0,00	0,00	0,00	0,00
Zn	0,00	0,00	0,00	0,00	0,00	0,00	0,00
Total	10,00	10,00	5,00	2,00	2,00	2,00	2,00
X_{Mg}	0,42	0,42					
X_{An}			0,21				

Sample BD15

Mineral	Garnet								
Point	35/1.	37/1.	43/1.	44/1.	52/1.	53/1.	54/1.	60/1.	61/1.
Position	Core	Rim	Core	Rim	Core	Rim	Core	Rim	Core
Wt. %									
SiO_2	36,52	36,76	36,39	36,61	36,44	36,45	36,15	36,05	36,36
TiO_2	0,05	0,02	0,04	0,02	0,08	0,04	0,06	0,00	0,11
Cr_2O_3	0,00	0,02	0,05	0,04	0,01	0,00	0,02	0,04	0,16
Al_2O_3	20,65	20,77	20,86	20,61	20,66	20,61	20,48	20,70	20,57
FeO	35,79	37,19	35,93	37,54	33,25	37,37	37,54	38,49	32,18
MnO	3,43	1,35	3,55	1,46	5,97	1,55	1,88	1,42	7,60
MgO	1,55	1,92	1,56	1,87	1,21	1,75	1,72	1,95	1,16
CaO	1,75	1,48	1,61	1,31	2,05	1,52	1,67	1,13	2,16
Na_2O	0,00	0,03	0,02	0,01	0,01	0,01	0,00	0,03	0,03
K_2O	0,00	0,00	0,00	0,01	0,00	0,01	0,00	0,01	0,01
ZnO	0,00	0,00	0,00	0,00	0,00	0,00	0,00	0,00	0,00
Total	99,74	99,54	100,03	99,48	99,68	99,32	99,52	99,81	100,32
12 O									
Si	2,98	3,00	2,96	2,99	2,98	2,99	2,96	2,94	2,96
Ti	0,00	0,00	0,00	0,00	0,01	0,00	0,00	0,00	0,01
Cr	0,00	0,00	0,00	0,00	0,00	0,00	0,00	0,00	0,01
Al	1,99	2,00	2,00	1,99	1,99	1,99	1,98	1,99	1,97
Fe^{3+}	0,04	0,00	0,06	0,02	0,03	0,03	0,09	0,13	0,09
Fe^{2+}	2,41	2,54	2,38	2,55	2,24	2,53	2,48	2,50	2,10
Mn	0,24	0,09	0,24	0,10	0,41	0,11	0,13	0,10	0,52
Mg	0,19	0,23	0,19	0,23	0,15	0,21	0,21	0,24	0,14
Ca	0,15	0,13	0,14	0,12	0,18	0,13	0,15	0,10	0,19
Na	0,00	0,00	0,00	0,00	0,00	0,00	0,00	0,00	0,00
K	0,00	0,00	0,00	0,00	0,00	0,00	0,00	0,00	0,00
Zn	0,00	0,00	0,00	0,00	0,00	0,00	0,00	0,00	0,00
Total	8,00	8,00	8,00	8,00	8,00	8,00	8,00	8,00	8,00
X_{Mg}	0,07	0,08	0,07	0,08	0,06	0,08	0,08	0,09	0,06
X_{Grs}	0,05	0,04	0,05	0,04	0,06	0,04	0,05	0,03	0,06
X_{Sps}	0,08	0,03	0,08	0,03	0,14	0,04	0,04	0,03	0,17

Sample BD15

Mineral	Staurolite							Muscovite		
Point	39/1.	45/1.	49/1.	51/1.	57/1.	58/1.	62/1.	42/1.	50/1.	56/1.
Position								Matrix	Matrix	Matrix
Wt. %										
SiO_2	26,96	27,48	27,64	27,56	27,16	26,90	27,23	45,01	44,78	45,95
TiO_2	0,36	0,37	0,38	0,43	0,43	0,49	0,38	0,27	0,19	0,26
Cr_2O_3	0,02	0,03	0,01	0,11	0,03	0,07	0,09	0,03	0,06	0,02
Al_2O_3	55,14	54,03	53,86	54,10	54,42	55,40	54,80	36,84	36,30	37,26
FeO	13,13	12,81	12,73	13,47	13,55	13,63	13,04	0,79	0,77	0,89
MnO	0,14	0,10	0,10	0,11	0,14	0,12	0,16	0,01	0,04	0,00
MgO	1,12	1,01	1,19	1,30	1,20	1,06	0,88	0,26	0,32	0,42
CaO	0,00	0,00	0,00	0,01	0,01	0,00	0,01	0,02	0,00	0,00
Na_2O	0,02	0,04	0,03	0,02	0,01	0,03	0,02	1,41	1,43	1,75
K_2O	0,01	0,02	0,02	0,00	0,00	0,01	0,00	8,96	8,58	8,38
ZnO	0,37	0,32	0,25	0,35	0,27	0,42	0,39	0,00	0,00	0,00
Total	97,28	96,21	96,21	97,46	97,23	98,12	97,01	93,61	92,48	94,93
24 O								*11 O*		
Si	3,84	3,96	3,98	3,93	3,87	3,80	3,89	3,03	3,05	3,05
Ti	0,04	0,04	0,04	0,05	0,05	0,05	0,04	0,01	0,01	0,01
Cr	0,00	0,00	0,00	0,01	0,00	0,01	0,01	0,00	0,00	0,00
Al	9,26	9,18	9,14	9,08	9,15	9,23	9,24	2,93	2,92	2,91
Fe^{3+}	0,00	0,00	0,00	0,00	0,00	0,00	0,00	0,00	0,00	0,00
Fe^{2+}	1,56	1,54	1,53	1,60	1,62	1,61	1,56	0,04	0,04	0,05
Mn	0,02	0,01	0,01	0,01	0,02	0,01	0,02	0,00	0,00	0,00
Mg	0,24	0,22	0,25	0,28	0,26	0,22	0,19	0,03	0,03	0,04
Ca	0,00	0,00	0,00	0,00	0,00	0,00	0,00	0,00	0,00	0,00
Na	0,01	0,01	0,01	0,00	0,00	0,01	0,01	0,18	0,19	0,23
K	0,00	0,00	0,00	0,00	0,00	0,00	0,00	0,77	0,75	0,71
Zn	0,04	0,03	0,03	0,04	0,03	0,04	0,04	0,00	0,00	0,00
Total	15,00	15,00	15,00	15,00	15,00	15,00	15,00	7,00	7,00	7,00
X_{Mg}	0,13	0,12	0,14	0,15	0,14	0,12	0,11	0,37	0,43	0,46

Sample BD15

Mineral	Plagioclase		Biotite			Chlorite	Ilmenite	
Point	48/1.	59/1.	38/1.	46/1.	55/1.	41/1.	36/1.	63/1.
Position	Matrix	Matrix	Matrix	Matrix	Matrix	Matrix	In Grt	In Grt
Wt. %								
SiO_2	63,63	64,07	34,69	34,06	34,21	23,61	0,02	-0,01
TiO_2	0,01	0,01	1,57	1,60	1,66	0,07	53,36	53,74
Cr_2O_3	0,01	0,00	0,01	0,05	0,04	0,00	0,00	0,05
Al_2O_3	22,28	18,27	20,09	19,41	20,60	22,00	0,00	0,00
FeO	0,11	0,23	21,55	22,74	22,47	28,93	44,93	46,09
MnO	0,03	0,03	0,08	0,05	0,09	0,13	1,39	0,67
MgO	0,01	0,01	7,40	7,22	5,99	11,69	0,08	0,19
CaO	3,80	0,00	0,00	0,00	0,04	0,05	0,00	0,00
Na_2O	9,87	0,19	0,17	0,07	0,09	0,00	0,00	0,02
K_2O	0,07	16,63	8,75	8,92	8,96	0,03	0,00	0,00
ZnO	0,00	0,00	0,00	0,00	0,00	0,00	0,00	0,00
Total	99,82	99,44	94,31	94,13	94,16	86,51	99,78	100,75
8 O			*11 O*			*14 O*	*3 O*	
Si	2,81	2,98	2,77	2,74	2,76	2,58	0,00	0,00
Ti	0,00	0,00	0,09	0,10	0,10	0,01	1,02	1,01
Cr	0,00	0,00	0,00	0,00	0,00	0,00	0,00	0,00
Al	1,16	1,00	1,89	1,84	1,96	2,84	0,00	0,00
Fe^{3+}	0,00	0,01	0,00	0,00	0,00	0,00	0,00	0,00
Fe^{2+}	0,00	0,00	1,44	1,53	1,51	2,65	0,95	0,97
Mn	0,00	0,00	0,01	0,00	0,01	0,01	0,03	0,01
Mg	0,00	0,00	0,88	0,87	0,72	1,91	0,00	0,01
Ca	0,18	0,00	0,00	0,00	0,00	0,01	0,00	0,00
Na	0,84	0,02	0,03	0,01	0,01	0,00	0,00	0,00
K	0,00	0,99	0,89	0,91	0,92	0,00	0,00	0,00
Zn	0,00	0,00	0,00	0,00	0,00	0,00	0,00	0,00
Total	5,00	5,00	8,00	8,00	8,00	10,00	2,00	2,00
X_{Mg}			0,38	0,36	0,32	0,42		
X_{An}	0,17	0,00						

Sample BD16c

Mineral	Garnet										
Point	1/1.	4/1.	7/1.	8/1.	9/1.	14/1.	15/1.	17/1.	19/1.	20/1.	21/1.
Position	Core	Rim	Core	Core	Rim	Core	Rim	Rim	Core	Rim	Rim
Wt. %											
SiO_2	34,62	36,67	36,37	36,51	36,43	36,37	36,28	36,45	36,18	36,46	36,00
TiO_2	0,18	0,11	0,13	0,19	0,13	0,14	0,17	0,11	0,13	0,09	0,14
Cr_2O_3	0,01	0,02	0,01	0,02	0,02	0,04	0,00	0,01	0,02	0,03	0,00
Al_2O_3	20,44	20,72	20,55	20,45	20,49	20,14	20,59	20,49	20,32	20,15	20,67
FeO	23,26	25,45	24,57	23,99	26,05	23,89	26,69	26,32	23,05	27,86	27,82
MnO	17,13	12,86	14,01	14,63	12,00	14,74	13,07	13,47	15,97	10,31	10,63
MgO	0,80	0,90	0,89	0,77	0,86	0,82	0,88	0,89	0,83	1,01	1,05
CaO	3,59	3,43	3,39	3,55	4,05	3,00	2,52	2,59	3,42	3,72	3,76
Na_2O	0,00	0,03	0,01	0,03	0,04	0,08	0,01	0,00	0,02	0,00	0,03
K_2O	0,00	0,00	0,00	0,00	0,00	0,02	0,00	0,01	0,00	0,02	0,00
ZnO	0,00	0,00	0,00	0,00	0,00	0,00	0,00	0,00	0,00	0,00	0,00
Total	100,03	100,20	99,94	100,14	100,07	99,25	100,22	100,33	99,95	99,65	100,10
12 O											
Si	2,83	2,98	2,97	2,97	2,96	2,99	2,96	2,97	2,95	2,98	2,93
Ti	0,01	0,01	0,01	0,01	0,01	0,01	0,01	0,01	0,01	0,01	0,01
Cr	0,00	0,00	0,00	0,00	0,00	0,00	0,00	0,00	0,00	0,00	0,00
Al	1,97	1,98	1,98	1,96	1,96	1,95	1,98	1,97	1,95	1,94	1,98
Fe^{3+}	0,35	0,05	0,08	0,07	0,10	0,06	0,08	0,08	0,12	0,09	0,15
Fe^{2+}	1,24	1,68	1,60	1,56	1,68	1,58	1,74	1,71	1,45	1,82	1,74
Mn	1,19	0,88	0,97	1,01	0,83	1,03	0,90	0,93	1,10	0,71	0,73
Mg	0,10	0,11	0,11	0,09	0,10	0,10	0,11	0,11	0,10	0,12	0,13
Ca	0,31	0,30	0,30	0,31	0,35	0,26	0,22	0,23	0,30	0,33	0,33
Na	0,00	0,01	0,00	0,01	0,01	0,01	0,00	0,00	0,00	0,00	0,00
K	0,00	0,00	0,00	0,00	0,00	0,00	0,00	0,00	0,00	0,00	0,00
Zn	0,00	0,00	0,00	0,00	0,00	0,00	0,00	0,00	0,00	0,00	0,00
Total	8,00	8,00	8,00	8,00	8,00	8,00	8,00	8,00	8,00	8,00	8,00
X_{Mg}	0,07	0,06	0,06	0,06	0,06	0,06	0,06	0,06	0,07	0,06	0,07
X_{Grs}	0,09	0,10	0,09	0,10	0,11	0,08	0,07	0,07	0,09	0,10	0,10
X_{Sps}	0,32	0,29	0,31	0,32	0,26	0,33	0,29	0,30	0,34	0,23	0,22

Sample BD16c

Mineral	Muscovite						Biotite					
Point	3/1.	5/1.	12/1.	13/1.	18/1.	23/1.	2/1.	6/1.	10/1.	11/1.	16/1.	22/1.
Position	Matrix	Matrix	Matrix	Matrix	Matrix	Matrix	Matrix	Matrix	Matrix	Matrix	Matrix	Matrix
Wt. %												
SiO_2	46,03	45,99	45,22	45,00	46,79	45,75	37,60	35,16	35,79	35,33	35,01	35,33
TiO_2	0,25	0,26	0,28	0,27	0,26	0,29	1,02	1,67	1,27	1,55	1,13	1,85
Cr_2O_3	0,02	0,00	0,04	0,00	0,01	0,04	0,01	0,05	0,00	0,02	0,01	0,01
Al_2O_3	36,27	36,04	33,38	34,04	33,44	34,86	20,15	19,70	19,50	20,21	19,93	20,44
FeO	2,11	2,34	3,20	2,60	2,67	2,31	19,14	20,47	22,18	21,12	21,92	20,08
MnO	0,00	0,02	0,01	0,00	0,07	0,03	0,09	0,14	0,19	0,20	0,31	0,15
MgO	0,64	0,60	1,01	0,72	0,95	0,82	7,45	7,39	6,81	6,59	7,04	5,98
CaO	0,00	0,00	0,00	0,00	0,00	0,01	0,19	0,09	0,17	0,22	0,23	0,29
Na_2O	0,88	0,78	0,66	0,72	0,54	0,73	0,11	0,24	0,19	0,24	0,19	0,27
K_2O	9,71	9,87	9,61	9,46	9,79	9,56	6,08	8,44	7,72	8,24	8,17	7,04
ZnO	0,00	0,00	0,00	0,00	0,00	0,00	0,00	0,00	0,00	0,00	0,00	0,00
Total	95,92	95,90	93,42	92,80	94,50	94,40	91,84	93,36	93,81	93,71	93,94	91,45
11 O							*11 O*					
Si	3,05	3,05	3,09	3,09	3,16	3,08	3,09	2,83	2,89	2,85	2,82	2,93
Ti	0,01	0,01	0,01	0,01	0,01	0,01	0,06	0,10	0,08	0,09	0,07	0,12
Cr	0,00	0,00	0,00	0,00	0,00	0,00	0,00	0,00	0,00	0,00	0,00	0,00
Al	2,83	2,81	2,69	2,75	2,66	2,77	1,95	1,87	1,86	1,92	1,89	2,00
Fe^{3+}	0,00	0,00	0,03	0,00	0,00	0,00	0,00	0,00	0,00	0,00	0,00	0,00
Fe^{2+}	0,12	0,13	0,15	0,15	0,15	0,13	1,31	1,38	1,50	1,42	1,47	1,39
Mn	0,00	0,00	0,00	0,00	0,00	0,00	0,01	0,01	0,01	0,01	0,02	0,01
Mg	0,06	0,06	0,10	0,07	0,10	0,08	0,91	0,89	0,82	0,79	0,84	0,74
Ca	0,00	0,00	0,00	0,00	0,00	0,00	0,02	0,01	0,01	0,02	0,02	0,03
Na	0,11	0,10	0,09	0,10	0,07	0,09	0,02	0,04	0,03	0,04	0,03	0,04
K	0,82	0,83	0,84	0,83	0,84	0,82	0,64	0,87	0,80	0,85	0,84	0,74
Zn	0,00	0,00	0,00	0,00	0,00	0,00	0,00	0,00	0,00	0,00	0,00	0,00
Total	7,00	7,00	7,00	7,00	7,00	7,00	8,00	8,00	8,00	8,00	8,00	8,00
X_{Mg}	0,35	0,31	0,41	0,33	0,39	0,39	0,41	0,39	0,35	0,36	0,36	0,35

Sample BD21

Mineral	Muscovite						Hematite
Point	24/1.	25/1.	27/1.	28/1.	29/1.	30/1.	26/1.
Position	Matrix	Matrix	Matrix	Matrix	Matrix	Matrix	Matrix
Wt. %							
SiO_2	45,48	44,96	45,77	46,40	45,78	45,34	0,12
TiO_2	0,18	0,19	0,22	0,27	0,27	0,21	0,04
Cr_2O_3	0,02	0,00	0,01	0,05	0,04	0,02	0,04
Al_2O_3	36,99	35,87	36,98	35,93	35,84	36,78	0,34
FeO	1,85	1,88	1,90	1,97	1,99	1,85	86,91
MnO	0,00	0,00	0,00	0,00	0,02	0,02	0,05
MgO	0,28	0,34	0,26	0,42	0,40	0,27	0,01
CaO	0,41	0,07	0,00	0,03	0,02	0,04	0,02
Na_2O	2,29	1,58	2,05	1,71	1,82	2,26	0,00
K_2O	7,47	7,47	8,44	8,53	8,59	8,13	0,01
ZnO	0,00	0,00	0,00	0,00	0,00	0,00	0,00
Total	94,96	92,35	95,64	95,32	94,76	94,91	87,53
11 O							*3 O*
Si	3,02	3,08	3,01	3,08	3,05	3,00	0,00
Ti	0,01	0,01	0,01	0,01	0,01	0,01	0,00
Cr	0,00	0,00	0,00	0,00	0,00	0,00	0,00
Al	2,89	2,90	2,87	2,81	2,82	2,87	0,01
Fe^{3+}	0,00	0,00	0,05	0,00	0,02	0,07	1,98
Fe^{2+}	0,10	0,11	0,06	0,11	0,09	0,03	0,00
Mn	0,00	0,00	0,00	0,00	0,00	0,00	0,00
Mg	0,03	0,03	0,03	0,04	0,04	0,03	0,00
Ca	0,03	0,00	0,00	0,00	0,00	0,00	0,00
Na	0,29	0,21	0,26	0,22	0,23	0,29	0,00
K	0,63	0,65	0,71	0,72	0,73	0,69	0,00
Zn	0,00	0,00	0,00	0,00	0,00	0,00	0,00
Total	7,00	7,00	7,00	7,00	7,00	7,00	2,00
X_{Mg}	0,21	0,24	0,31	0,28	0,30	0,47	0,12